3-2020

Analysis of Additively Manufactured Rings Under Compression Loading for Use in a Vacuum Lighter Than Air Vehicle Structure

Kevin D. Greenoe

Analysis of Additively Manufactured Rings Under Compression Loading for Use in a Vacuum Lighter Than Air Vehicle Structure

THESIS

Kevin D. Greenoe, 2d Lt, USAF

AFIT-ENY-MS-20-M-264

DEPARTMENT OF THE AIR FORCE
AIR UNIVERSITY

AIR FORCE INSTITUTE OF TECHNOLOGY

Wright-Patterson Air Force Base, Ohio

AFIT-ENY-MS-20-M-264

ANALYSIS OF ADDITIVELY MANUFACTURED RINGS UNDER COMPRESSION LOADING FOR USE IN A VACUUM LIGHTER THAN AIR VEHICLE STRUCTURE

THESIS

Presented to the Faculty

Department of Aeronautics and Astronautics

Graduate School of Engineering and Management

Air Force Institute of Technology

Air University

Air Education and Training Command

in Partial Fulfillment of the Requirements for the

Degree of Master of Science in Aeronautical Engineering

Kevin D. Greenoe, B.S. ME

2d Lt, USAF

26 March 2020

AFIT-ENY-MS-20-M-264

ANALYSIS OF ADDITIVELY MANUFACTURED RINGS UNDER COMPRESSION LOADING FOR USE IN A VACUUM LIGHTER THAN AIR VEHICLE STRUCTURE

THESIS

Kevin D. Greenoe, B.S. ME
2d Lt, USAF

Committee Membership:

A. N. Palazotto, PhD
Chairman

R. A. Kemnitz, Maj, PhD
Member

M. N. Pachter, PhD
Member

Abstract

A Vacuum Lighter Than Air Vehicle (VLTAV) utilizes a lightweight structure paired with an internal vacuum to achieve buoyancy; this allows it to float throughout a given atmosphere. The pressure differential between the internal vacuum and external atmosphere places the vehicle under intense loading. Therefore, the VLTAV must be comprised of a lightweight, durable structure. A specific structure under investigation is the celestial icosahedron, which features nine intersecting rings that have an outer diameter of 0.2032 m and circular cross-sectional thickness of 5.08 mm. The celestial's rings are positioned in three different orientations with respect to the horizontal plane: 0°, 45°, and 90°. Rings for each orientation were additively manufactured (AM), out of ULTEM 9085 resin, using fused deposition modeling (FDM). The rings were placed under compression to investigate their nonlinear behavior and mechanical properties. Ring models with the same geometry were generated and analyzed using finite element analysis (FEA) under similar loading conditions. The experimental and analytical results were used to evaluate the material properties for each build orientation. The results from both methods were used to investigate the nonlinear behavior of the rings.

Acknowledgements

I would like to acknowledge and thank the following:

- Dr. Anthony Palazotto for his guidance, insight, and wisdom
- Travis Shelton for his technical assistance and expertise
- Maj Ryan Kemnitz for his generous advice and guidance
- Dr. Jamie Tiley, and AFOSR, for the resources to make this research possible
- Mike Ranft, Brian Crabtree, Ben Doane, and all other technicians from the AFIT Model Shop and ENY Labs
- Dr. Meir Pachter for his contributions as a committee member

This research would not have been possible without the support and assistance received from all those mentioned.

Kevin D. Greenoe

Table of Contents

Page

List of Figures

Figure Page

List of Tables

List of Abbreviations

Abbreviation		Page
LTAV	Lighter Than Air Vehicle	1
VLTAV	Vacuum Lighter Than Air Vehicle	1
AM	Additive Manufacturing	2
FEA	Finite Element Analysis	2
UAV	Unmanned Aerial Vehicle	2
WWI	World War I	5
AFIT	Air Force Institute of Technology	8
NR	Newton–Raphson	15
FEM	Finite Element Method	15
CAE	Complete Abaqus Environment	17
DOF	Degrees of Freedom	17
PDE	Partial Differential Equation	19
CG	Center of Gravity	25
FBD	Free Body Diagram	28
FDM	Fused Deposition Modeling	39
CAD	Computer-Aided Design	43
STL	Stereolithography	43
FS	Full Scale	59

List of Symbols

ANALYSIS OF ADDITIVELY MANUFACTURED RINGS UNDER COMPRESSION LOADING FOR USE IN A VACUUM LIGHTER THAN AIR VEHICLE STRUCTURE

I. Introduction

1.1 Overview

Throughout the modern world, it is commonplace to see an airplane or helicopter gliding through the sky at any given moment. Airliners, jets, and helicopters have dominated the air since the middle to late 20^{th} century. Modern vehicles are a testament to the exponential progression of aviation technology. The roots of aviation can be traced back to the inception of the Lighter Than Air Vehicle (LTAV). The LTAV has had significant utility throughout history. However, due to various functional disadvantages, the utility of LTAVs has been severely limited in the 21^{st} century.

This thesis is a successive iteration of research focused on a redefined potential for LTAV technology. The celestial Vacuum Lighter Than Air Vehicle (VLTAV) is an innovative design that is based on historical LTAV tenets paired with cutting-edge enhancements. The celestial VLTAV has the potential to surpass common functional disadvantages and provide a new paradigm for LTAVs. This chapter presents: the objective of the thesis research, the motivation behind the research, the historical background of the topic, and the previous research tied to the thesis.

1.2 Objective

The overall objective of this thesis is to analyze the behavior of additive manufactured (AM) rings under compression. The rings represent the individual members of the celestial icosahedron. A specific concern is the celestial's ability to withstand compressive loading. It serves as the structural housing for a VLTAV design and it is imperative to understand the behavior of it's geometry under external loading. The overall objective is broken down into a series of design objectives:

- Determine an appropriate cross-sectional thickness for the beam members of the celestial using classical solving methods.
- Additively manufacture rings out of ULTEM 9085 in three different orientations: 0°, 45°, 90°.
- Test each orientation in compression using an MTS machine and model the scenario in Finite Element Analysis (FEA) software.
- Identify the modulus of elasticity for the material, at each orientation, through comparison of FEA and experimental results.
- Compare the analytical results with the experimental results to characterize the nonlinear response.

1.3 Motivation

The celestial icosahedron is a potential candidate for the internal structure of the VLTAV. The VLTAV is a novel approach in the Unmanned Aerial Vehicle (UAV) design space. It has the potential to address shortcomings in current technology so that it can satisfy unique mission sets such as providing access to previously unreachable

places. A salient characteristic is its ability to dwell within a potentially harsh and corrosive environment for long durations to measure and record data.

The VLTAV concept does not rely on lifting gases or a propulsion system to stay aloft. It utilizes the inclusion of an internal vacuum surrounded by a robust and lightweight structure. This structure is wrapped with a thin-layered membrane that protects the internal cavity of the vehicle. This simple design provides the ability for the vehicle to stay aloft in an atmosphere for a long period without needing a resupply of energy. It allows for the safe inclusion of measurement devices such as sensors and gages to gather important data from the environment in which it is immersed. The membrane and structure provide protection to the onboard devices from the potentially corrosive external atmosphere. This allows for data to be efficiently harvested from austere regions and situations. The addition of a parachute could bolster the buoyancy of the VLTAV to allow it to dwell for extremely long durations within a specific environment.

A specific mission of interest is the investigation of the intensely hostile Venus atmosphere. Venus's atmosphere is extremely hot, turbulent, and filled with traces of highly reactive compounds such as sulfuric acid [1]. Due to its harsh nature, it is challenging to measure and record data throughout the Venus atmosphere. The VLTAV has the potential to be a suitable candidate for the safe collection of data from Venus such as wind speed, air composition, temperature, etc. The structure would safely harbor the required devices while the overall vehicle would be strong enough to withstand the turbulence.

Similar to the Venus mission, the VLTAV has potential to be dropped within violent weather events such as a tornado or a hurricane. It would function in the same capacity by collecting and transmitting data from within the storm cell. There is unlimited potential for the VLTAV concept. It has the capacity to achieve a unique

and unrivaled mission set.

1.4 Background

Humankind has been fascinated with the phenomena of flight as far back as history reaches. It is riddled throughout ancient mythology and legend, for example, the flight of Icarus and Daedalus that transpired through the use of melted wax and feathers as their means for escape from imprisonment [2]. Similar to the Greek myth, early humans sought to emulate the flight of birds by creating and testing wings to attach to the body [3]. These attempts were not successful but served as a stepping stone in the development of flight. Initially, manned flight found success using a uniquely different method from the winged approach: flotation. LTAV's ability to float is explained by Archimedes principle and gas laws.

LTAV.

The big and vibrant hot air balloons, often seen floating throughout today's skies, have humble beginnings. In a small town in southeastern France, two brothers experimented with making a small wooden box float. The Montgolfier brothers were on the cusp of a big discovery as they lit a fire underneath the cloth-covered box and made it rise to the ceiling of the room [4]. Unbeknownst to them, the brothers were utilizing Archimedes' principle to achieve buoyancy by heating the air underneath the box causing it to expand and become less dense. The difference in density allows the air to rise and provide an upward force to the cloth in order to lift the box. In 1783, the Montgolfier brothers scaled their experiment and created a 60,000 ft^3 balloon that successfully carried the first human airborne [4].

The Montgolfier brother's hot air balloons served as a starting point for the development of LTAV technology. Instead of heated air, lighter-than-air gases such as

hydrogen and helium were used to help keep balloons aloft longer [5]. In 1794, the technology was first utilized in warfare as a means of aerial reconnaissance in battles of the French Revolutionary War [6]. Balloons were successfully utilized for the same purpose by the Union Army in the American Civil War [6]. In World War I (WWI), the balloon was replaced with the airship as the predominant LTAV.

Airships are more versatile and lethal than the traditional flying balloon. They are equipped with motors or other mechanism for propulsion and navigation. This allows for the control of the ship in both the vertical and horizontal directions. Airships operate very much like the hot-air balloon by employing the use of a lifting gas within an envelope to achieve buoyancy. The envelope, or structure, can be rigid, semi-rigid, or non-rigid [7]. In WWI, airships were used for naval and land reconnaissance [8]. They were also used as instruments of deadly force by means of strategic bombing [8]. The airships of WWI effectively displayed the functionality of LTAVs.

The brief history of LTAVs provided in this section would not be complete without the mention of the "Father of Aeronautics". Francesco Lana de Terszi was a notable Italian scientist recognized for his accomplished works in mathematics and physics [9]. One noteworthy contribution is his theory of aerial navigation and the underlying mathematics that helped establish the science of aeronautics [9]. In 1663, Lana de Terzi presented the idea of a VLTAV. The concept was based on a vessel equipped with four copper spheres, as shown in Figure 1. In order to take flight, a vacuum would be drawn within each sphere to displace the volume of air within the spheres. This displacement would make the four spheres lighter than air and would cause the vessel to float.

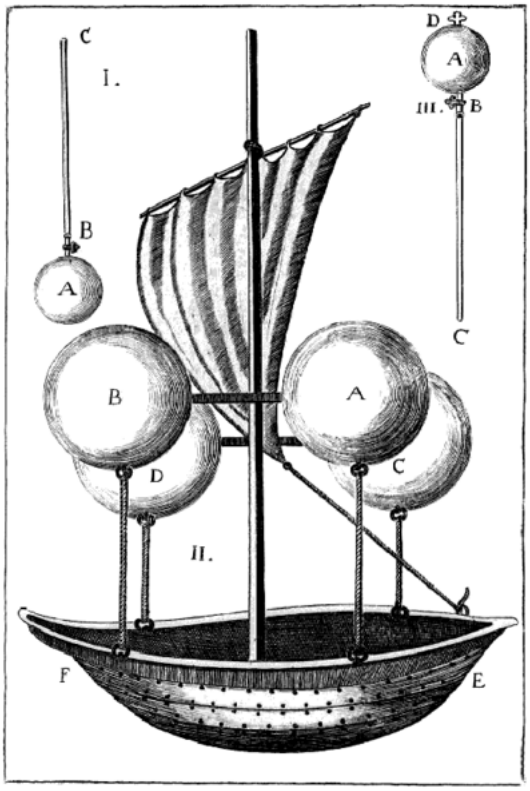

Figure 1. Francesco Lana de Terszi's conceptual design of a flying vessel that utilizes copper spheres for flotation [9].

The design was never built due to manufacturing limitations of the time. It would not have been capable of floating due to the external pressure on the copper spheres but the design proved to be a worthwhile thought experiment and inspiration to future generations. His pioneering work in aeronautics has significant influence on scientists, both in the past and present, in the field of lighter-than-air technology.

Archimedes' Principle.

LTAV's are able to "float", or be suspended in the air, due to a fundamental tenet within fluid mechanics called Archimedes' principle. Archimedes' principle states that the buoyant force (B) has a magnitude directed vertically upward, that is equal to the weight of fluid displaced by a submerged body [10]. A simple example is a piece

of driftwood floating on a lake. A small portion of the driftwood's body is submerged and the rest is exposed. The submerged portion displaces a volume of water. That volume has a magnitude of weight and it is equal to the buoyant force pushing upward on the driftwood. In this example, since the piece of wood is floating, B is equal to the weight (W) of the wood. The matter of buoyancy, or flotation, comes down to a simple force balance between W of a body and B.

The same phenomena experienced by the driftwood is also experienced by bodies in air. Air is significantly less dense than water. Therefore, it requires a large volume of air to be displaced, or for the "body" to be extremely light, in order to achieve buoyancy. A convenient relation used to characterize the buoyancy of an object is the weight-to-buoyancy (W/B) ratio. A low W/B ratio is desired if the object is intended to float. More specifically, a W/B less than 1 indicates positive buoyancy since B is greater than W of the object. Conversely, W/B greater than 1 will indicate negative buoyancy, or the inability to float. Lastly, a W/B ratio equal to 1 denotes neutral buoyancy.

A LTAV must not weigh very much in order to achieve a W/B ratio equal to or less than 1. The VLTAV is an ideal derivative of the LTAV because it relies on an internal vacuum as it's mechanism for lift. Theoretically, the weight of the internal volume would be weightless since it is completely devoid of air. The structure and the membrane would be the only components contributing to the vehicle's weight. This poses a difficulty in the design of the vehicle's structure; it must be lightweight but also strong enough to handle external pressure loading from the atmosphere. This loading is created by the difference in pressure between the internal vacuum and the surrounding atmosphere. Lana de Terzi's VLTAV, shown in Figure 1, featured sphere's made of thin copper as the lifting mechanism. If a vacuum was successfully drawn in a sphere, the compressive loading from the atmospheric pressure would've

caused the sphere to buckle. This conclusion is brought forth by the analysis done by Akhmeteli and Gavrilin, in which, it is mathematically supported that: "no known material can be used to create a vacuum balloon made from a homogeneous wall structure" [11]. This phenomena must be appropriately addressed if the VLTAV is to be transformed from a conceptual design to an operational entity.

1.5 Previous Research

The success of a VLTAV hinges on the design of a functional structure to serve as the vehicle's frame. It has been proven that a spherical, thin-layered homogeneous frame is insufficient in withstanding the compressive loading imposed by the atmosphere [11]. An ideal frame for the VLTAV must be structurally stable under loading while being light enough to promote positive buoyancy. At the Air Force Institute of Technology (AFIT), an abundance of research has been focused on this twofold problem. The following serves as a brief overview of the investigations conducted at AFIT.

In 2012, Trent Metlen sought a design that would be sufficient to achieve positive buoyancy while also maintaining structural integrity. He investigated a method to geometrically stiffen a sphere to accomplish this feat [12]. His work brought forth a unique model that had potential in satisfying the problem at hand: the icosahedron. The icosahedron is a geodesic polyhedron that is composed of 20 equilateral triangles [12], [13]. As shown in Figure 2, the vertices of the icosahedron pass through points that make up a sphere. This is important because a spherical body is the optimal shape for the VLTAV. It offers the largest amount of internal volume, to draw a volume of air from, for the smallest surface area [14],[15]. This relationship allows for maximum lift potential and structural integrity.

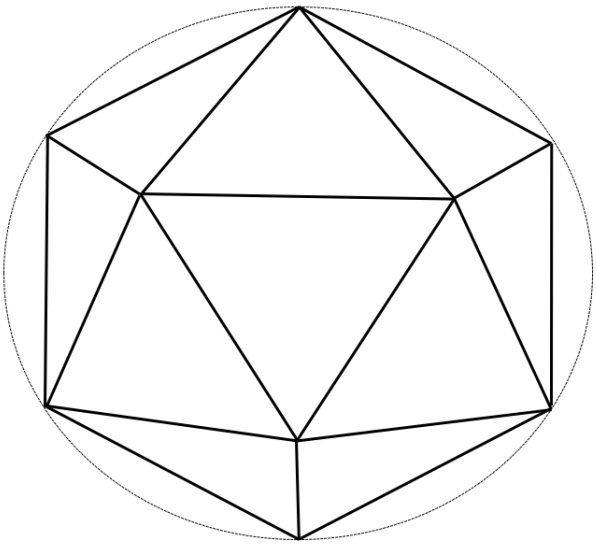

Figure 2. Basic icosahedron with a spherical outline connecting the outer vertices.

It can be seen, by inspection of Metlen's icosahedron, that if the size of the triangles that make up the body were to decrease in size and increase in number, then the overall shape of the structure would approximate a sphere more accurately. A derivative of this notion, the hexakis icosahedron, is pictured in Figure 3. The hexakis was examined in depth by Cranston; it is composed of 120 scalene triangles and 62 vertices [16].

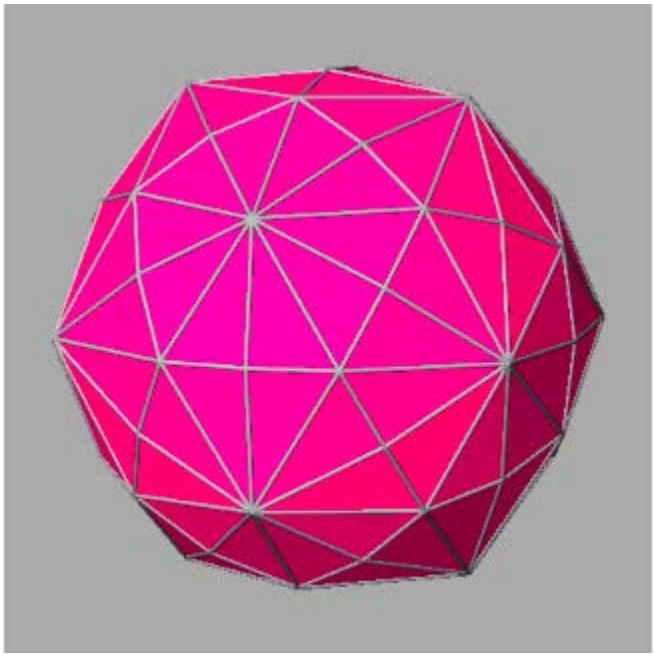

Figure 3. Hexakis icosahedron from Cranston [16].

Cranston's hexakis icosahedron is a closer approximation of a sphere than Metlen's hexakis, thus indicating the hexakis has more internal volume. This allows for more air to be evacuated and aids in the buoyancy properties. In addition to its increased buoyancy potential, the hexakis proved to be more structurally feasible and capable of enduring loads [16]. In search of increasing this trend in performance, Cranston considered a third configuration: the celestial icosahedron.

The celestial icosahedron has nine intersecting curved rings that are oriented in three directions with respect to the horizontal plane: 0°, 45°, and 90° [14],[15]. A frontal view of a 3D printed celestial, accompanied by a schematic of the ring orientations, offers a more concise representation of the structure's composition in Figure 4 and 5. It is clear that the celestial design takes on a spherical shape. Of the three designs, it is the ideal configuration in regards to W/B since it can evacuate the largest amount of air.

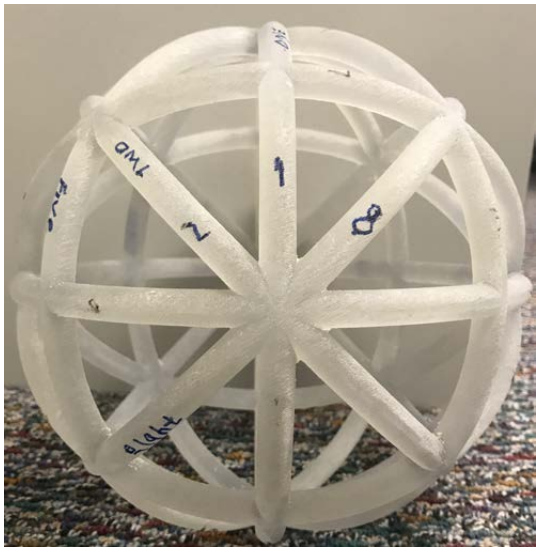

Figure 4. Frontal view of 3D printed model of celestial icosahedron showing the ring orientations.

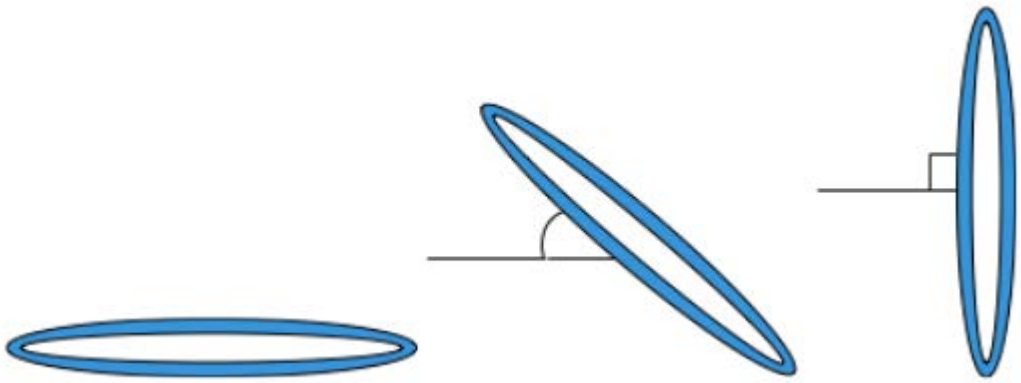

Figure 5. Schematic of the ring orientations that makeup the celestial: 0° (left), 45° (center), 90° (right).

Extensive analysis has been conducted for each frame considered. A key point of interest is the behavior of the structure under loading. As discussed previously, the structure must keep its W at a minimum which requires the use of slender beams and lightweight material. A stable frame is imperative to the success of a VLTAV.

Cranston and AlGhofaily experimentally determined the stability and buckling behavior of Metlen's icosahedron using an MTS machine [17]. As mentioned previously, Metlen's icosahedron has less potential in achieving positive buoyancy as compared to

the celestial. The instability of the celestial has yet to be investigated experimentally. A proper analysis would provide essential information in regards to the celestial's potential as a proper frame for the VLTAV. The following thesis aims to satisfy the questions involving the celestial icosahedron's instability under compressive loading.

1.6 Thesis Outline

- Chapter I: Thesis objective, motivation, background, and previous research.
- Chapter II: Analysis of relevant literature/research concerning nonlinearity, AM, and FEA.
- Chapter III: Design process, AM techniques, experimental and finite element model setup.
- Chapter IV: Presentation of experimental and theoretical results.
- Chapter V: Summary of results, conclusions, and future research recommendations.

II. Theoretical Framework

2.1 Chapter Overview

The objective of this thesis is to investigate the instability of the members of the celestial icosahedron, both experimentally and analytically. The celestial must be properly sized, manufactured, and tested in compression, to satisfy the research objectives. FEA is required to aid in the characterization of both the material and response for the celestial. In order to conduct the research at hand, an awareness of the underlying principles present throughout the work is required. This chapter provides a brief, but comprehensive, introduction to the theoretical framework that supports the research and its various components. It focuses on nonlinear behavior, FEA, and AM.

2.2 Fundamental Theory

The major disciplines that makeup the theory behind this particular research are interconnected. This research is nested within the field of continuum mechanics, more specifically, solid mechanics. Each research component is incomplete without the proper consideration of the specific tenets with solid mechanics. A few major tenets of consideration for this research includes beam-column relations, stability, material properties, and numerical approximation methods.

2.3 Nonlinear Behavior

A common assumption made in the analysis of problems, within structural mechanics, is to neglect nonlinear effects. Although nonlinear effects, or nonlinearity, is present in all problems they can be reasonably ignored if the effects are small [18]. Cook et al. defines nonlinearity as a phenomenon in which the "response is

not directly proportional to the action that produces it". There are multiple types of nonlinear effects that can be present within a given problem, however, this research is mainly concerned with the effects geometric nonlinearity.

Effects from geometric nonlinearity are pertinent when displacements, rotations, or strains are not infinitesimal [19]. The main tenet of this research involves the uniaxial compression of rings. The imposed displacement is significant in magnitude, especially in comparison to the ring's thickness (t). This drives the notion that geometric nonlinear effects must be accounted for within the analysis. Figure 6 serves as a basic summary of the process, in which a load (P) is applied to the structure that causes a significant displacement (u). The output response is nonlinear, as shown in the plot of Figure 7.

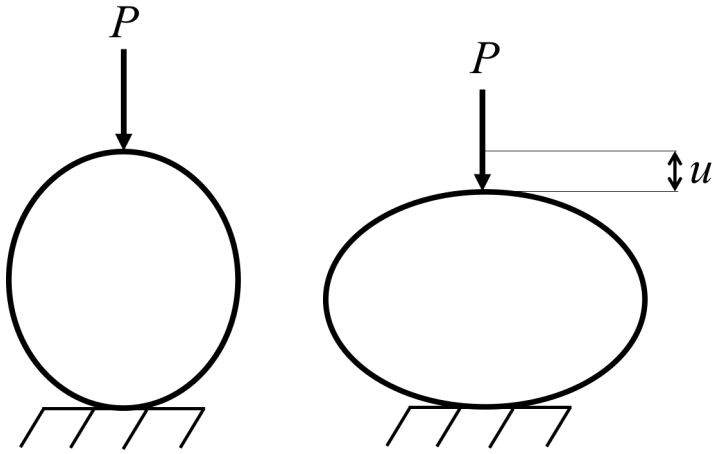

Figure 6. Basic schematic of a ring structure exhibiting nonlinear behavior due to P.

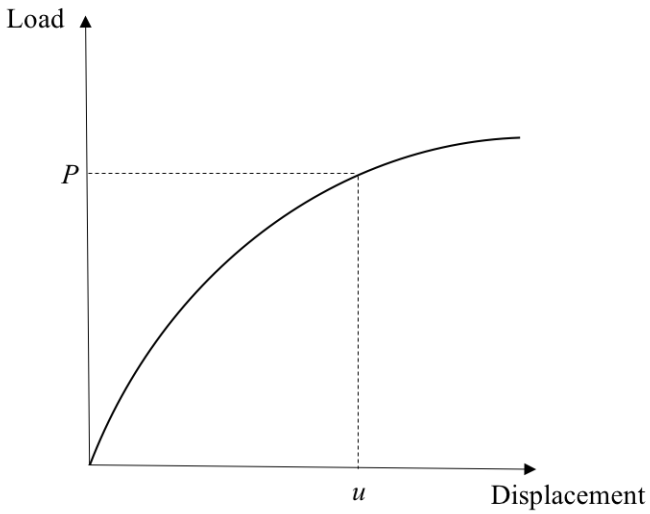

Figure 7. Nonlinear relationship of P vs u [20].

Nonlinearity increases the complexity of finding a solution and requires appropriate analysis techniques. FEA is a robust computational tool for solving many complex problems–including nonlinear problems. If nonlinear effects are to be included, care must be taken by the user to ensure the proper analysis technique is setup correctly. A powerful, and widely used, solving approach used to solve nonlinear problems is the Newton–Raphson method (NR). NR is the technique utilized for this research and is described in depth in a subsequent section.

2.4 FEA

FEA, or the finite element method (FEM), was first developed in the aerospace industry as a computational tool for the analysis of large structures [21],[22]. Since its inception, FEA has advanced to be a computational aid for many disciplines. For the purpose of the work provided in this thesis, the use of FEA is concerned with its initial design purpose–structural analysis. At its core, FEA is a method for numerical solution of field problems [18]. A field problem is mathematically expressed as a differential equation or integral expression [18]. Field problems related to mechanical

stress analysis are of concern for this particular thesis. FEA is capable of solving time-dependent or time-independent problems along with linear and nonlinear problems. Generally, it is divided into three main operations: pre-processing, numerical analysis, and post-processing [18]. The following provides a brief overview of FEA and its use in structural analysis.

Modeling & Preprocessing.

In FEA, the initial step is identification of the problem and the results in which the analysis is expected to produce. For example, a problem may concern the bending of a beam due to transverse loading. Is the propagation of stress throughout the beam the desired result? Or is the total strain desired? Is it linear, time-dependent, or both? The specific characteristics of the model must be addressed in the model setup, or preprocessing stage. The complexity of the model and corresponding level of accuracy are directly proportional to the time required for model setup and for processing.

Once the problem is sufficiently identified, the model is setup in the FEA software. In computational structural analysis, the model is strictly a mathematical representation of a physical entity. Governing equations are devised based on the specifications input by the user. First, the geometric parameters that define the entity are formed within the software and can be modeled according to a specific dimensionality (1D, 2D, or 3D). Constraints specific to material properties such as isotropy, homogeneity, and linear-elastic (nonlinear and/or inelastic) behavior, are built in to the model definition. Next, the boundary conditions and loads are considered. These serve as approximate, or ideal, representations of the conditions in which the model is subject to in a realistic environment, as defined by the user.

The most intensive, but crucial, step in FEA is the definition of the mesh. A mesh

is an interconnected grid composed of finite elements that include formulations and restrictions specific to the model. The elements are connected to one another at nodes to makeup the mesh. Elements vary in composition and functionality depending on the type of problem and desired solution at hand. Element designations are specific to the FEA program in use; the remainder of this discussion will reference formulations specific to Abaqus CAE element library. An example of a planar beam element is shown in Figure 8. This element has the designation of "B21", which signifies that it is a beam element in planar space (2D) and is linear [20]. It has two nodes–one at each end of the element. Each node has two degrees of freedom (DOF)–one in translation and one in rotation, as depicted in Figure 8 [18]. Characteristics such as

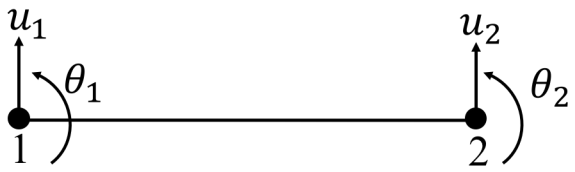

Figure 8. A B21 element, which is a two-node linear beam element [18].

"beam", "linear", or "two-node", are unique to the type of element being used and represent the types of constraints or limitations that can applied to the model. These are just a few examples of many different types of element characteristics. A more complex element, the C3D8, is depicted in Figure 9. A C3D8 element is a linear brick element with eight nodes; it is a continuum stress/displacement element in 3D [20]. It has three DOF per node for a total of 24 DOF per element [18].

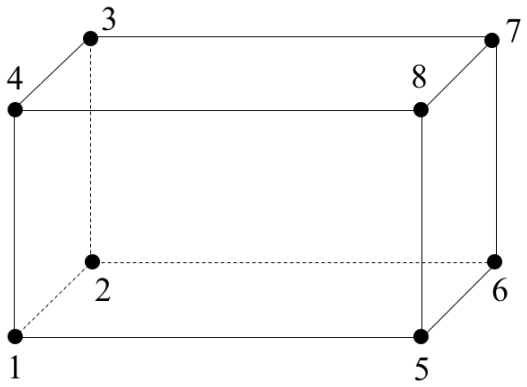

Figure 9. A C3D8 element, which is an eight-node linear brick element.

The B21 and C3D8 elements are two examples of element types that can be used to outfit a model. There is an extensive library of element types and each type comes with specific capabilities and limitations. Once the specific element type(s) are decided, the mesh can be generated for the model via discretization.

The essence of FEA, as stated by Cook et al, is "approximation by piecewise interpolation of a field quantity" [18]. The mesh is a mathematical model that consists of a piecewise continuous field that characterizes a fully continuous field [18]. This continuous piecewise field is defined by the quantity of nodes and interpolation within each element [18]. Therefore, discretization is the mathematical division of a model into a defined number of elements, in which, the elements are connected by a continuous piecewise field at designated nodal locations. The field variable of interest (e.g. mechanical stress σ is approximated by the connection of interpolation functions for each finite element [18]. The functions are adjusted specifically to the nodal locations inherent to the designated element type.

Numerical Analysis.

Numerical analysis is the second major step of an FEA routine. The analysis route is complex and can be tailored specifically to a desired problem or outcome. A low-

level summary of the numerical analysis step is provided in the following passage; the reader is encouraged to seek out the indicated references for a more detailed, holistic discussion on FEA numerical solvers. The work for this thesis utilizes nonlinear analysis via Abaqus/Standard.

In general, specific field quantities serve as the desired output of an FEA model subject to a set of boundary conditions, loads, material behavior, etc. The output is generated by the preset solving techniques within the FEA software. This process involves the creation of an immense matrix equation representative of the entire structure [23]. The matrix equation is reduced from a series of partial differential equations (PDE) [24]. The matrix equation is subdivided into smaller matrices that identify the specific behavior of each element [23]. The encompassing matrix equation is solved to determine the field quantities at the nodal locations throughout the structure [23].

Abaqus/Standard uses implicit integration for solving. The implicit method solves for the field quantities, or unknowns, that are nested within the matrix equation, through matrix inversion [24]. In a nonlinear problem, an iterative approach is required; the problem is broken up incrementally and the current solution relies on the solution of the previous step, or increment [24]. The nonlinear solving routine is discussed in greater detail in the following section.

Nonlinear Analysis.

Abaqus/Standard employs the NR method to execute nonlinear analysis. NR, or commonly referred to as Newton's method, is a numerical procedure that converges to a solution through approximation and iteration. Convergence is based on the tolerance limit, or proximity of the approximation to the final solution. The NR method will continue iteration until it has satisfied the set tolerance or if it exceeds

maximum iterations. The NR method is generally quick to converge and is highly efficient in solving large, nonlinear computations [25]. The basic, governing formula of the NR method is given in Equation 1 [26]:

$$x_{k+1} = x_k - \frac{f(x_k)}{f'(x_k)} \tag{1}$$

The most pertinent example of the NR method is its employment by Abaqus to solve nonlinear structural analysis problems. In a nonlinear analysis, Abaqus breaks up the simulation into a number of time increments and solves for an approximate equilibrium solution at the end of each increment [20]. This approximation must satisfy a defined tolerance and, therefore, may result in multiple iterations within one increment, in which, the NR technique is employed. In a nonlinear analysis simulation, convergence is attained when equilibrium is established [20]. The following example, adapted from the Abaqus User's guide, attempts to summarize the NR technique in solving a nonlinear load-displacement problem [20].

Abaqus/Standard is theoretically used to capture the structure's response to P. The external load creates stresses within the elements that compose the structure and these stresses transmute to internal forces (I) at the nodes [20]. A balance between the external and internal loads must be achieved in order to establish equilibrium. The total load is broken into a smaller portion of the load (Δ_P) with an initial displacement (u_0). The NR method utilizes the structure's stiffness K at u_0 to calculate a displacement correction (c_a) [20]. The value of K_0 is found from the tangent line, or slope, at the point of u_0. Through the use of c_a, the structure's displacement is adjusted to a displacement of u_a. At this new location, the internal nodal forces are updated. The force residual (R_a) is calculated by taking the difference between the

total force P and the updated I.

$$R_a = P - I_a \tag{2}$$

R_a is checked against the set tolerance for the force residual at all nodes [20]. If the calculated R_a is less than the tolerance, equilibrium has been established and u_a is accepted as an appropriate configuration for the structure [20]. The routine must check an additional parameter before convergence can be declared for the step: the magnitude of c_a must be small compared to the magnitude of the displacement from u_0 to u_a.

$$\Delta u_a = u_a - u_0 \tag{3}$$

$$|c_a| << |\Delta u_a| \tag{4}$$

The Abaqus User's Manual states: "If c_a is greater than a fraction (1% by default) of the incremental displacement, Abaqus/Standard performs another iteration." Convergence is not obtained until both the tolerance and the additional check are satisfied. A solution, within an iteration, that does not converge requires a second iteration with the objective of balancing the internal and external forces [20]. Similar to the process of the first increment, a new K_a is created from the position u_a. K_a, coupled with a new residual, R_a, corrects the configuration by the displacement c_b in an attempt to satisfy equilibrium. A graphical representation of the first iteration within an increment is shown in Figure 10. The second iteration is shown in Figure 11.

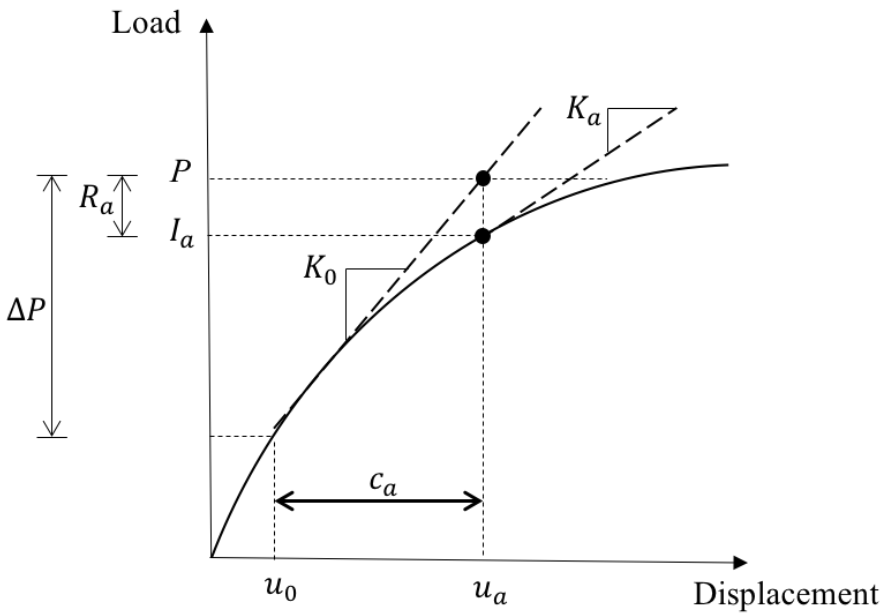

Figure 10. Depiction of the initial iteration in NR analysis for the P vs u example [20].

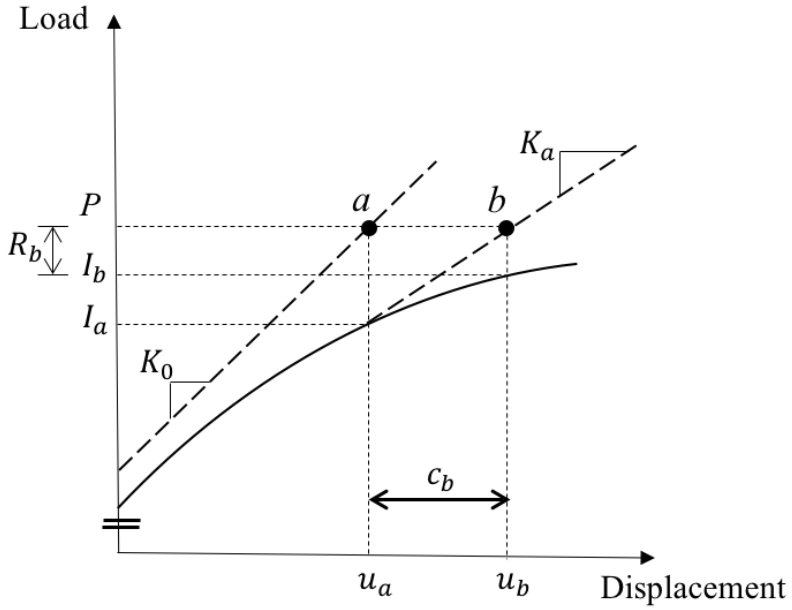

Figure 11. Second iteration of NR analysis in attempt to bring the system closer to equilibrium [20].

The preceding section is a simplified example of the NR technique employed by Abaqus/Standard to acquire a solution for a nonlinear problem. The given example is

a basic introduction to the NR solver. There are varying degrees in which the routine can be modified according to the type of problem and solution desired by the user. It is a powerful solving technique and provides an effective means for the exploration of nonlinear phenomena.

2.5 Beam Sizing

The celestial icosahedron is composed of nine intersecting rings. The design at hand assigned an outer diameter of 0.2032 m for each ring. This dimension was first based on a previously manufactured design by Moore, shown in Figure 12. Moore's 3D printed celestial features an outer diameter of 0.1905 m and was manufactured as a visual aid and proof of concept. Ultimately, the overall dimension was assigned in order to comply with the dimensionality of the AM and testing facilities.

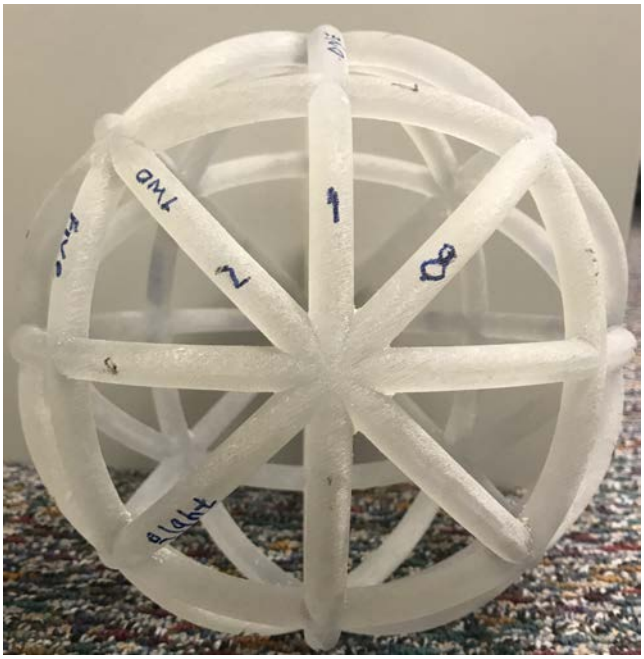

Figure 12. Moore's 3D printed, 0.1905 m-diameter celestial icosahedron has a t of 9.53 mm.

The current design utilizes an 0.2032 m diameter for simplicity in analysis and manufacturability; it can easily fit within the testing rig and 3D printer. This partic-

ular size enables the manufacture of multiple rings to be fit in one build plate which saves both time and energy. The AM process is discussed in greater detail in a subsequent section. The design required an appropriate cross-sectional thickness for the members so that it can withstand a prescribed loading scenario. In order to satisfy this requirement, an analysis was required that employed classical structural analysis techniques provided by Saada [27].

Beam-Column Loading.

A beam-column is a member that is loaded both in the axial direction and in the transverse direction. This loading arrangement places the member in both compression and bending. A beam-column subject to multiple concentrated loads is depicted in Figure 13.

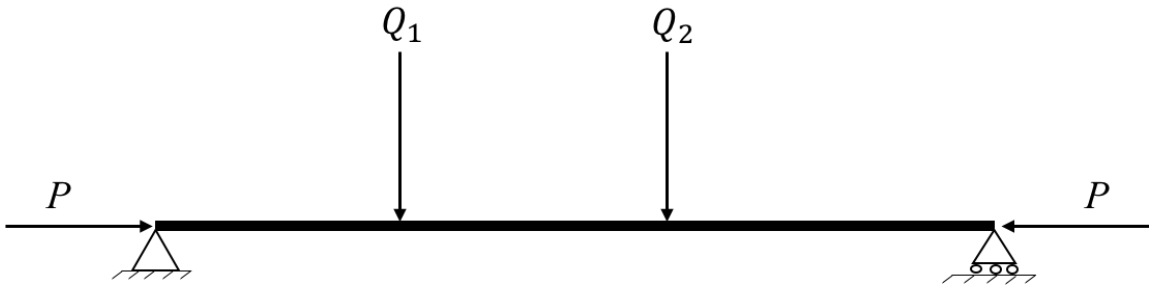

Figure 13. Beam-column with multiple concentrated loads (Q) in the transverse direction in conjunction with an axial load (P).

To find an appropriate t, a small beam section of the celestial was treated as a beam-column under a distributed triangular load offset from the center of the span (Figure 14). An equivalent load was determined by considering sea-level pressure acting on one triangular area of the celestial. This area is highlighted in Figure 15.

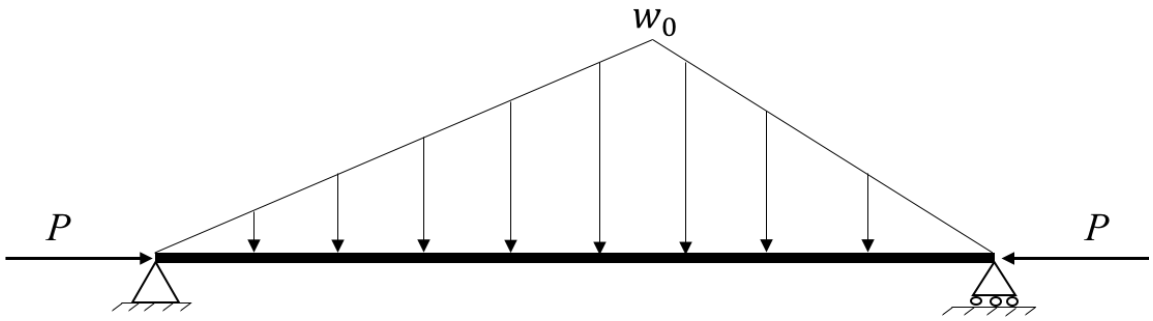

Figure 14. Beam-column with offset triangular loading.

In order to determine the equivalent line load, the coordinates at each vertex point within the blue triangle of Figure 15, were recorded from the SolidWorks part file. The triangular area was split into two identical right triangles. The coordinates were used to find the center of gravity (CG) of one of the right triangles by determining the lengths of each side. These lengths were used to reconstruct the triangle as a planar geometry with the assumption that the effects of the curvature of the actual members is negligible.

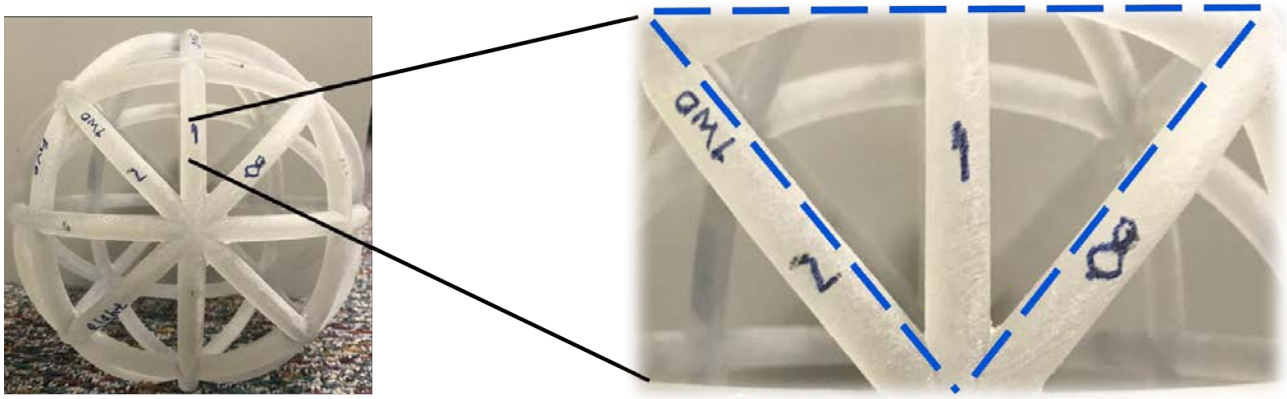

Figure 15. Triangular region of the celestial in which the pressure loading value was analyzed.

After the CG was determined, a straight line was dropped from the CG to a leg of the triangle, denoted d_1 in Figure 16.

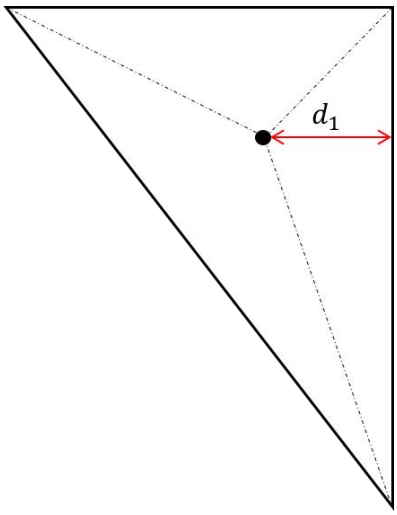

Figure 16. d_1 **- the distance between the CG and vertical leg of the triangle.**

The length of d_1 was determined by the law of cosines and right triangle relations to be 21.62 mm. d_1 was used to find the equivalent triangular line load (w_0) from the pressure applied across the triangular region. Sea-level pressure was used for analysis: 101,325 Pa. w_0 was ultimately determined by the relation given below in Equation 5; P is pressure, d_1 is the shortest distance from the CG to the vertical leg, and the factor of 2 accounts for the contribution of both right triangles within the region of interest.

$$w_0 = 2Pd_1 \tag{5}$$

Now that the value of w_0 is known, the beam-column analysis for an offset triangular line load was derived to determine an adequate t for the beam. In the derivation, the line load is presumed to be acting on the vertical beam member, labeled "1" in Figure 15. It's length (L) was determined using the law of cosines and given coordinates. The triangular load was broken up into two portions: left and right. This separation stems from the intersection point of d_1 and the vertical beam member. The left-hand side spans from $0 < x1 < 0.65L$, while the right-hand side spans from $0.65L < x1 < L$. A schematic of this division is shown in Figure 17.

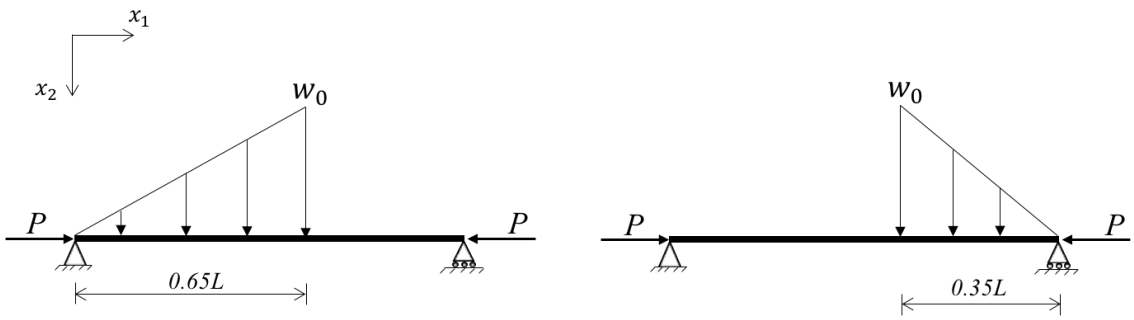

Figure 17. Beam-column with triangular line load divided into left and right portions.

Ultimately, the analysis treated the member as a beam-column with several concentrated loads and utilized the principle of superposition to conjoin the response from the left and right regions [27]. The triangular loads were broken into their respective resultant loads in order to define the governing differential equations.

The resulting equations contained constants of integration (e.g., C_1-C_4), that were found using the method of undetermined coefficients [28]. Once the constants were defined, the equations that characterized the two portions of the beam were combined using the principle of superposition. This determined the deflection of the member at any point due to the loading scheme [27]. This analysis is discussed in detail in the following section.

Beam-Column Analysis Method.

The reaction forces and moments were found for the portion of the beam-column, in which the triangular line load acting across the span was equivalent to the $0 < x1 < 0.65L$ segment of the entire triangular load (Figure 18).

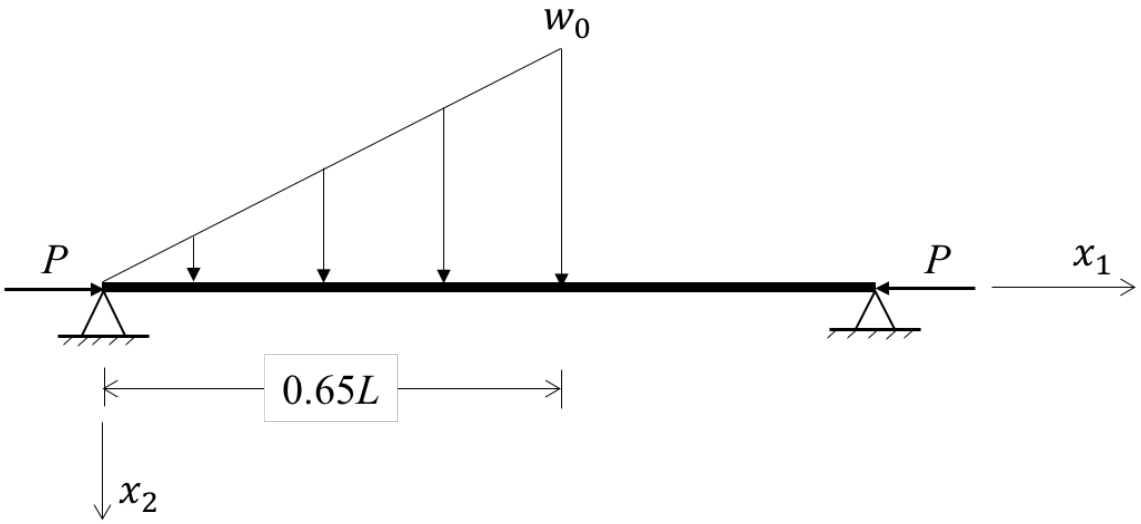

Figure 18. Beam-column with triangular line load divided into left portion.

This was accomplished by first analyzing the free body diagram (FBD). The reaction forces (R_A, R_B) were found to be:

$$R_A = \frac{169}{1200} L w_0 \tag{6}$$

$$R_B = \frac{221}{1200} L w_0 \tag{7}$$

Next, the sum of moments was taken about the right side to find the moment (M_1) at a distance x_1 from the left side.

$$M_1 = \frac{221}{1200} L w_0 x_1 - \frac{10 w_0 {x_1}^3}{39L} + P u_2 \tag{8}$$

The moment-curvature relationship is defined in Equation 9.

$$M = -EI \frac{\partial^2 u_2}{\partial {x_1}^2} \tag{9}$$

Equation 9 was substituted for M_1 along with a substitution of K, which is defined

as:

$$K^2 = \frac{P}{EI} \tag{10}$$

The result is a differential equation of the form:

$$\frac{\partial^2 u_2}{\partial {x_1}^2} + K^2 u_2 = \frac{1}{EI}\left(\frac{10 w_0}{39L}{x_1}^3 - \frac{221 L w_0}{1200} x_1\right) \tag{11}$$

Equation 11 was solved using the method of undetermined coefficients to find a relation for the vertical deflection (u_2). The solution consisted of the sum of the particular component (u_{2p}) and complementary component (u_{2c}).

$$u_2 = u_{2c} + u_{2p} \tag{12}$$

The general form used for u_{2c} included two coefficients (C_1,C_2) in the arrangement:

$$u_{2c} = C_1 sin(K x_1) + C_2 cos(K x_1) \tag{13}$$

u_{2p} consisted of four different coefficients (A,B,C,D):

$$u_{2p} = A{x_1}^3 + B{x_1}^2 + C x_1 + D \tag{14}$$

The coefficients in u_{2p} were solved for with the aid of MATLAB (Appendix A).

$$A = \frac{10 w_0}{39 EILK^2} \tag{15}$$

$$B = 0 \tag{16}$$

$$C = \frac{-w_0\left(2873 K^2 L^2 + 24000\right)}{15600 EILK^4} \tag{17}$$

$$D = 0 \tag{18}$$

The coefficients were plugged back into Equation 14. u_{2p} was then inserted into Equation 12. A relation for u_2 for the $0 < x1 < 0.65L$ portion of the beam (u_2L) was found by applying the following boundary condition for the left side of the beam-column:

$$x_1 = 0 \tag{19}$$

$$u_2 = 0 \tag{20}$$

This condition allowed for C_2 to be solved for directly.

$$C_2 = 0 \tag{21}$$

As a result, Equation 12 was rewritten as:

$$u_2L = C_1 sin(Kx_1) + \left(\frac{10w_0}{39EILK^2}\right) {x_1}^3 - \left(\frac{w_0\left(2873K^2L^2 + 24000\right)}{15600EILK^4}\right) x_1 \tag{22}$$

The reaction forces and moments were found for the $0.65L < x1 < L$ portion of the same beam-column. The resulting moment (M_2), acting at a section within the $0.65L < x1 < L$ portion was found to be:

$$M_2 = \frac{169}{1200} w_0 L^2 - \frac{169}{1200} w_0 L x_1 + P u_2 \tag{23}$$

Another second-order differential equation was developed by following the same substitutions as the previous formulation.

$$\frac{\partial^2 u_2}{\partial {x_1}^2} + K^2 u_2 = \frac{1}{EI}\left(\frac{169}{1200} w_0 L x_1 - \frac{169}{1200} w_0 L^2\right) \tag{24}$$

This equation was solved using the same method as the previous formulation. The

result was a definition for the deflection of the right side of the beam-column (u_2R).

$$u_2R = C_3sin(Kx_1) + C_4cos(Kx_1) + \left(\frac{169w_0L}{1200EIK^2}\right)x_1 - \left(\frac{169Lw_0\left(LK^2+1\right)}{1200EIK^4}\right) \quad (25)$$

The following boundary condition, for the right side of the beam, was applied to solve for C_4:

$$x_1 = L \quad (26)$$

$$u_2 = 0 \quad (27)$$

$$C_4 = \frac{\left(\frac{169Lw_0}{1200EIK^4} - C_3sin(KL)\right)}{cos(KL)} \quad (28)$$

C_4 was plugged back into u_{2R} (Equation 25):

$$u_{2R} = C_3sin(Kx_1) + \frac{(cos(Kx_1)(169Lw_0 - 1200C_3EIK^4sin(KL))}{1200EIK^4cos(KL)} + ... \\ \frac{169Lw_0x_1}{1200EIK^2} - \frac{169Lw_0(LK^2+1)}{1200EIK^4} \quad (29)$$

For this analysis, the beam-column was broken up into two portions but it still functions as a continuous entity. Therefore, it shares the same u_2 at the point in which the regions were separated. This continuity creates the following boundary conditions:

$$x_1 = 0.65L \quad (30)$$

$$u_{2R} = u_{2L} \quad (31)$$

$$x_1 = 0.65L \quad (32)$$

$$\left(\frac{\partial u_2}{\partial x_1}\right)_L = \left(\frac{\partial u_2}{\partial x_1}\right)_R \quad (33)$$

Using the two boundary conditions, the three unknown constants C_1, C_3, and C_4 were found and plugged back into Equations 22 and 29 to fully define the u_2 for the entire span of the beam that is subjected to the portion of triangular load highlighted in Figure 18.

A similar approach was followed for a beam-column subject to a triangular line load, with intensity w_0, across the $0.65L < x1 < L$ span of the beam. The scenario is depicted in Figure 19.

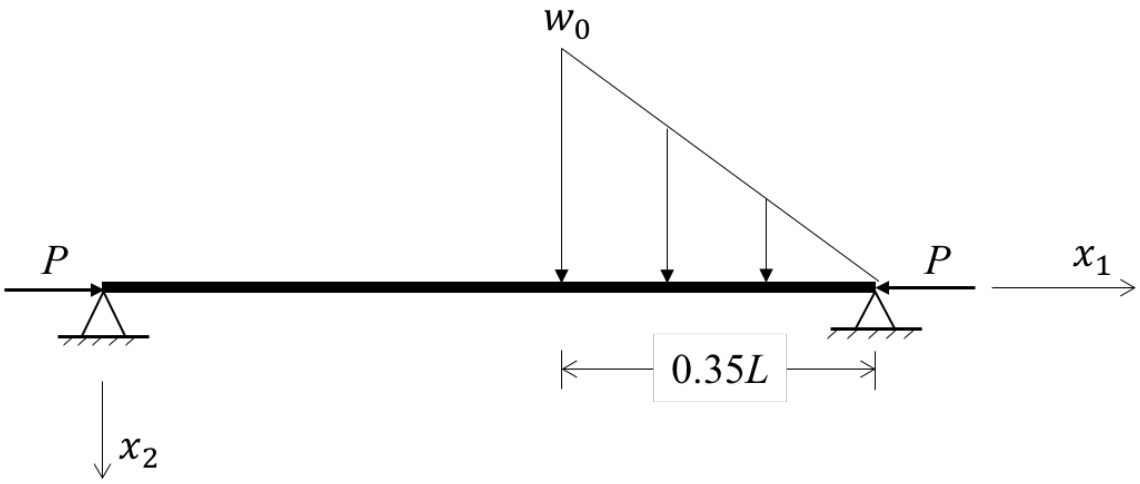

Figure 19. Beam-column with triangular line load divided into right portion.

First, the $0 < x1 < 0.65L$ region of the beam was analyzed to find the internal moment (M_1) at a distance x_1 from the left side.

$$M_1 = \frac{49Lw_0}{1200}x_1 + Pu_2 \tag{34}$$

The appropriate substitutions were made to develop the governing differential equation.

$$\frac{\partial^2 u_2}{\partial {x_1}^2} + K^2 u_2 = -\left(\frac{49Lw_0}{1200EI}\right)x_1 \tag{35}$$

The method of undetermined coefficients was applied, along with the following bound-

ary condition, to define u_{2L}.

$$x_1 = 0 \tag{36}$$

$$u_2 = 0 \tag{37}$$

$$u_{2L} = C_1 sin(Kx_1) - \left(\frac{49Lw_0}{1200EIK^2}\right) x_1 \tag{38}$$

Next, the the $0.65L < x1 < L$ region of the beam was considered. The internal moment (M_2) was found to be:

$$M_2 = \frac{1}{8400L}\left[-2873w_0L^3 + 10873w_0L^2x_1 - ... \right.$$
$$\left. 12000w_0L{x_1}^2 + 8400Pu_2L + 4000w_0{x_1}^3\right] \tag{39}$$

The proper substitutions were made in Equation 39 to develop the differential equation.

$$\frac{\partial^2 u_2}{\partial {x_1}^2} + K^2u_2 = \frac{1}{8400L}\left[-2873w_0L^3 + 10873w_0L^2x_1 - ... \right.$$
$$\left. 12000w_0L{x_1}^2 + 8400Pu_2L + 4000w_0{x_1}^3\right] \tag{40}$$

The method of undetermined coefficients was applied, along with the following boundary condition, to define u_{2R}.

$$x_1 = L \tag{41}$$

$$u_2 = 0 \tag{42}$$

$$u_{2R} = -\frac{1}{8400EIK^4Lcos(KL)}\left[24000Lw_0cos(KL) - 24000w_0x_1cos(KL) - ...\right.$$
$$2873K^2L^3w_0cos(KL) + 4000K^2w_0{x_1}^3cos(KL) - 12000K^2Lw_0{x_1}^2cos(KL) + ...$$
$$\left.10873K^2L^2w_0x_1cos(KL) + 8400C_3EIK^4Lsin(K(L-x_1))\right] \quad (43)$$

The boundary conditions defined in Equations 30 and 32 were applied to solve for the three constants: C_1, C_3, and C_4. Consequently, a relation for u_{2L} and u_{2R} were found.

$$u_{2L} = -\frac{w_0}{8400EIK^5Lsin(KL)}\left[343K^3L^2x_1sin(KL) - ...\right.$$
$$\left.24000sin\left(\frac{7KL}{20}\right)sin(Kx_1) + 8400KLcos\left(\frac{7KL}{20}\right)sin(Kx_1)\right] \quad (44)$$

$$u_{2R} = \frac{w_0}{8400EIK^5Lsin(KL)}\left[12000cos\left(\frac{K(7L-20x_1)}{20}\right) - ...\right.$$
$$12000cos\left(\frac{K(33L-20x_1)}{20}\right) + 2873K^3L^3sin(KL) - ...$$
$$4000K^3{x_1}^3sin(KL) - 2400KLsin(KL) + ...$$
$$24000Kx_1sin(KL) + 4200KLsin\left(\frac{K(7L-20x_1)}{20}\right) + ...$$
$$4200KLsin\left(\frac{K(33L-20x_1)}{20}\right) + ...$$
$$\left.12000K^3L{x_1}^2sin(KL) - 10873K^3L^2x_1sin(KL)\right] \quad (45)$$

The principle of superposition was used to establish u_2 for the entire beam-column subject to the full triangular line load. The beam is broken into two regions (I,II) as shown below in Figure 20.

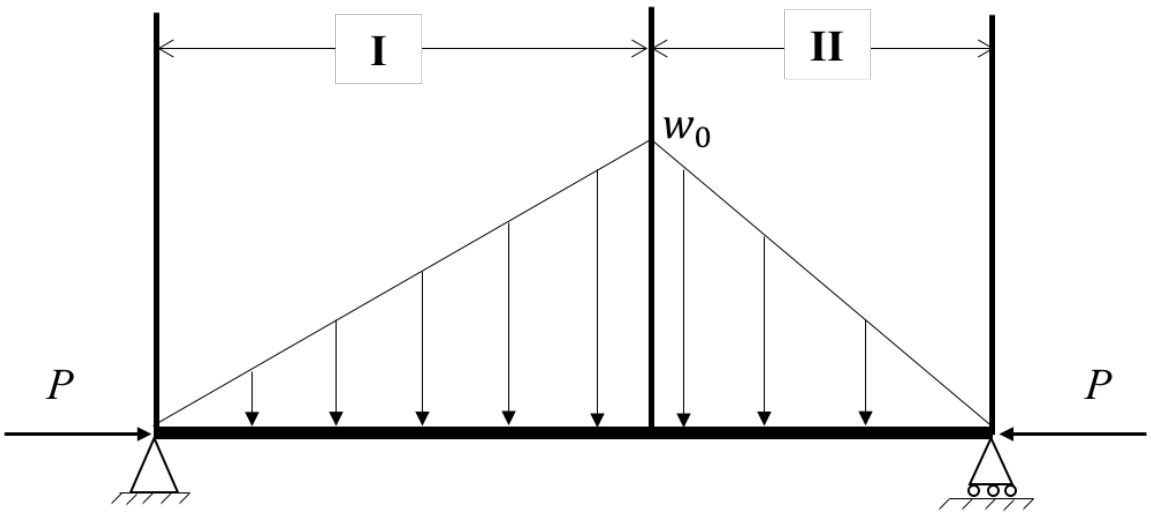

Figure 20. Beam-column divided into two regions: I and II.

For region I, the u_{2L} relations from Equation 22 and 44 were added together. The same was done for region II. Numerical values were substituted for the variables into these new relations to investigate which region the maximum vertical displacement occurred.

$$c = 0.00342\ m$$

$$E = 4,371\ MPa$$

$$w_0 = 4,379\ \frac{N}{m}$$

$$L = 0.0777\ m$$

$$P = 342\ N$$

The value for c was taken from a rudimentary analysis of the beam-column subjected to a series of concentrated forces equivalent to a crude distribution of w_0. E was the average of the published values for the compressive E of ULTEM 9085 [29]. The value of P was the adjusted magnitude of axial force from previous research

[17]. The deflection for each portion of the beam is shown in Figures 21 and 22. The deflection for the entire beam is shown in Figure 23.

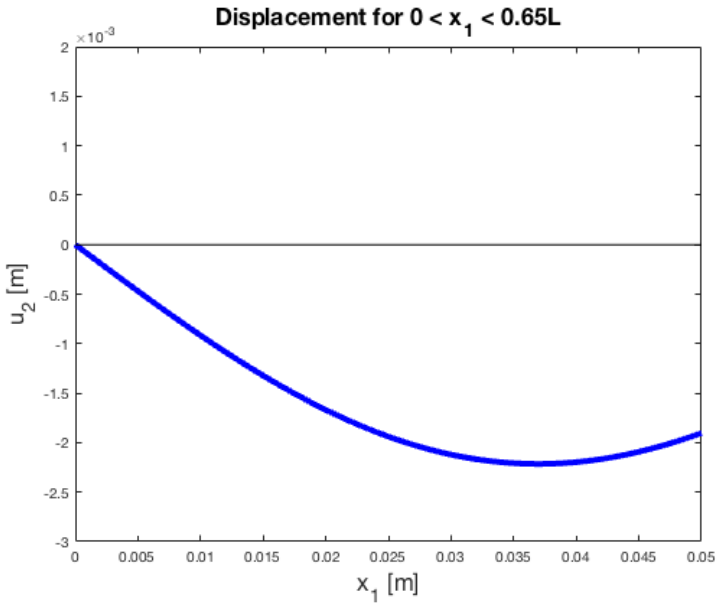

Figure 21. Deflection of region I for the beam-column.

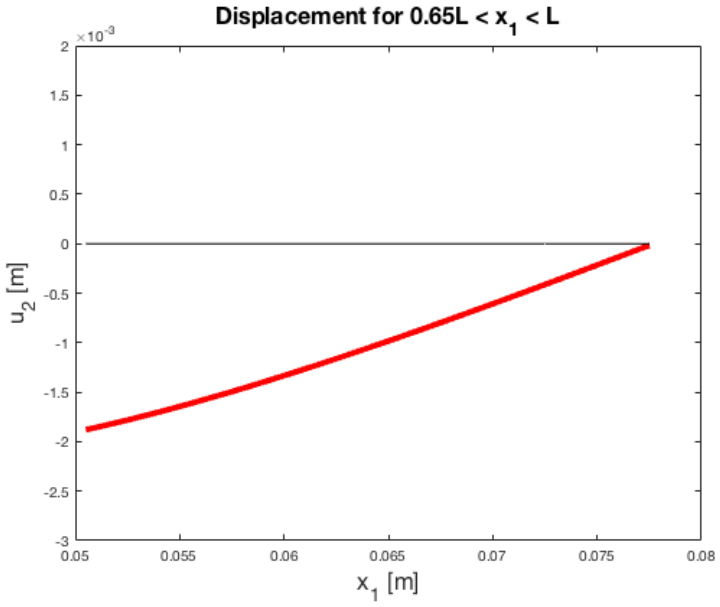

Figure 22. Deflection of region II for the beam-column.

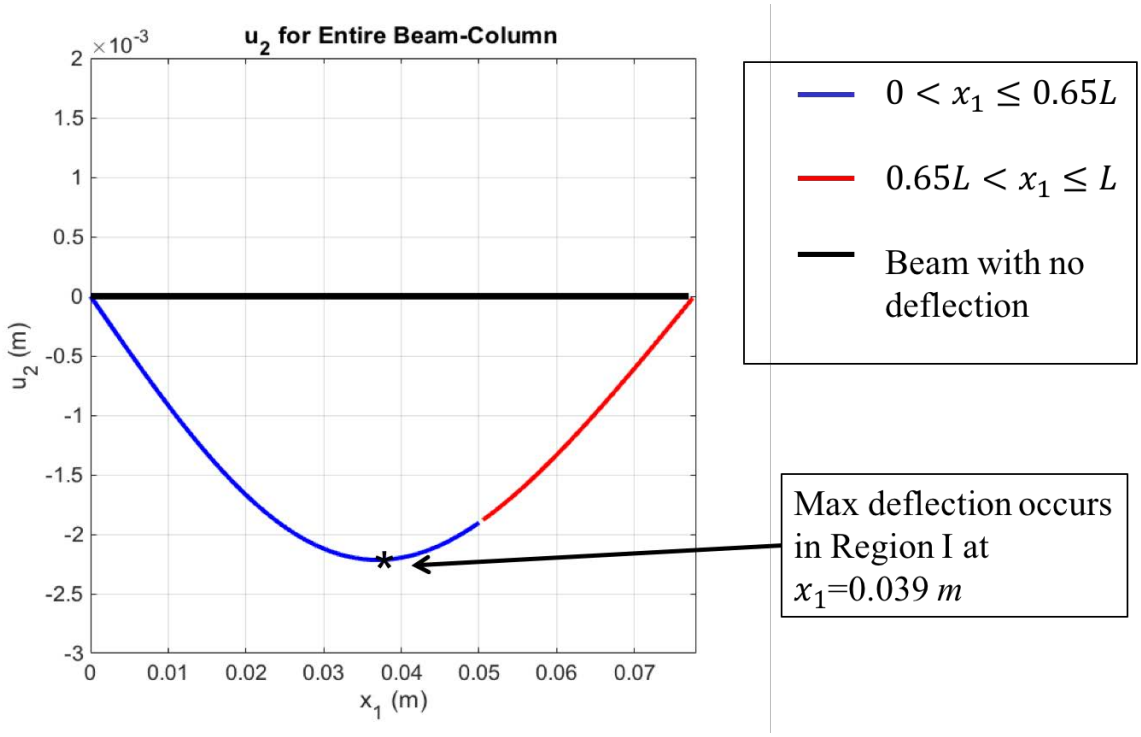

Figure 23. Deflection of the entire beam-column, with point of maximum displacement, compared to the initial position of no displacement.

It is shown that the maximum deflection occurs in region I. The location of the maximum bending moment in region I was found by finding the x_1 location in which the triple derivative of u_{2L} was equal to zero.

$$\frac{\partial^3 u_2}{\partial {x_1}^3} = 0 \tag{46}$$

The result was a location of $x_1 = 39.61mm$. This value was substituted back into the moment equation for the left side of the beam in order to determine M_{max}.

$$M_{max} = \frac{221}{1200} L w_0 x_1 - \frac{10 w_0}{39L} {x_1}^3 + \frac{49 L w_0 x_1}{1200} \tag{47}$$

Equation 47 was found by combining the moment equations found for the left side of the beam for the two separate triangular loading scenarios. M_{max} was found to

be 2.134 $N \cdot m$. The radius of the beam (c) was found by rearranging the following equations.

$$\sigma_y = \frac{Mc}{I} \tag{48}$$

$$I = \frac{\pi c^4}{4} \tag{49}$$

$$c = \sqrt[3]{\frac{4M}{\pi \sigma_y}} \tag{50}$$

Upon rearrangement, c was solved to equal 2.54 mm. This was multiplied by two to get a t for the cross section of 5.08 mm.

2.6 Chapter Summary

The main tenets within this chapter concern: analysis of nonlinear effects, FEA, and sizing using a beam-column analysis. Nonlinearity can be investigated using both experimental and analytical means. An analytical approach to measuring nonlinear behavior is through the use of FEA. An appropriate size for the rings were determined using classical structural analysis techniques paired with the prescribed loading condition of sea-level pressure. This chapter provides a framework for the methodology that is used throughout the research objectives covered in subsequent chapters.

III. Research Methodology

3.1 Chapter Overview

The overall objective of this research is to evaluate the behavior of the celestial icosahedron's structural members. The objective is broken down into a series of successive components. The main components are sizing, AM, experimentation, and FEA. Similar research components have been investigated at AFIT, but none have fully encompassed the stated objective for the celestial icosahedron. However, a review of recent and related works will aid in the setup and analysis of this thesis objective.

The contents of this chapter provides the framework for which the results were obtained. First, the steps of the sizing process that was followed to define the dimensionality of the celestial icosahedron, and its rings, are presented. Next, the AM process and material characteristics are discussed in detail. Finally, the analytical and experimental setups are outlined. The sum of these components provide the methodology that was followed to obtain the results for the research objective.

3.2 Additive Manufacturing

A major objective of this research effort was to implement AM techniques to produce the ring members. AM allows for rapid development of specimens with high accuracy at a relatively low-cost. The 3D printer used for this work was the Stratasys Fortus 450mc (Figure 24). It uses Fused Deposition Modeling (FDM) to produce parts out of "high-performance thermoplastics" to an accuracy of $\pm$ 0.127 mm [30]. This specific printer was chosen because it was accessible and spacious enough to produce the desired specimens. The remainder of the section discusses the material and the FDM process in greater detail.

Figure 24. Stratasys Fortus 450mc FDM printer located at AFIT; the build oven is where the parts were manufactured.

Material Properties.

The material used for producing the parts was ULTEM 9085 Resin. It's availability and compatibility, with the Fortus 450mc, were the foremost drivers for its selection. It is solicited by the manufacturer as a "high-performance thermoplastic with high strength-to-weight ratio," while also "satisfying test criteria required by the aerospace industry" [29]. An initial review proved the material to be a good choice due to its availability, price, compatibility, and performance.

The material's manufacturer, Stratasys, provides open-source documentation on various material properties such as yield strength, ultimate strength, modulus, etc. The reported values were found via ASTM testing standards, but ultimately the user is encouraged to determine if the material is "technically suitable for the intended application" [29]. Additionally, due to the nature of FDM, mechanical properties exhibit anisotropy.

The validity of the results of this research hinged on accurate material properties.

Many facets of the design and analysis would be adversely affected by inexact material definitions. Therefore, an investigation was set forth in an attempt to experimentally determine material properties for the rings that makeup the celestial. The major property of interest was the compressive modulus due to the ultimate objective of compression testing. An accurate modulus is required to characterize the buckling behavior of the rings and the celestial. The investigation of the modulus compared experimental data with FEA results. The goal was to closely match the results to derive a value for the modulus; this process is discussed in the ensuing FEA section.

Print Orientation.

As previously mentioned, the printing method presents anisotropy in the material specifications. FDM is a subset of the material extrusion class within 3D printing [31]. FDM is the process in which a part is built layer by layer atop a build plate. Thermoplastic filament is loaded into the printer, melted, and then deposited as thin strands into layers across the three dimensions of the build space [31]. A build begins at the bottom, or on the surface of the build plate, and is built up layer-by-layer until the entire specimen is completed. An exaggerated illustration of this process is shown in Figure 25.

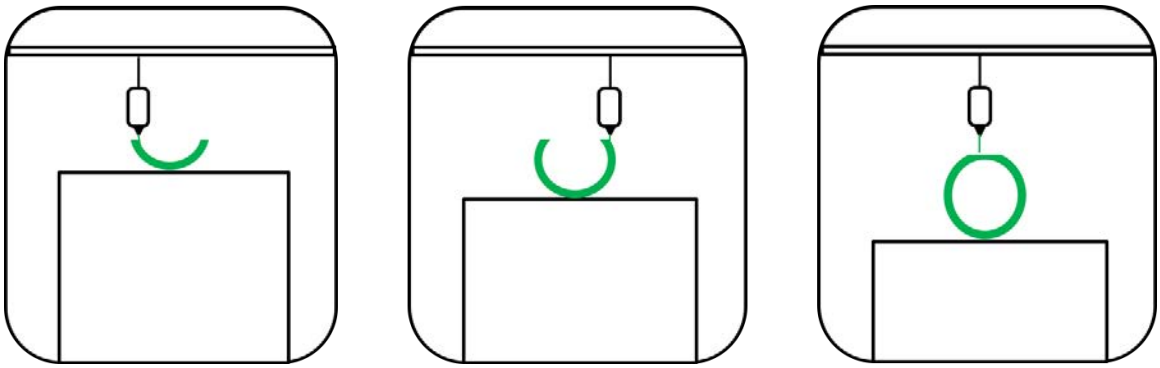

Figure 25. FDM process: layer-by-layer build of a part beginning at the base (left) and progressing to the top of the part (right) [31].

The issue that arises with FDM is the contrast in mechanical properties between

specimens that are printed in different orientations. This introduces variance in the performance of a part that is based on build orientation and the specific material in use. For this work, the manufacturer included different values for material properties based on orientation. However, the difference in these values was substantial. For example, the compressive E in the XZ orientation is over four times the compressive E in the ZX orientation [29]. The reported values are specific to the orientation in which a specimen was printed. Figure 26 shows the orientations that correspond to the published properties.

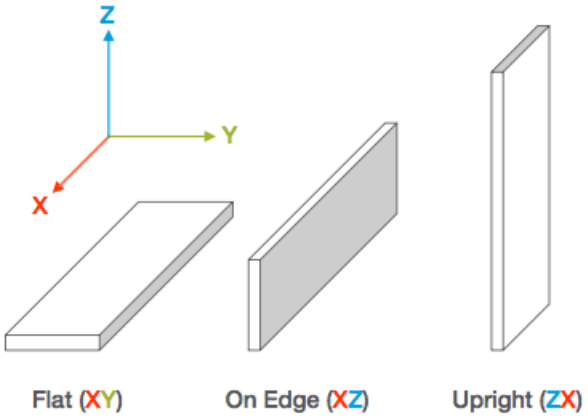

Figure 26. Orientation of test specimen for reported material properties [29].

The celestial icosahedron features three different ring orientations in reference to a horizontal plane: 0°, 45°, and 90°. This difference in orientation can be seen more clearly in Figure 27. The difference in orientation suggests a variation in mechanical properties between the rings. Therefore, an investigation of each particular ring orientation was conducted by printing separate rings at 0°, 45°, and 90°. The behavior of each ring in compression was measured both experimentally and analytically to decipher the compressive E in each direction. This exploration was necessary before the full celestial icosahedron model could be produced in order to gain insight on the model's mechanical properties.

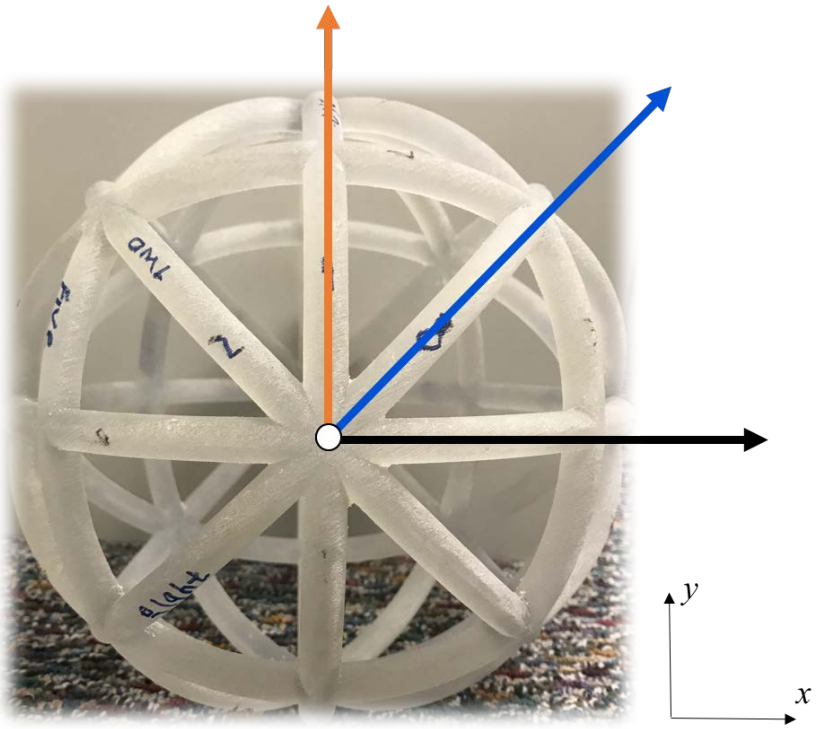

Figure 27. The three different ring orientations that make up the celestial: 0° (black), 45° (blue), 90° (orange).

AM Process.

The same general process was followed to AM each ring using the Fortus 450mc. The only deviations were the support material requirement, build plate configuration, and post-processing. Stratasys Fortus Insight software was the program used to pre-process the rings; this included parameters such as build direction, support material, and batch size. The following process highlights the main tenets of the manufacturing process from design to part production:

1. Generation of computer-aided design (CAD) model, using SolidWorks, with appropriate sizing and geometry for the ring (Figure 28).

2. Importation of stereolithography (STL)-file, for the CAD model of the ring, into Stratasys Fortus Insight software (Figure 29).

3. Application of support material conditions for the part based on print orientation (Figure 30).

4. Configuration of batch size, which was contingent on the build plate size, so the maximum number of parts per build could be safely satisfied (Figure 31).

5. Transmission of pre-processing specifications to Fortus 450mc for part production.

6. Removal of support material from the finished part(s).

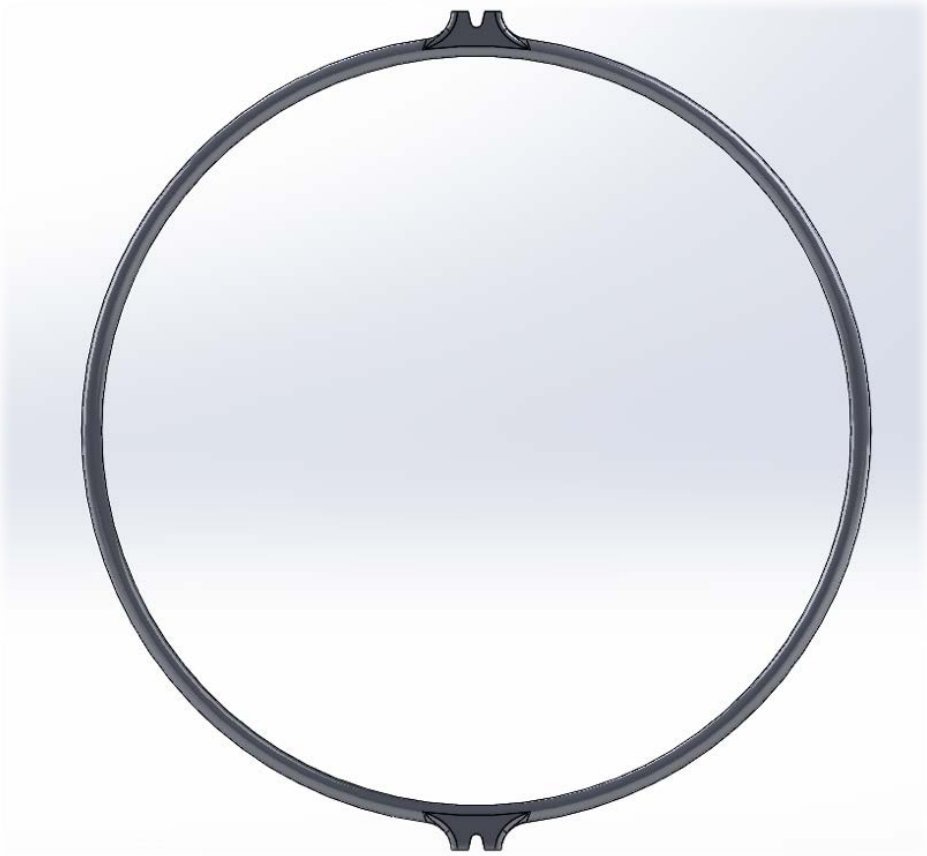

Figure 28. CAD model of the ring generated within SolidWorks and sized according to the results from the beam-column analysis.

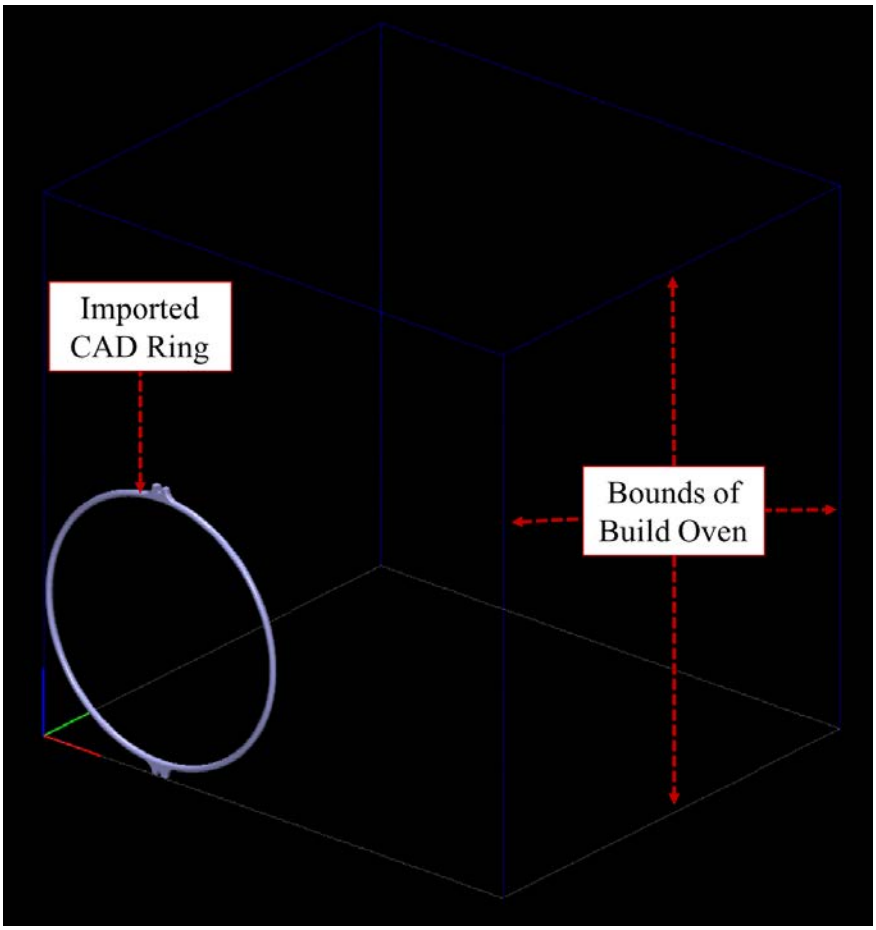

Figure 29. CAD model of a 90° ring placed within Insight software; the blue bounds represent the geometry of the build oven within the Fortus 450mc.

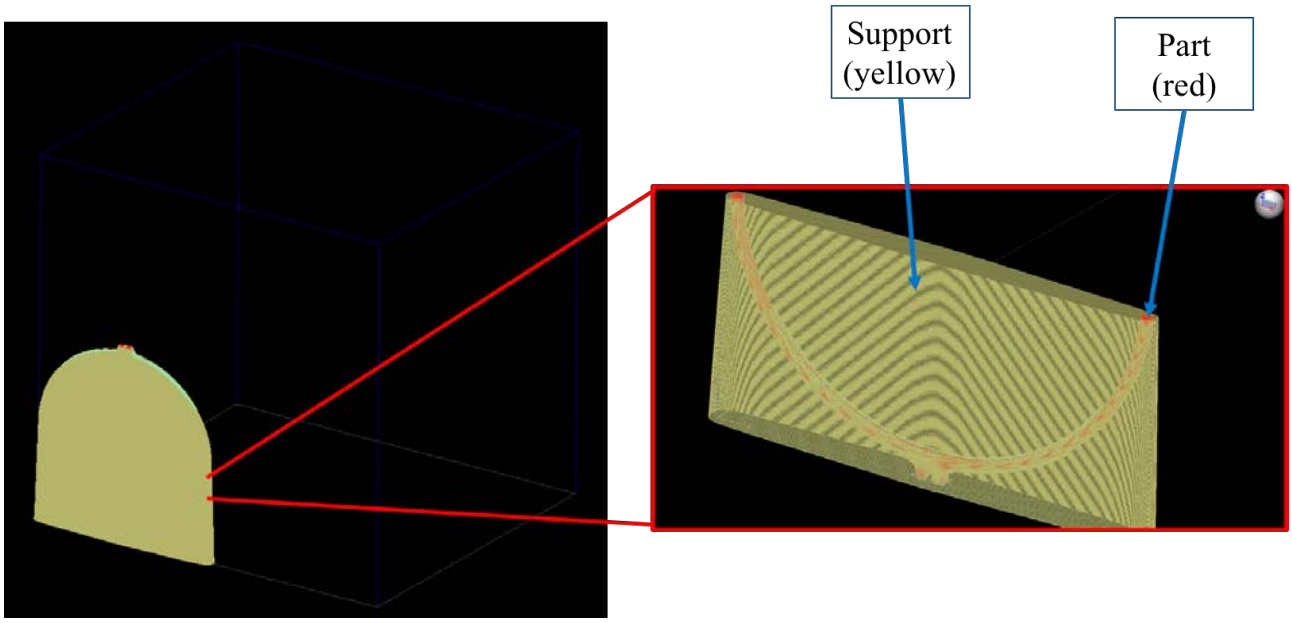

Figure 30. Application of support material within the Insight software for a 90° ring, in which the entire ring was encased in support material to aid in it's support throughout the build process.

Figure 31. Interface on Insight software that allows for part placement on the build plate to determine batch size; this particular configuration is a stack of four 90° rings (labeled "1-4").

3.3 AM Results

The rings were printed in separate batches according to their respective orientation. The parameters of each batch varied depending on the type of ring being printed. Notable parameters that were measured were: batch size, print time, material requirements, and post-processing effort. The size of the batch was determinant on the build plate's capacity to successfully hold each specimen. The time required for each batch was specific to the orientation along with the amount of support material and post-processing required.

The most straightforward print was the 0°-oriented ring. It required a marginal amount of support material because an entire side of the part rested on the surface of

the build plate and served as the base for the print. Since support was not required, there was no post-processing involved. The ring's front profile is much wider than it's side profile due to it's 0.2032 m diameter and 5.08 mm thickness. The 0° print required the front profile of the ring to be laid across the length and width of the build plate. The build plate area was 406 x 356 mm [30]. Therefore, the batch size for the 0° prints were limited to two rings. The 0° ring was the quickest to print with a total print time of 2 hrs. A manufactured 0° ring is shown in Figure 32.

Figure 32. The finished print of a 0° ring.

A closer look at the ring's surface provides a clearer distinction on the build composition. The following image was taken of the inner section of a 0° ring using a stereo microscope at 13.8x magnification.

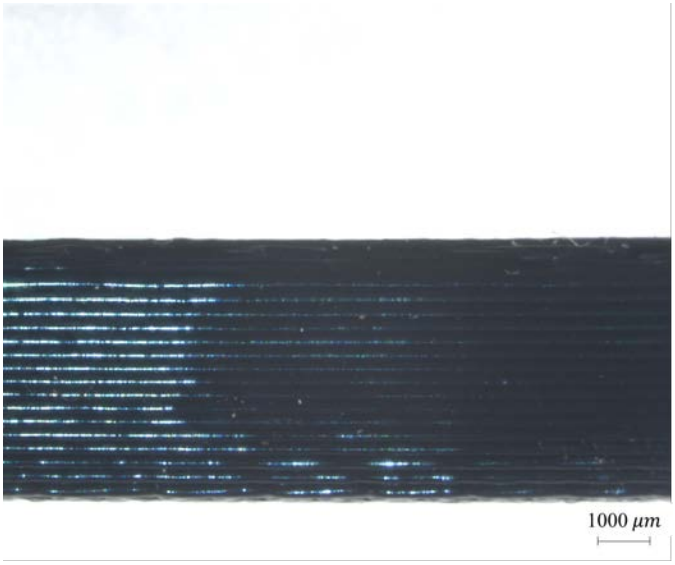

Figure 33. The inner surface of a ring printed in the 0°-orientation, in which the layers of material are demarcated by the horizontal striations across the length of the section.

The 45°-oriented ring required a lot of support material to craft it's unique support structure. This was necessary in order to successfully print the cross-section of the ring at a 45° angle. The print time for the 45° prints was 26.5 hrs. Figure 34 shows the finished build of a batch of 45° rings within the build oven. Figure 35 shows a batch of 45° rings with the support material attached.

Figure 34. A batch of 45° prints sitting atop the build plate within the build oven of the Fortus.

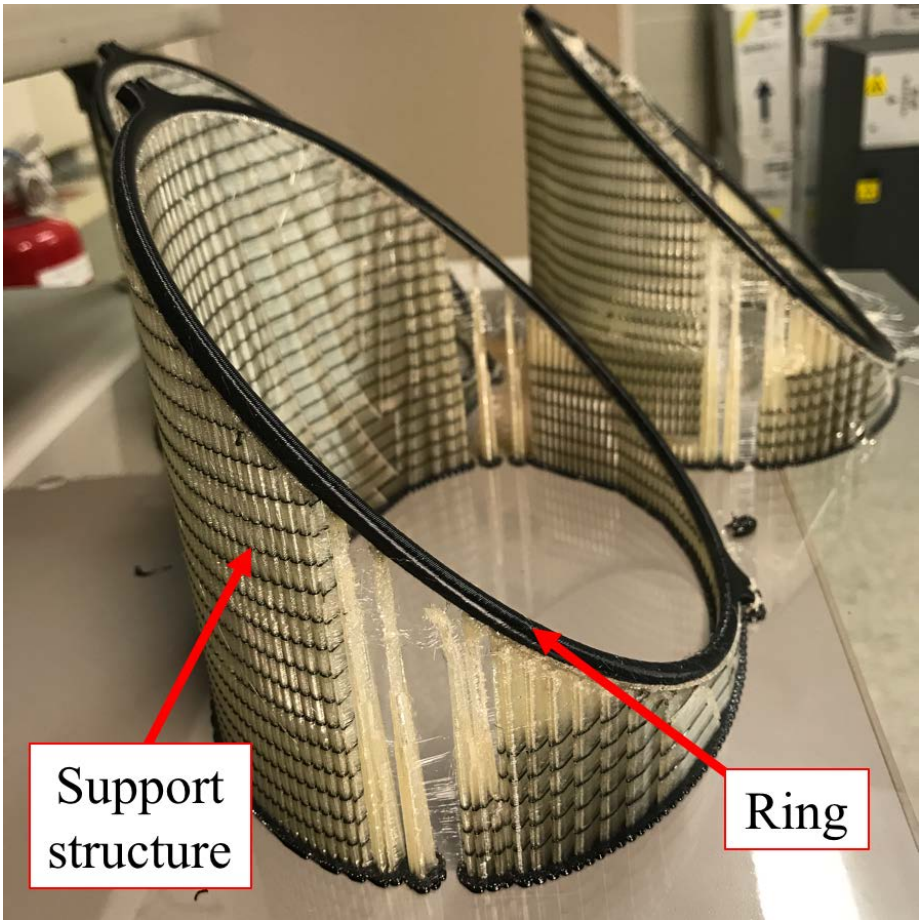

Figure 35. The side profile of a batch of 45° prints sitting atop their support structures.

As shown in Figure 35, the batch size consisted of three rings. The top profile of the print is pictured in Figure 36.

Figure 36. The top profile of a 45° print with its support structure intact.

Figure 37 provides a closer view of the 45° build composition. It was also taken of the inner section of a 45° ring using a stereo microscope at 13.8x magnification. The 90°-oriented rings were printed in batch sizes that consisted of four rings. The thin side profile of the ring allowed for the prints to be stacked closely together. They were printed in two different trials. The first trial adhered support material to the majority of each ring as shown in Figures 38 & 39.

Figure 37. The inner surface of a ring printed in the 45°-orientation, in which the layers of material are depicted by the left-slanted striations across the length of the section.

Figure 38. The front profile of a 90° print from the first trial.

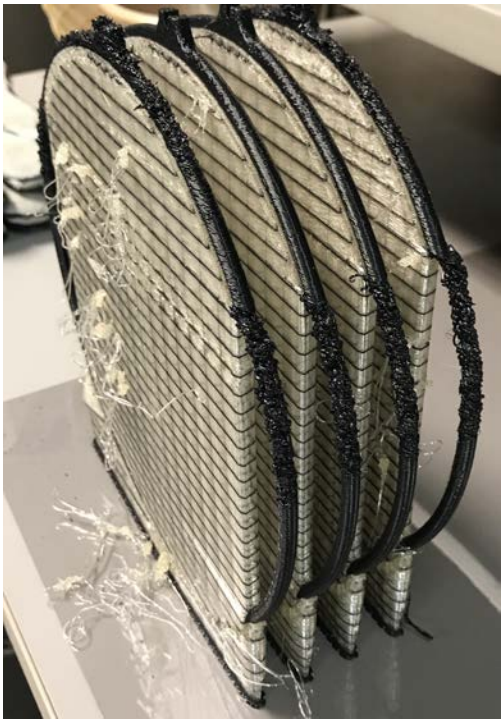

Figure 39. The side profile of a 90° print from the first trial.

An inspection of the build quality reveals apparent discontinuity and deformation in the upper quadrants of the build. The print was not able to support itself as the material was deposited in these regions. A second trial was run in which the support material fully enclosed the rings. The encasement can be seen specifically in Figure 40.

Figure 40. Top view of the fully encased batch of 90° prints from the second trial.

The product of the second trial was a smooth build throughout all regions of the ring. Extensive post-processing was necessary to remove the rings from the support material. Additionally, a 45° print was added to the build in order to take full advantage of the build plate area. Hence, the second trial consisted of four 90° rings and one 45° ring. It was the longest build resulting in 33 hrs of print time. The entire build is depicted in Figure 42. Figure 41 is an image of the inner section of a 90° ring using a stereo microscope at 13.8x magnification.

Figure 41. The inner surface of a ring printed in the 90°-orientation, in which the layers of material are depicted by the vertical striations across the length of the section.

Figure 42. The entire build for the second trial: four 90° prints and one 45° print.

The chief characteristic for each build was the orientation in which the material was deposited layer-by-layer. The finished builds were identical in both shape and size. A summary of the different prints and their specifications are presented in Table 1.

Summary of Print Specifications			
Orientation	Batch Size	Support Material (cm^3)	Print Time (hrs)
0°	2	21	2
45°	3	445	26.5
90°	4	256	18.5

Table 1. Summary of build parameters for each ring orientation.

3.4 Experimental Setup

The chief tenet of this research was measuring the response of the celestial icosahedron, and its individual rings, in compression. In order to gain this response, the

celestial and rings were physically tested in an MTS machine. A unique experimental setup was required to accommodate the geometry of both the celestial and rings. The aim was to closely replicate the experiment conducted by Cranston et al., in which a 3D printed icosahedron frame was tested in compression [17]. However, the difference in geometry between the two designs required a different approach for experimentation. As shown in Figure 43, the icosahedron had a flat surface both at the top and bottom of its frame, which enabled the part to be placed between two platens that were affixed to the MTS loading cell. The celestial is composed of circular rings

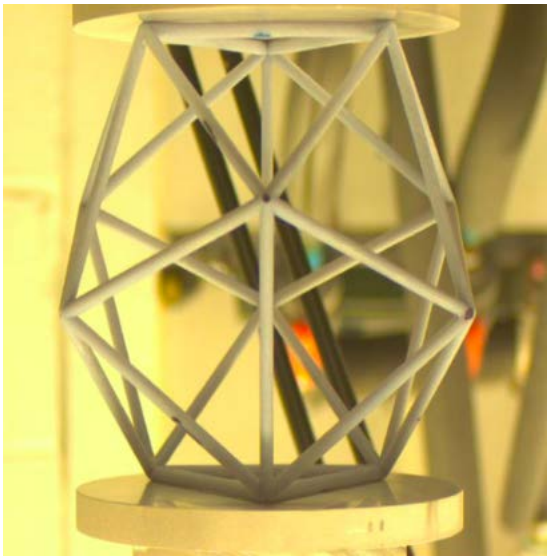

Figure 43. The icosahedron affixed between two platens in an MTS testing machine [32].

and does not have flat surfaces in which it can be conveniently placed between two plates. Therefore, a different approach was taken to secure the individual rings and the celestial frame within the MTS.

MTS Acumen.

The machine used for the compression tests was an MTS Acumen 3 Electrodynamic Test System located at AFIT. This machine employed a 661.11H-01 model load

cell from MTS. The most recent calibration for this machine listed it's full scale (FS) capability at 250 N. The specific MTS Acumen used for experimentation is shown in Figure 44.

Figure 44. MTS Acumen 3 testing rig–located at AFIT and equipped with a 250 N load cell.

MTS 858 Landmark.

The testing machine that was used for the majority of the analyses was an MTS 858 Landmark Tabletop Test System located at AFIT. This particular machine employed a 661.19H-04 model load cell from MTS. The calibration for this machine listed it's FS capability at 25 kN. The particular load cell is rated to measure compression loads ranging from 5-25 kN [33].

It was presumed the magnitude of compression force on the ring would not enter within this range. The calibration for the load cell was performed incrementally according to percentage of FS force. The lowest calibration point was performed at

2% FS, which equated to 0.5 kN. The force at this calibration point still exceeded the maximum expected compression force in which the ring would undergo. Therefore, it was necessary to verify the data acquired from this machine was accurate. Verification was conducted with the MTS Acumen testing rig. It's 250 N load cell was more conducive to the expected range of forces.

Compression of Rings.

Great caution was taken in order to accurately test a ring in compression. A large portion of effort revolved on the experimental setup. A mechanism was required to be built into the ring's geometry so that the ring could be held in proper alignment between the MTS heads. A model of the ring was generated in SolidWorks, in which additional tab-like features were modeled on the top and bottom vertex of the ring.

This tab feature shared the same width of the ring's t and had a radius built in the center of the flange. It was designed as an additional extrusion to the outer surface of the ring so that it would not compromise the geometry of the ring. The radius was added so that an external piece could nest within it and allow the ring to be secured within the MTS. A render of the ring model, with the built-in tabs, is depicted in Figure 45. The actual tab that was printed on the model is shown in Figure 46.

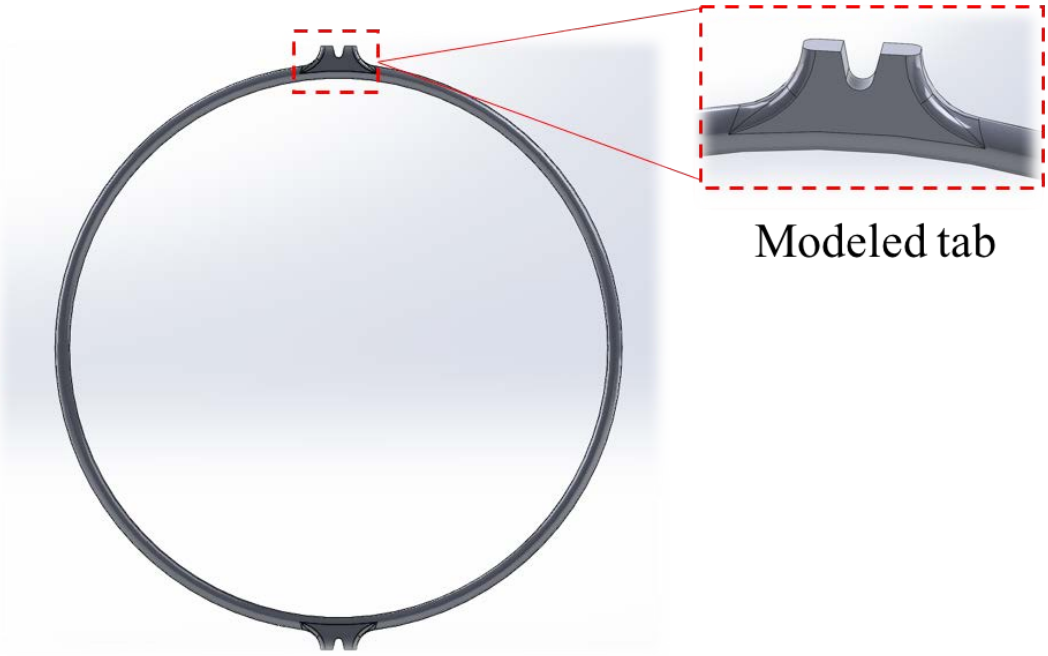

Figure 45. The SolidWorks model of the ring with a closer section view of the tab feature that was built into the top and bottom of the ring.

Figure 46. The built-in tab feature for the top and bottom of the ring.

The additional feature that was added to the ring was accompanied by an external piece that fit within the MTS. The conceptual design was generated in SolidWorks, but the actual piece was modified so that it could be easily manufactured. A side-by-side comparison of the conceptual model and the finished product for the clamp

is provided in Figure 47. The clamp's shape and size was crafted specifically for use in the 22.2 kN MTS shown in Figure 50.

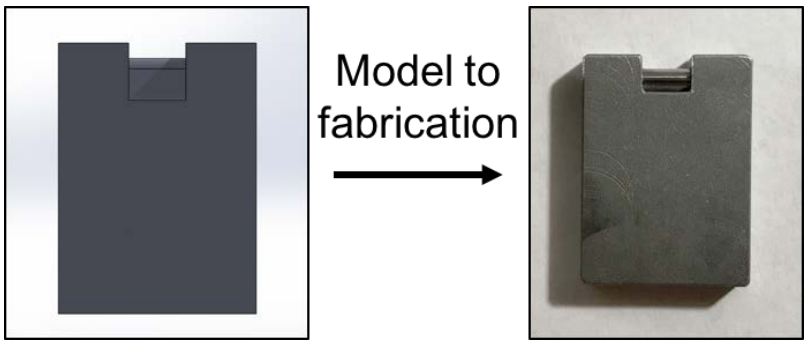

Figure 47. Comparison of the external clamp that was designed in SolidWorks (left) and manufactured (right) to sit within the MTS grips to hold the ring.

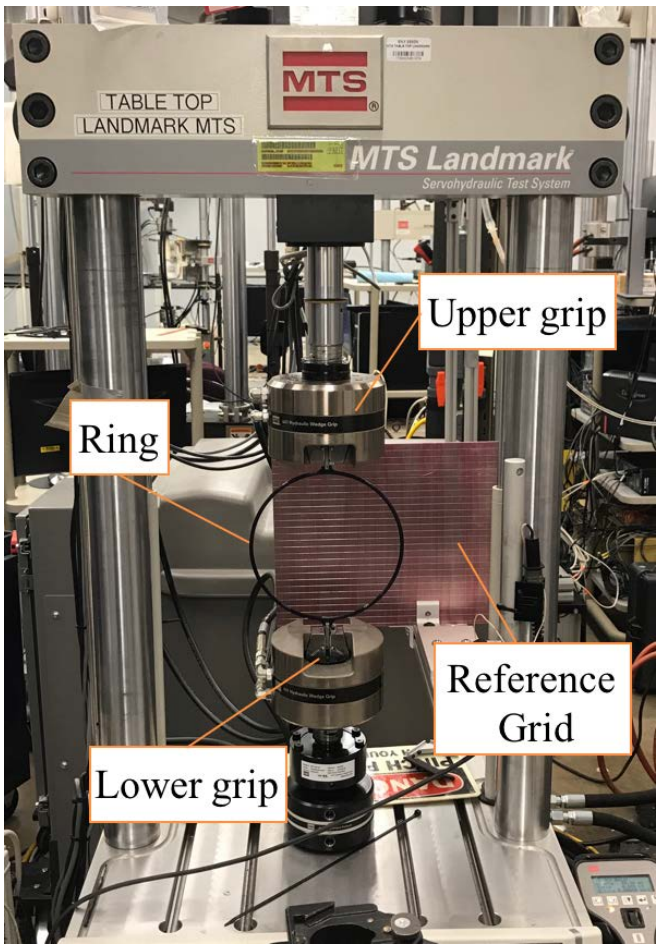

Figure 49. Experimental setup with a ring secured within the MTS 858 Landmark–25 kN MTS.

(a)

(b)

Figure 48. The clamp piece that was manufactured to hold the upper and lower portions of the ring in place within the MTS.

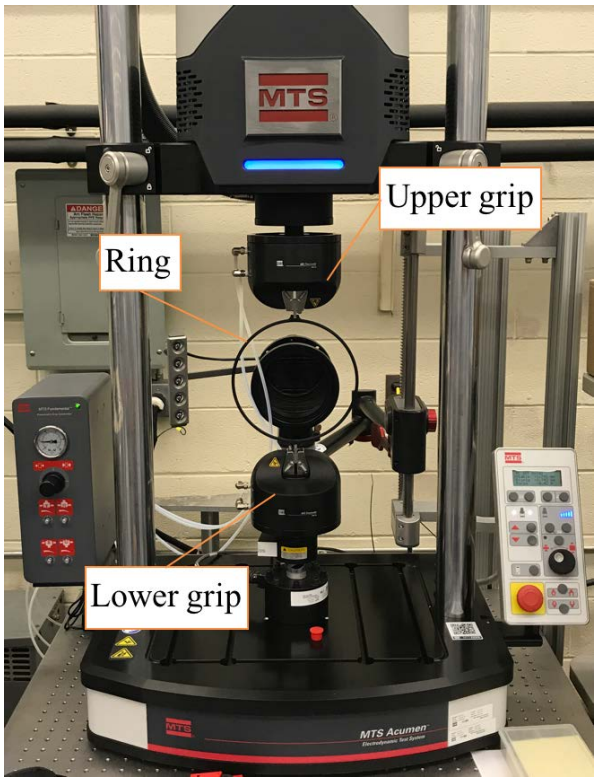

Figure 50. Experimental setup with a ring secured within the MTS Acumen 3–250 N MTS.

The additional design features were included to ensure the ring would be aligned correctly within the test space. The design aimed to provide appropriate boundary conditions to mitigate the movement of the ring during testing. The ideal loading condition was to be purely in the downward vertical direction and any rotation or translation of the ring would incite eccentric loading. The tab and clamp approach provided support, at the connection points of the ring and the MTS, to inhibit translation in any direction. Representation of a ring properly placed within the MTS 858 Landmark is provided in Figures 51, 52, 53. The setup for the MTS Acumen 3 is provided in Figures 54, 55, 56.

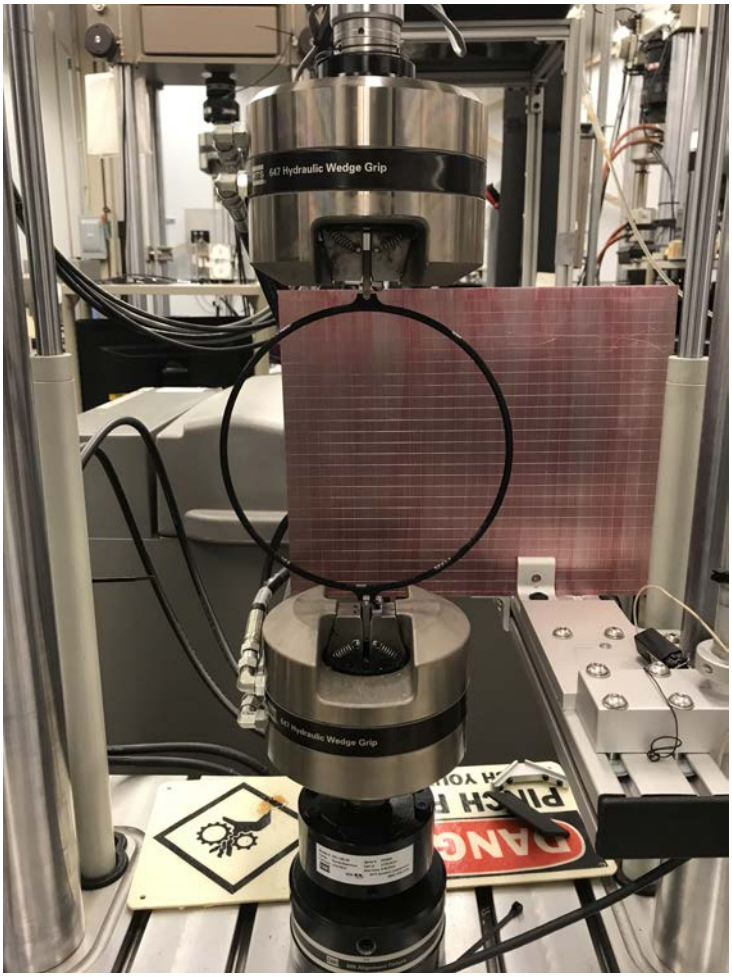

Figure 51. Ring secured within the MTS testing rig.

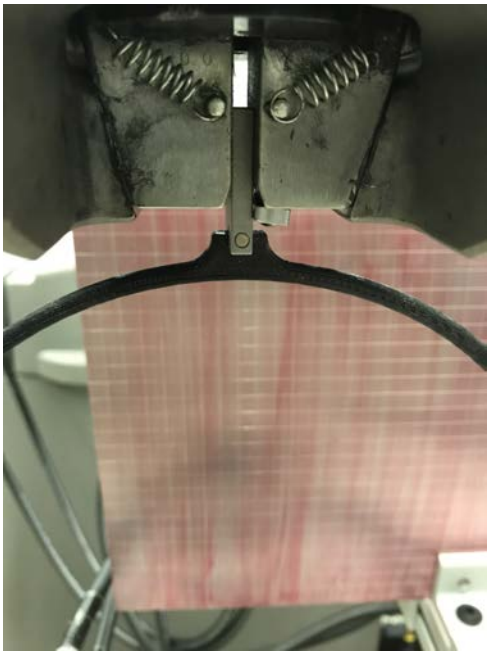

Figure 52. View of the top of the secured ring.

Figure 53. View of the bottom of the secured ring.

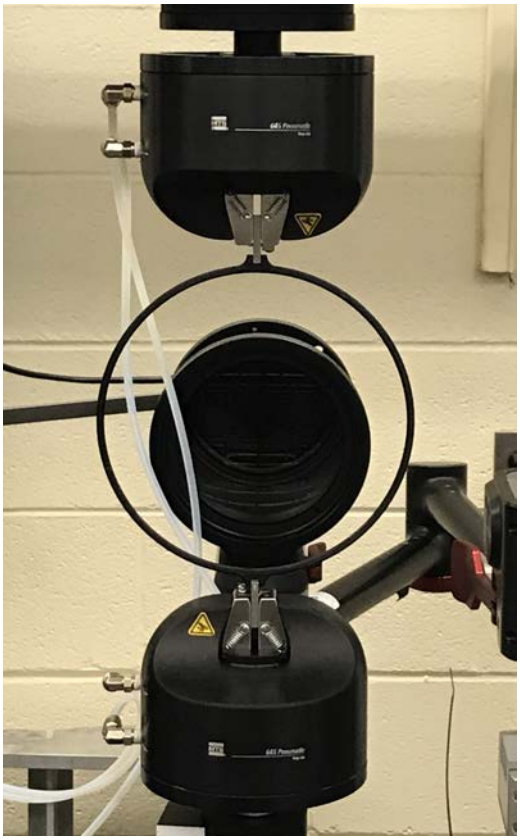

Figure 54. Ring secured within the Acumen 3 testing rig.

Figure 55. Views of the top clamp in the Acumen 3.

Figure 56. Views of the bottom clamp in the Acumen 3.

The rings were placed under compression loading. The loading was unidirectional in the negative y-direction. It was quasi-static with a loading rate of 1.27 $\frac{mm}{min}$, in accordance with ASTM D95-15 [34]. The first loading condition was based on a prescribed vertical displacement of the upper loading cell, which was equal to 50.8 mm. The lower cell was fixed in place. The setup is shown in Figure 57. The MTS data acquisition software was used to record the force (P), displacement (δ), and time. Data was acquired at a rate of 5 Hz.

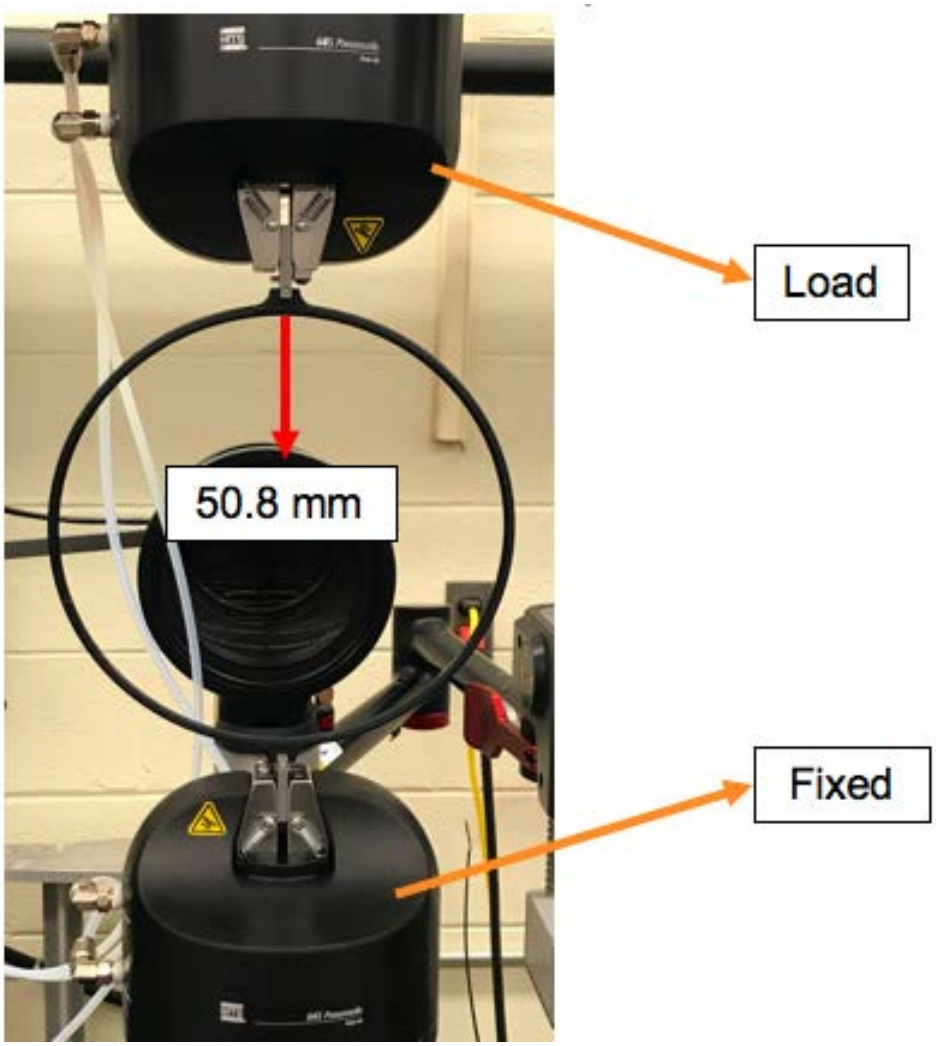

Figure 57. Compression test setup in MTS displaying the displacement condition and the upper and lower boundary conditions of the secured ring.

3.5 Finite Element Model

FEA was a significant analytical tool throughout this thesis work. It provided a means to simulate the experimental methodology to investigate material properties and stability behavior. A credible finite element model was required to accurately represent the ring. The model was designed to be simple and robust so that copious simulations could be run without requiring excess computational load or time. The model was setup using Abaqus/CAE 2016.

Ring Models.

Two FEA models were constructed for the specific analysis of a ring under compression. Both were modeled as a 3D, deformable beam structure within Abaqus. The general shape was created by defining a circle with a vertex at (0,0,0) and an overall diameter of 0.2032 m. The model was assigned B32 elements, which are quadratic beam elements in space (3D) [20]. Within Abaqus, B32 elements are Timoshenko beams meaning they are shear flexible [20]. More information in regards to element type, nodes, and solving can be found in Chapter 2.

The first model had the exact profile of a ring and was assigned a solid, circular cross-section throughout. The ring was assigned an approximate global seed size of 1 mm to produce a mesh with 622 elements and 1,866 nodes. The boundary condition for the bottom of the ring was set to inhibit any movement. A displacement equal to 50.8 mm in the negative y-direction was set as the boundary condition for the top of the ring. The point of application for the displacement was at the nodal location of (0,0.1016,0) m. The boundary conditions and model are displayed in Figure 58.

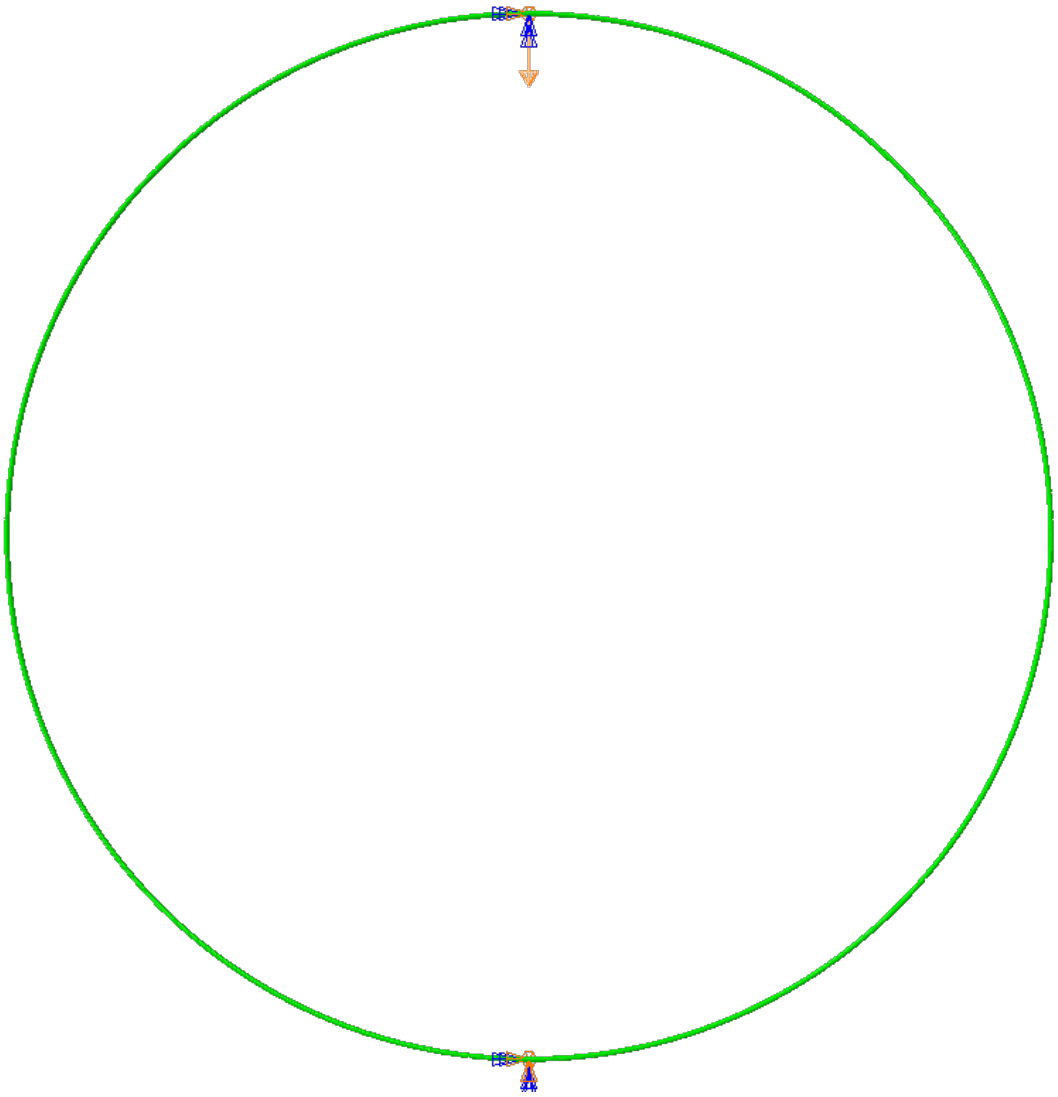

Figure 58. The boundary conditions set for the top and bottom of the FEA model.

Figure shows a closer look at the top boundary condition, in which five DOF were constrained–including rotation in about each axis and two translational directions. The only movement allowed was in the vertical, or '2' direction.

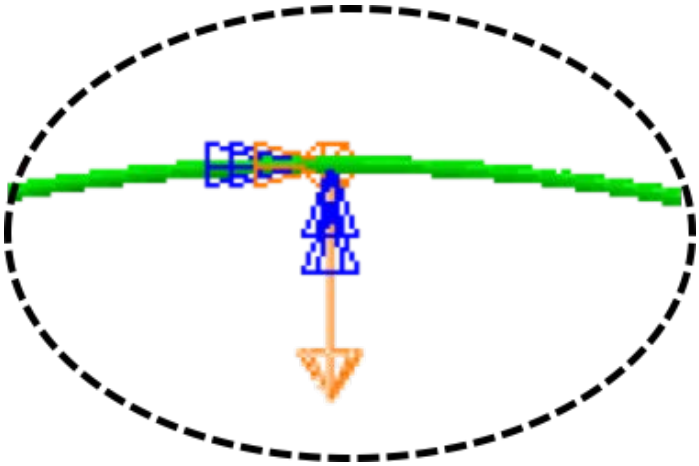

Figure 59. The boundary conditions set for the top of the model.

The boundary condition for the bottom of the ring was clamped–barring any rotational or translational movement. This condition was set in order to mimic the experimental boundary condition. A closer view is shown in Figure 60.

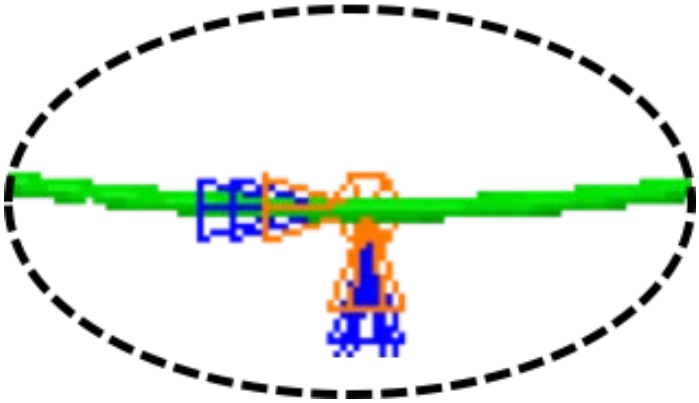

Figure 60. The boundary conditions set for the bottom of the model.

Nonlinear Abaqus/Standard was used as the solving routine. The step type used was static, general. The time period was set to 10 s. The incrementation parameters are provided in Figure 61.

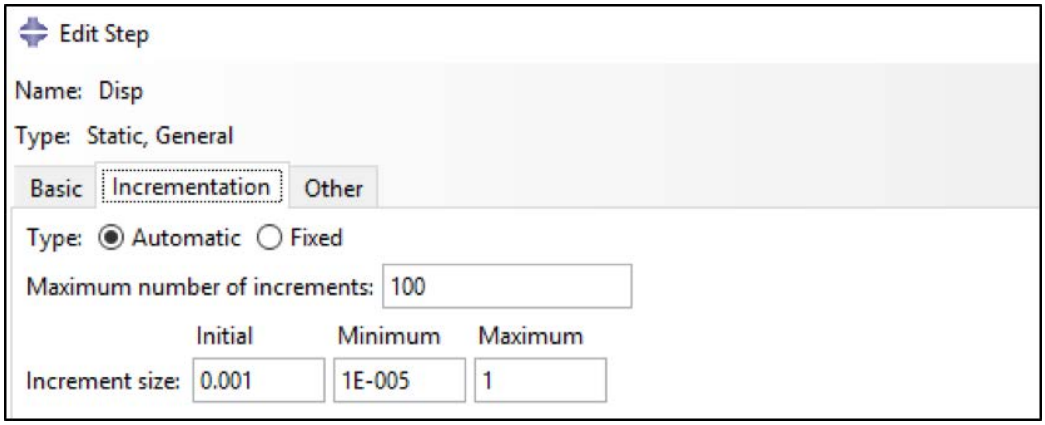

Figure 61. The settings used for incrementation within the step module.

The second model was similar in shape to the exact ring model except for a nonuniform cross-sectional thickness. The cross-section was circular throughout the model but had a different thickness at the top and bottom of the ring. This change in thickness was employed to better emulate the 3D printed ring. The actual print featured a built-in tab at the top and bottom of the ring as shown in the previous section.

The thickened sections were assigned a diameter of 9.1 mm and spanned the same length as the built-in tab. This increased diameter corresponds to the overall height of the built-in tab. The remainder of the model was assigned a diameter, or thickness, of 5.08 mm. The same mesh characteristics and boundary conditions as the exact ring model were applied. This tabbed model allows for the model to remain a beam structure but also account for the increase in material in the upper and lower vertices of the ring. Figure 62 shows the tabbed ring and Figure 63 provides a closer view of a thickened section.

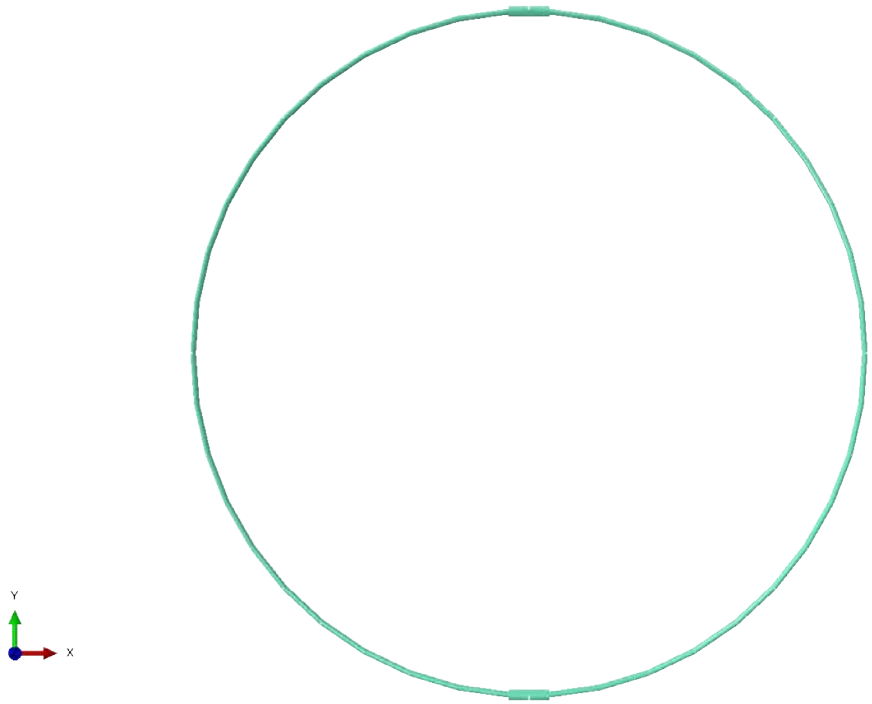

Figure 62. The tabbed ring model used to emulate the thickened sections of the printed ring.

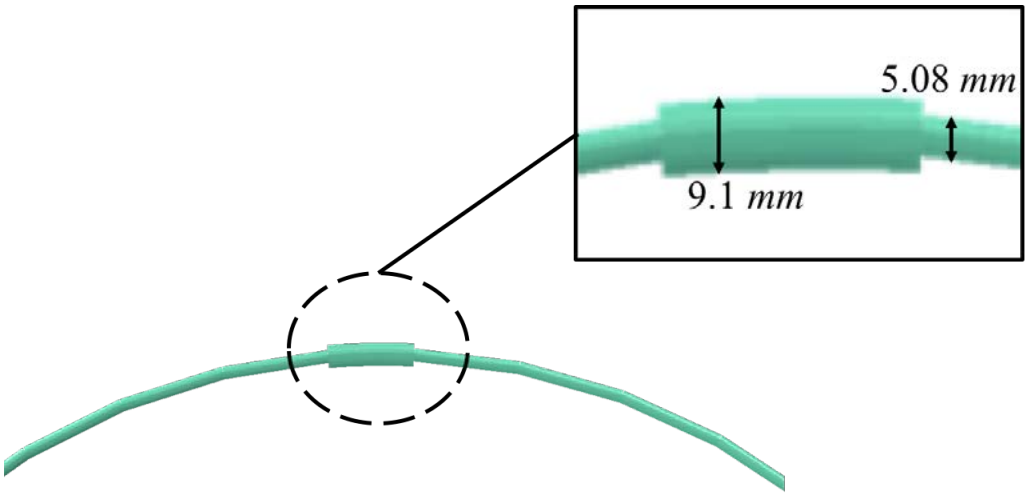

Figure 63. A close-up view of the thickened section of the tabbed ring model, in which the cross-section changes from 5.08 mm to 9.1 mm.

Arch Model.

The celestial icosahedron has various intersection points throughout the structure. These intersection points are specific regions in which multiple members conjoin. There are three different types of intersections that are based on the number of ring members. The first type is an intersection of two rings. The second type is an intersection of three rings and the fourth type is an intersection of four rings. All three of these intersections within the celestial can be viewed in Figure 64.

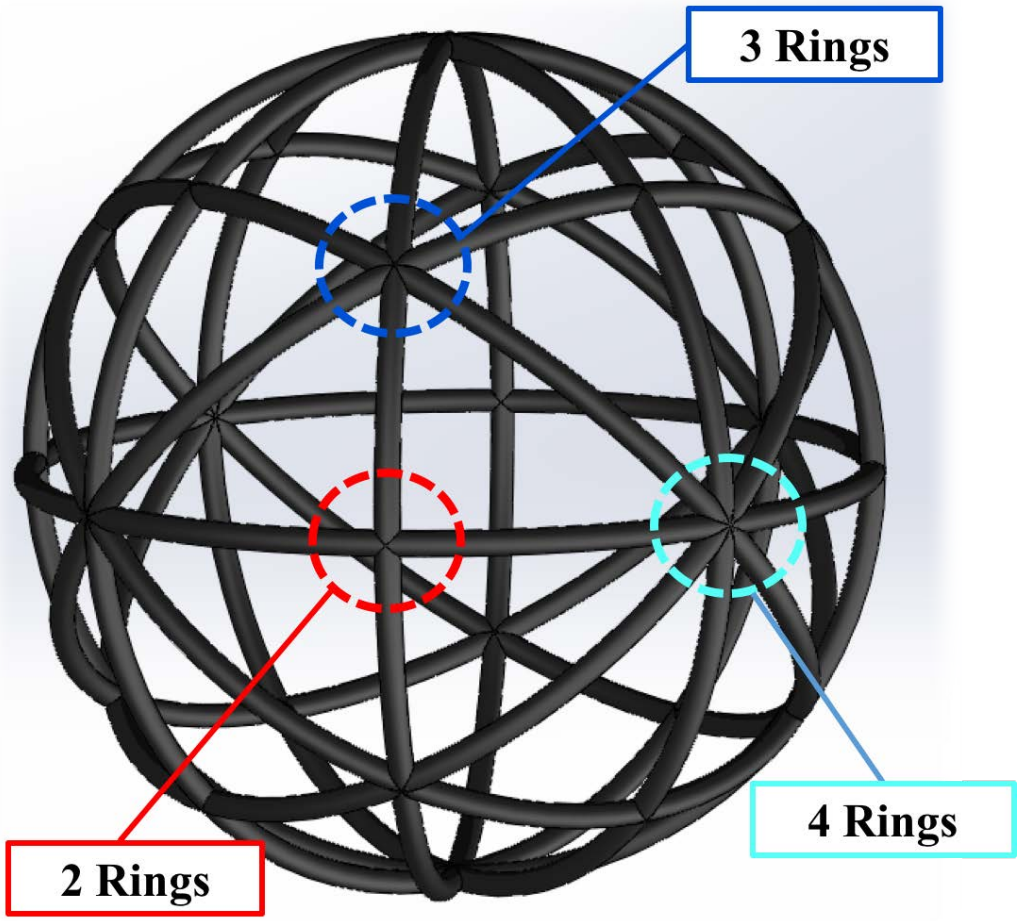

Figure 64. The three different types of intersections within the celestial icosahedron: 2-ring, 3-ring, and 4-ring.

The ring members are stiffened at the regions of intersection. The amount of added stiffness depends on the type of intersection. The 4-ring intersection supplies

greater additional stiffness and support than the 2-ring and 3-ring type. The 4-ring intersection was of interest in this analysis. A celestial icosahedron, manufactured using FDM, would include 90°-oriented ring members that feature two 4-ring intersections. This juncture occurs when a 90°-oriented ring meets with the 0°-oriented ring. This particular region is highlighted by the turquoise circle in Figure 64.

An FEA model was generated of an arch in order to replicate the upper half of a 90°-oriented ring with two 4-ring intersection points. The intersection points are modeled as fixed boundary conditions, in which all translation and rotation at the ends of the arch is inhibited. The arch was subjected to the same displacement condition as the ring models: 50.8 mm in the negative y-direction at the top vertex. All parameters for the mesh were kept the same using B32 elements. The step information and solving routine were identical to the ring model analysis. Figure 65 shows the arch model with the appropriate boundary conditions at the ends and the displacement condition at the vertex.

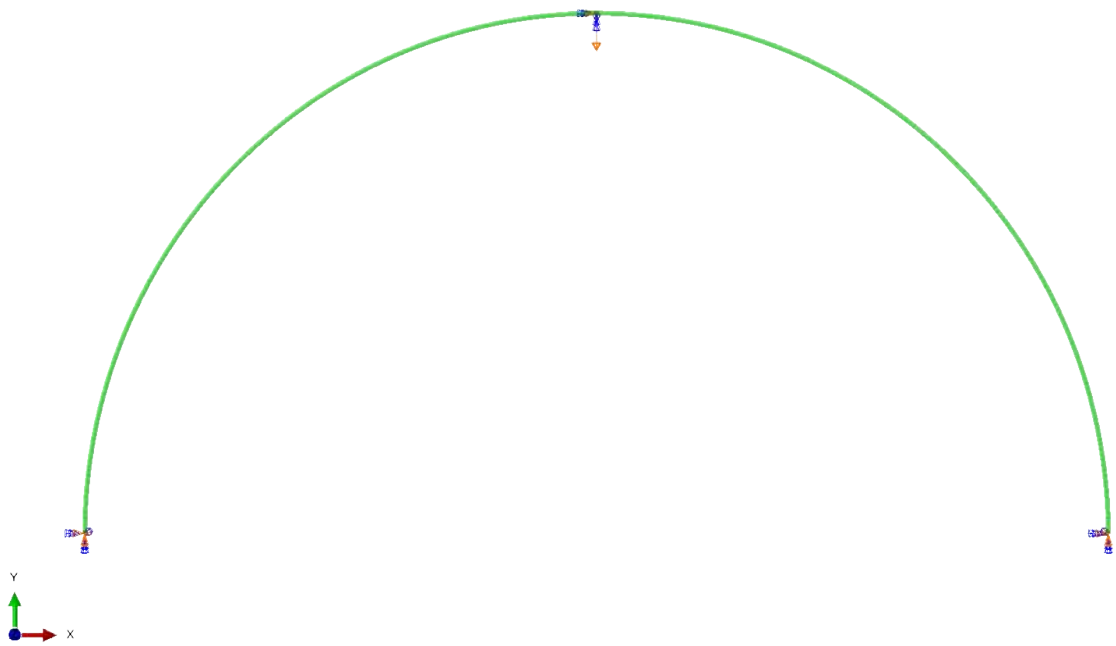

Figure 65. The setup for the arch model featuring fixed ends and a prescribed -50.8 mm vertical displacement at the top vertex.

3.6 Chapter Summary

The aim of this thesis is to examine the behavior of the celestial icosahedron's ring members. Within the celestial, the rings are oriented in three different directions: 0°, 45°, and 90°. Rings were manufactured for each orientation using FDM–a robust AM technique. The rings' stiffness was measured by placing them under compression. Due to their curved profile, a unique experimental setup was crafted in order to place the rings in compression using a 25 kN MTS machine. Simultaneously, two ring models and an arch were created and analyzed using Abaqus/CAE FEA software. The results from the different objectives are presented in the following chapter.

IV. Results

4.1 Chapter Overview

There are multiple objectives included within the scope of this research. Each objective is unique, but also tied to one another so that the overall objective of the research can be accomplished. The overall objective is to examine the nonlinear response of the celestial's ring members subjected to uniaxial compression. This required varied efforts such as AM, experimentation, and FEA in order to come to fruition. Throughout this chapter, the results of each effort are discussed. The following components will be presented:

- The experimental results from placing each ring orientation under compression using an MTS testing machine.
- The investigation of material properties using the experimental and analytical results in conjunction.
- The analytical results from FEA, which provide specific output from the simulation that can be directly compared to the experimental results.

4.2 Compression Testing

The rings were tested in accordance with the parameters outlined in Chapter 3. The results for each ring, based on orientation, will be presented subsequently. The test data provided from the MTS machine was processed and filtered using MATLAB.

Three samples of the 0°-orientation were tested in the MTS Landmark and MTS Acumen. The prescribed loading rate was 1.27 $\frac{mm}{min}$. The loading condition was set to a -50.8 mm vertical displacement of the upper hydraulic grip. The raw data of the P vs δ curve for the first sample, is presented alongside the filtered data in Figure 66

to display the effect of the filtering algorithm that was used for the remainder of the results.

The filtering algorithm was a built-in function in MATLAB. It employed the Savitzky-Golay filtering method. This method "smooths out the noise in data by minimizing the least-squares error in fitting a polynomial to frames of noisy data" [35].

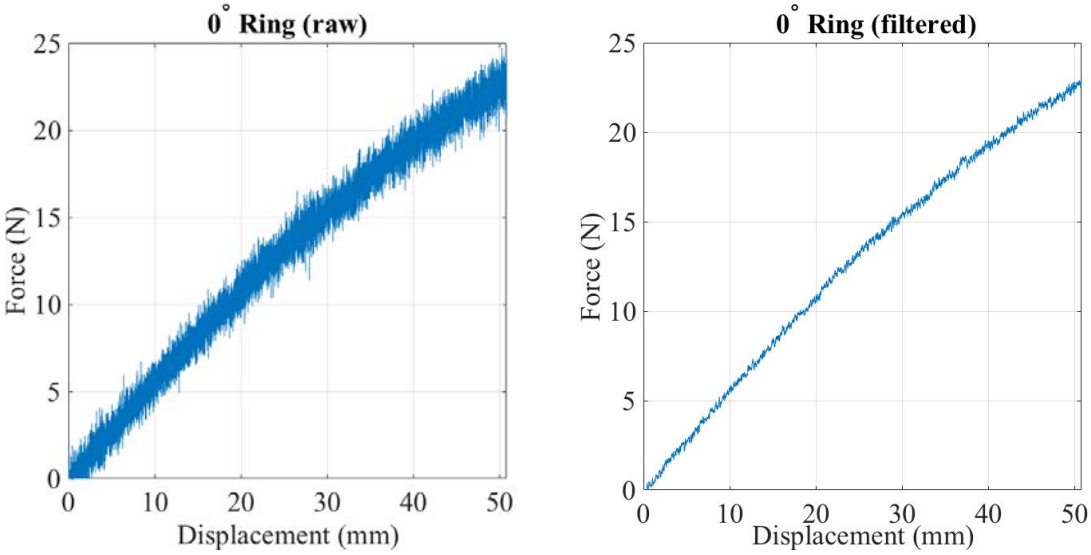

Figure 66. Experimental results for the 0°-oriented ring comparing raw (left) vs filtered (right) data.

MTS Acumen Results.

The following results are from the prescribed loading conditions for the compression testing described in Chapter 3. One ring for each orientation was tested using the MTS Acumen 3 testing rig. The results for the 0° ring are presented in Figures 67 and 68.

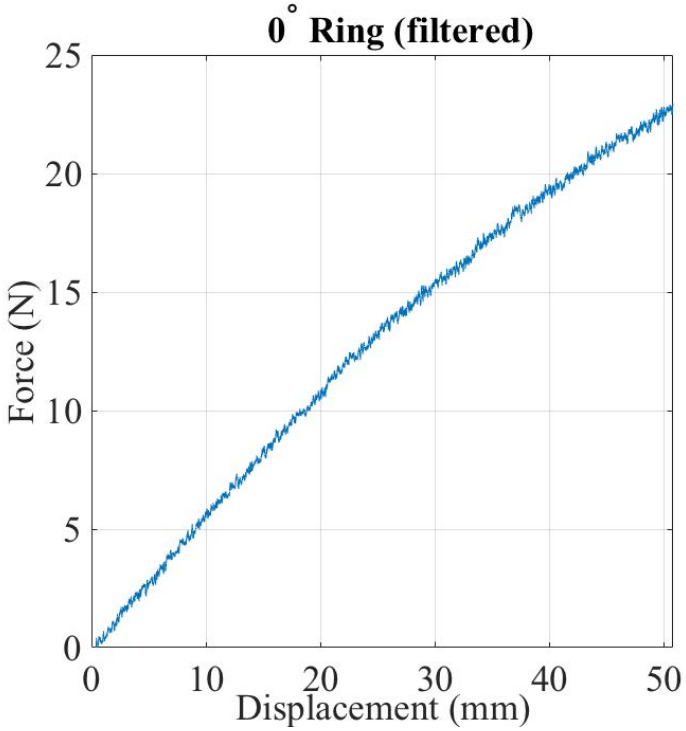

Figure 67. Filtered result of the 0° ring tested in the Acumen.

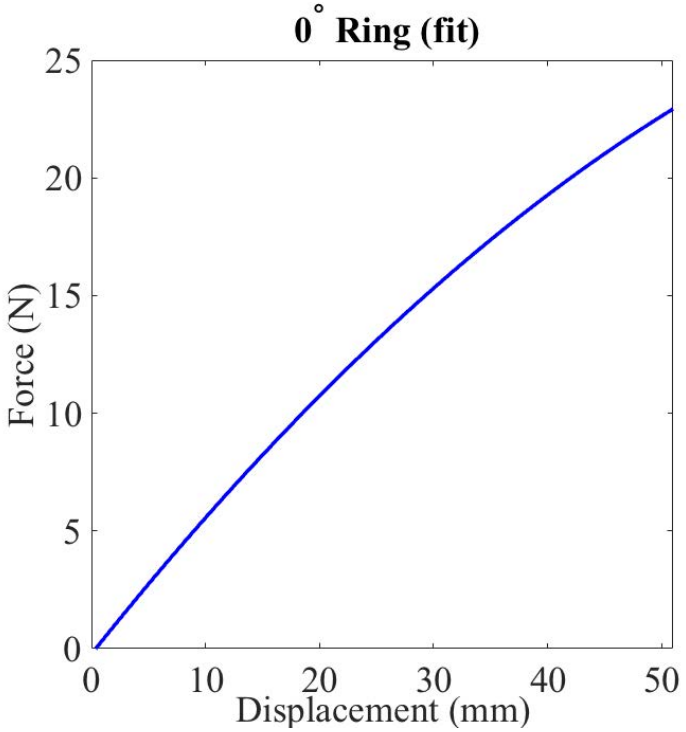

Figure 68. Curve-fit of the experimental result for the 0° ring tested in the Acumen.

The same loading rate and condition was used to test the 45°-orientation ring sample. The results are presented in Figures 69 and 70.

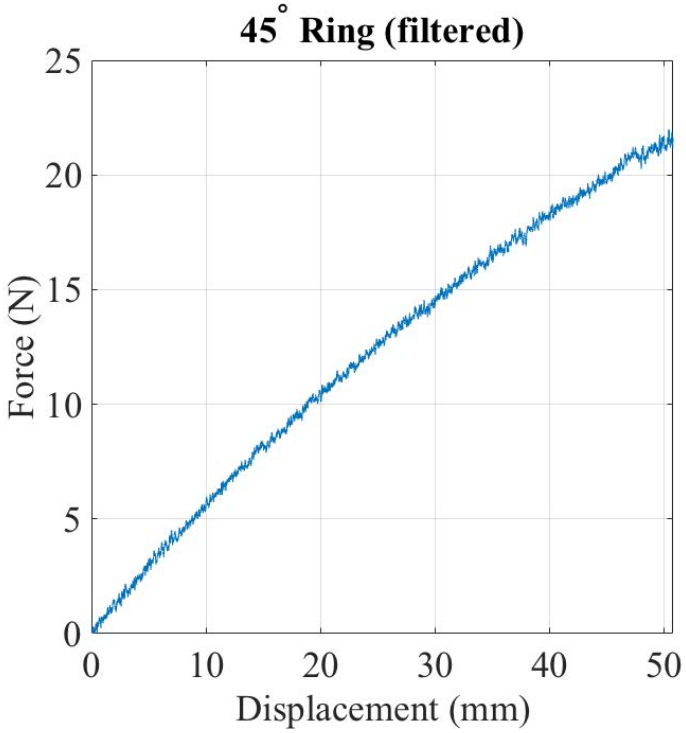

Figure 69. Filtered result of the 45° ring tested in the Acumen.

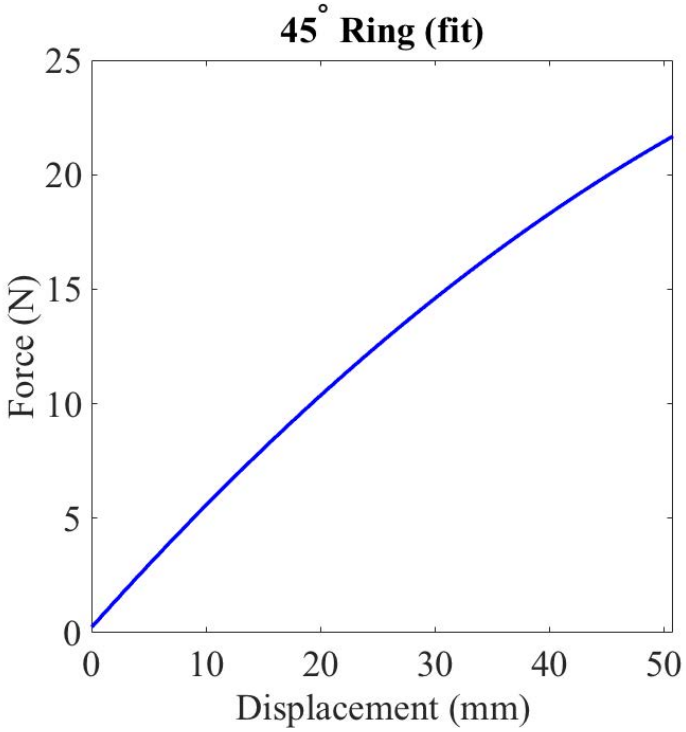

Figure 70. Curve-fit of the experimental result for the 45° ring tested in the Acumen.

The results for the 90°-orientation ring sample are presented in Figures 71 and 72.

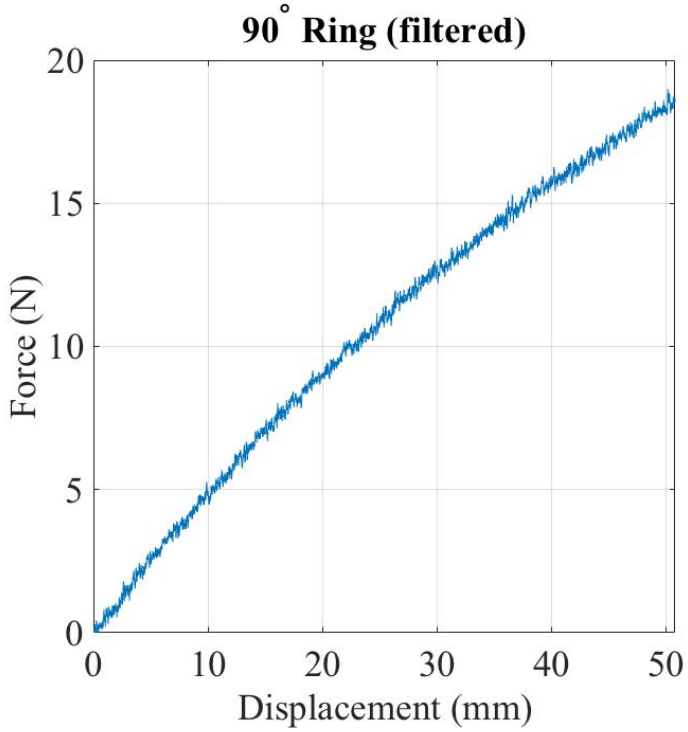

Figure 71. Filtered result of the 90° ring tested in the Acumen.

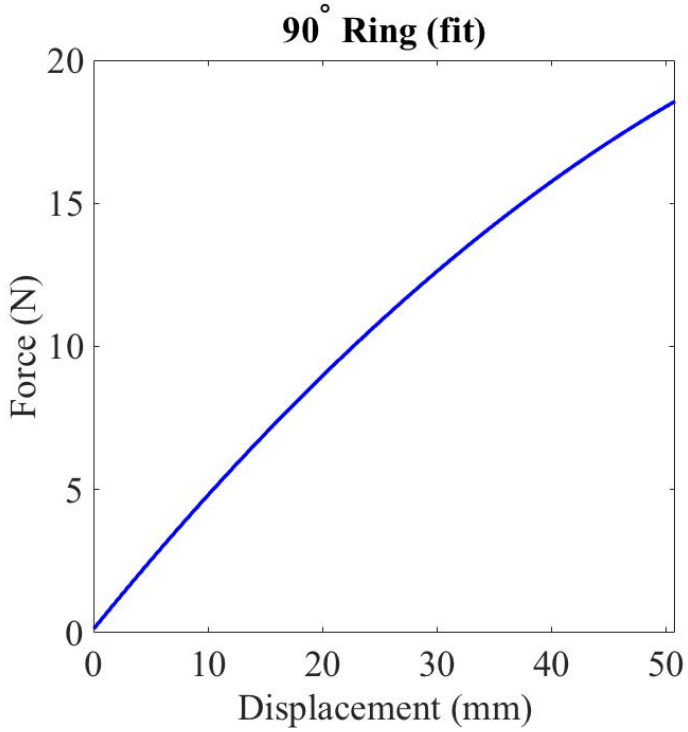

Figure 72. Curve-fit of the experimental result for the 90° ring tested in the Acumen.

The results for all three orientations are compared in Figure 73. It is clear that the 0° ring exhibited higher stiffness than the other two orientations. The 90° ring was the least stiff. The curve for the 90° is noticeably lower than the other orientations. The maximum force at the top vertex for the 90° ring was 18 N at a displacement of 50.8 mm. The maximum force for the 0° was 23 N at the same displacement. The maximum force for the 45° ring was 21 N. The 45° ring's response was in between the response for the 0° and 90° but was closer in magnitude to the 0° response. The 0° and 45° orientations exhibited the same general trend in their response. The shape of the 90° curve is aligned with the other orientations but the difference in magnitude is significant.

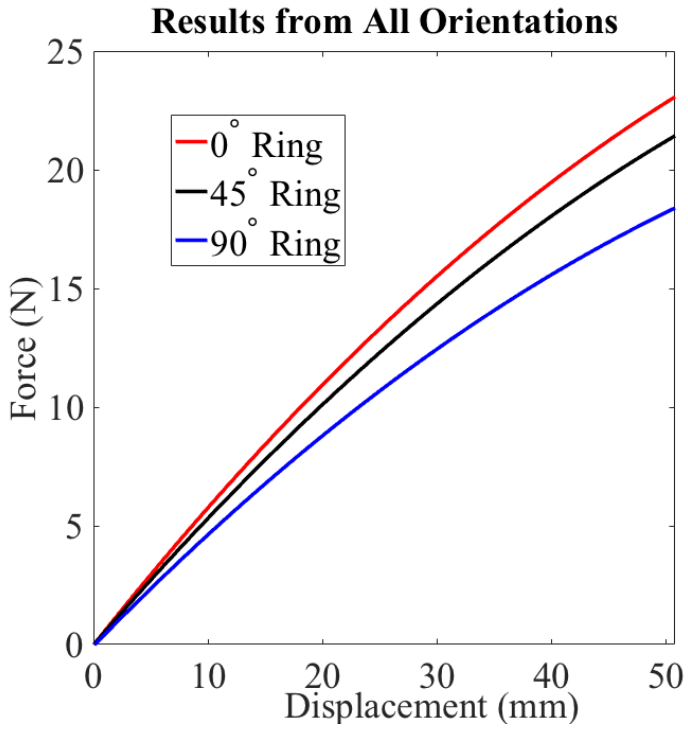

Figure 73. Comparison of the experimental results for each ring orientation gathered from the Acumen test rig.

Figure 74 depicts the general progression of the test from start to finish. The particular figure features the test for a 0° ring and provides a view of the sample at four different displacement values.

(a) 0 mm Displacement

(b) 25.4 mm Displacement

(c) 38.1 mm Displacement

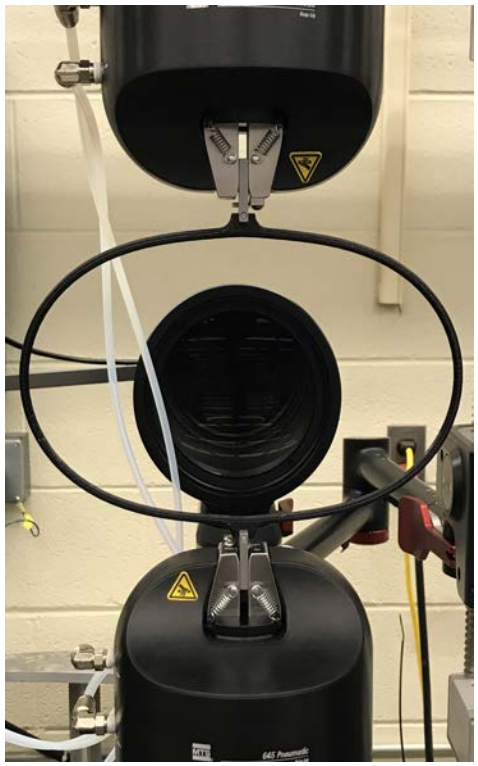

(d) 50.8 mm Displacement

Figure 74. The deformed state of a ring through at different stages of the compression loading for a 0° ring.

Verification of MTS Landmark.

As discussed in Chapter 3, the MTS 858 Landmark was equipped with a 25 kN load cell. The largest forces seen in the MTS Acumen 3 experiments was around 25 N. This suggests that the maximum force of a ring sample is 0.1% of the Landmark's FS output. A series of tests were conducted with the Landmark to gauge it's ability to accurately measure the forces from the rings. The results from the Landmark were compared to the results gathered from the Acumen. The general trend was very similar but the magnitude was off. Therefore, manipulation of the Landmark data was required to gain a close match between the two systems.

The results from the Landmark were vertically offset by a small magnitude throughout the response. They also had a chaotic period in the beginning of the response most likely due to the presence of small forces that were too far out of the operating range. An example of this data is provided in Figure 75.

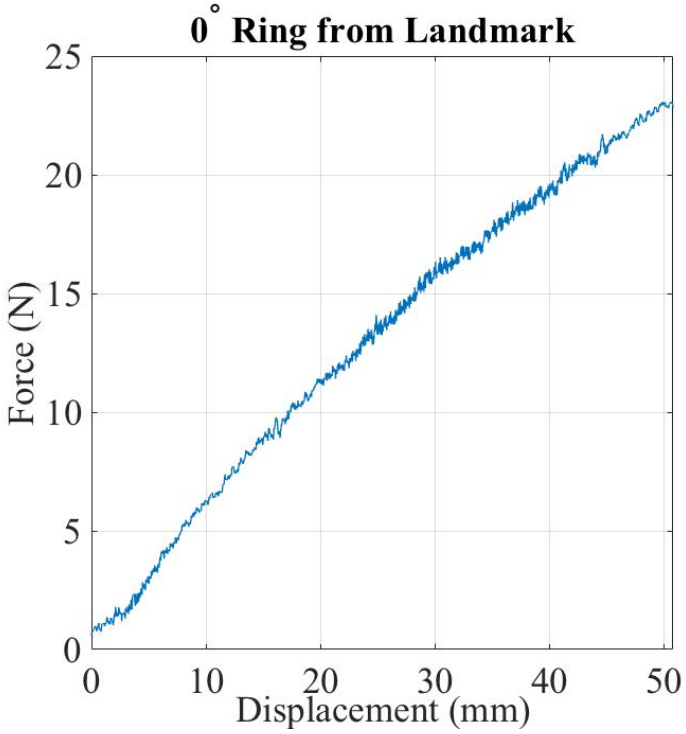

Figure 75. Result of a 0° ring tested in the Landmark with no manipulation to the data.

Despite having a shaky beginning and being offset, the data from the Landmark was manipulated to match the data from the Acumen. The beginning data was chopped off to get rid of the fluctuation. Then, a small value of force was subtracted from the force data. The value used for subtraction was determined by matching the Acumen data as closely as possible. After the adjustments were made, the results from the Landmark matched the Acumen very well. The comparison is presented in Figure 76.

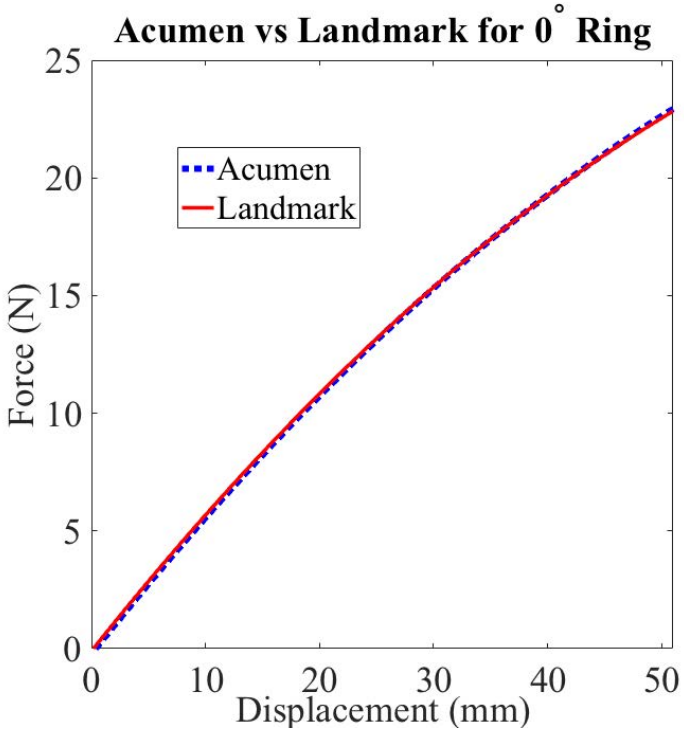

Figure 76. Adjusted result of a 0° ring tested in the Landmark and compared with the result from a ring tested in the Acumen.

As seen in Figure 76, the response is nearly identical from both testing machines. The Landmark was used for testing the different ring types. Two samples per ring orientation were tested in order to verify the results from the Landmark were accurate since the forces were significantly smaller than it's rated FS range. The ensuing section presents the results from the MTS 858 Landmark testing rig, in which all the results were adjusted in the manner described.

MTS Landmark Results.

The same filtering algorithm used for the Acumen results was used to filter the raw data that was output from the Landmark. A comparison of the raw versus filtered data is given in Figure 77.

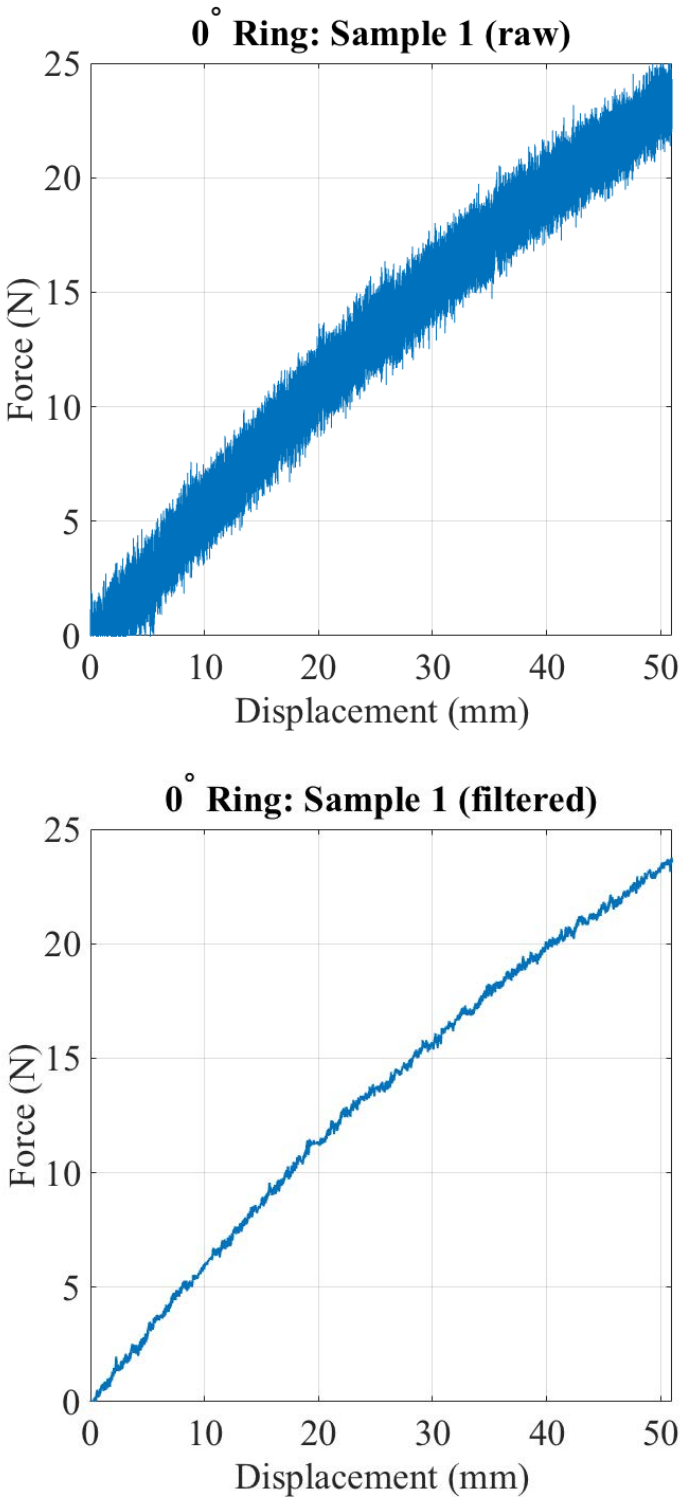

Figure 77. Experimental results for the first sample of the 0°-oriented ring comparing raw (top) vs filtered (bottom) data.

The results for two samples of the 0°-orientation are presented in Figure 78.

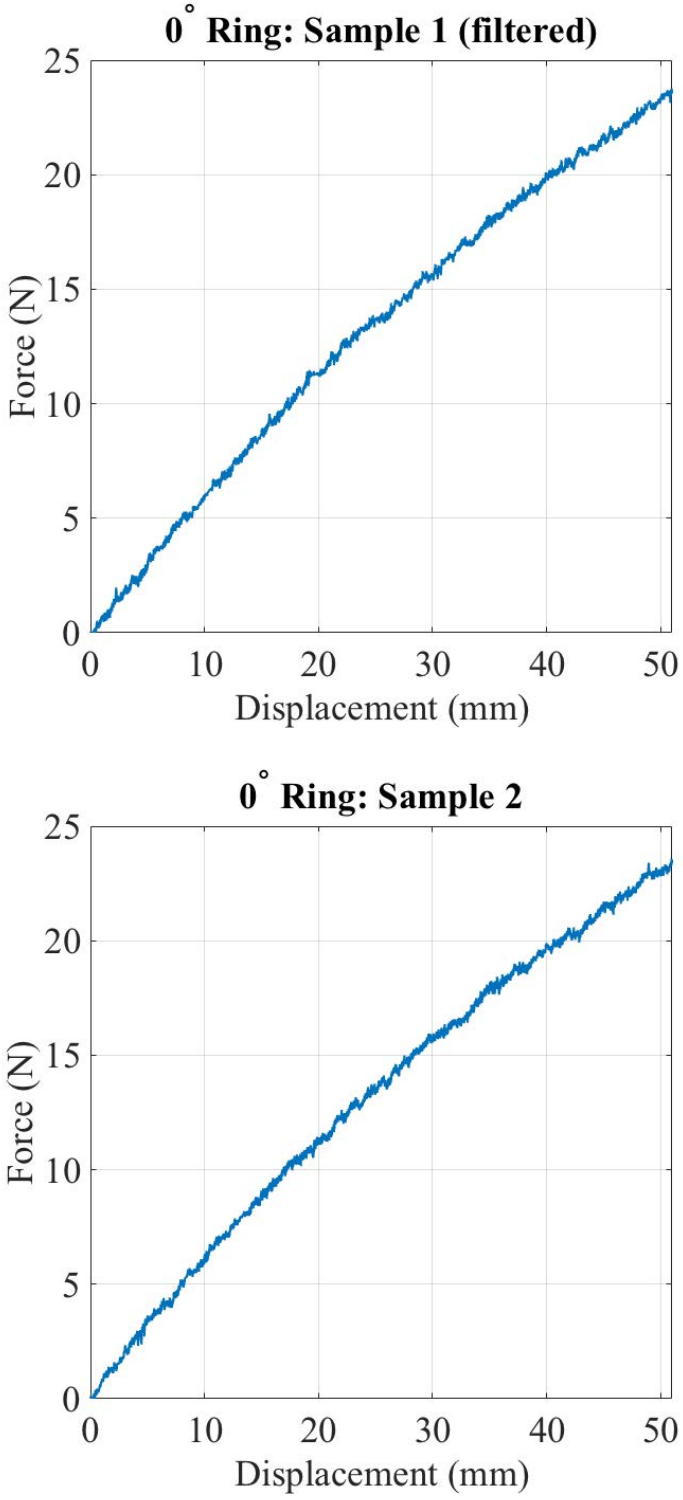

Figure 78. Experimental results for the 0°-orientation from the Landmark.

The same loading rate and condition was used to test two samples of the 45°-

orientation. The results for the two sample are presented in Figure 79.

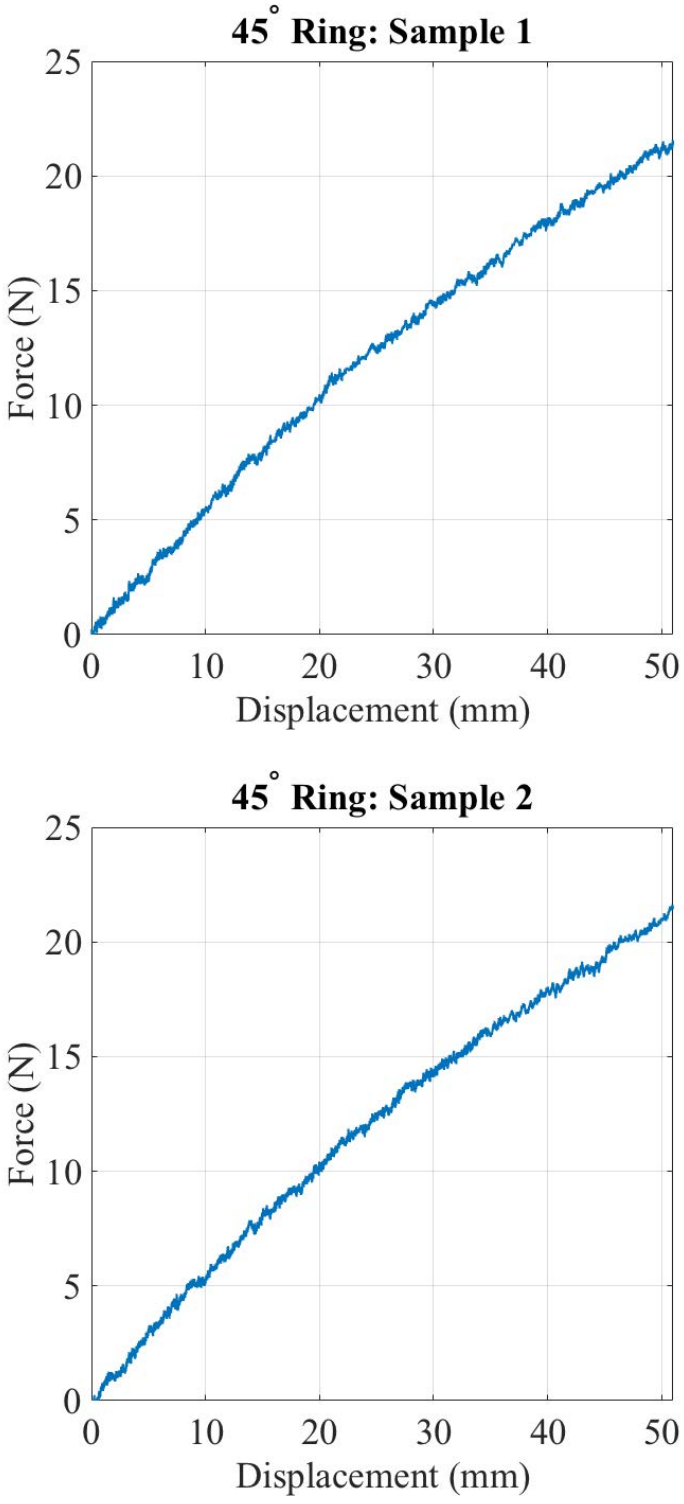

Figure 79. Experimental results for the 45°-orientation from the Landmark.

The same procedure was repeated for the 90°-orientation. The results are provided in Figure 80.

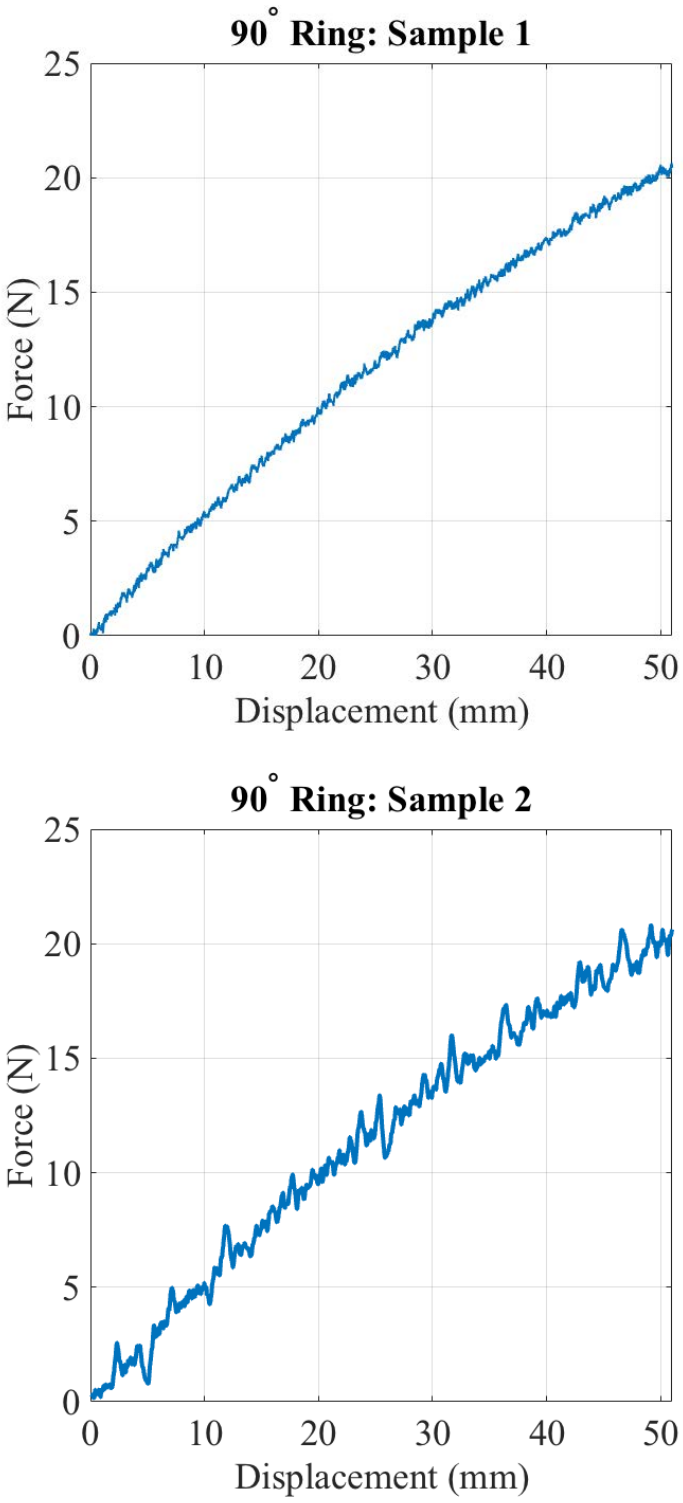

Figure 80. Experimental results for the 90°-orientation from the Landmark.

The data for each ring was fit with a curve to capture the trend of the response

and provide a clearer comparison between the three cases. The behavior of the rings, with this specific loading condition and rate, is presented in Figure 81.

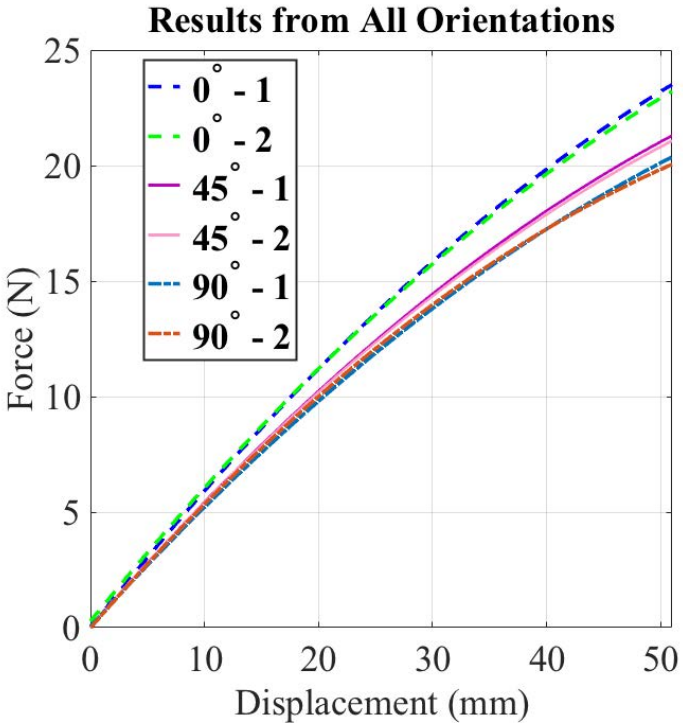

Figure 81. Experimental results for all three orientations from the Landmark.

The same trend is observed in the comparison of the rings that was found in the Acumen testing results. The 0° ring is the most stiff while the 90° ring is the least stiff. The 45° ring lies in between the other two but it is closer in magnitude to the 90° ring. This was not the case in the comparison from the Acumen results. It can also be observed that the maximum force for the 45° and 90° rings are higher than the maximum force reported for the Acumen results. This difference may be due to the Landmark's inability to measure smaller forces. The 0° ring appears to be at the same magnitude of force as the Acumen result (Figure 73).The 0° ring exhibits higher forces than the other two configurations, which enables the Landmark's load cell to register it's response more accurately.

The slight difference in response between the Acumen and Landmark suggest that

the Landmark is not perfectly suited to the small forces present in the compression of the rings. It was shown and proven that the data can be manipulated to match the overall trend. However, the resolution and accuracy of the results suffer. The Acumen's 250 N load cell is more suitable for operating within the loading range of the rings.

A visual progression of the compression loading process for the Landmark testing machine is laid out in Figure 82. The ring begins with a circular profile but as it's loaded the profile becomes oblong. The result is an elliptical profile, in which the sides of the rings take on a noticeably higher curvature in comparison to the spherical profile.

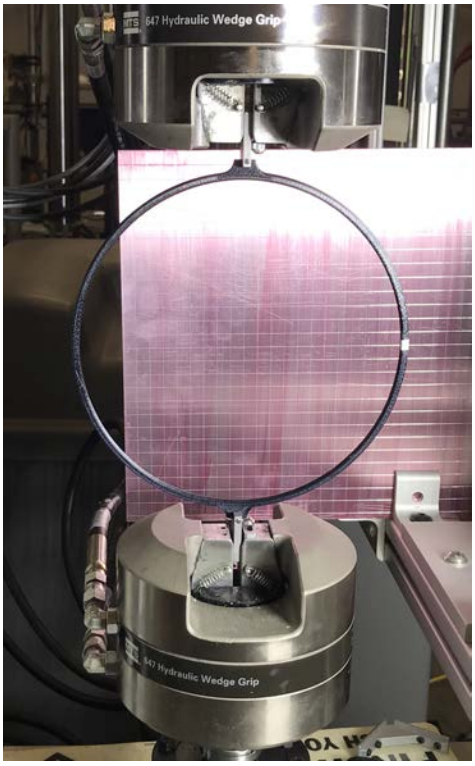

(a) Beginning of test

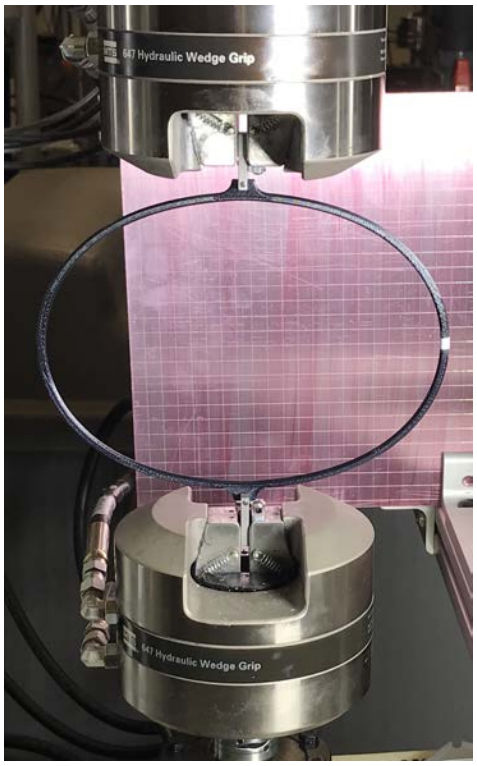

(b) Mid-test

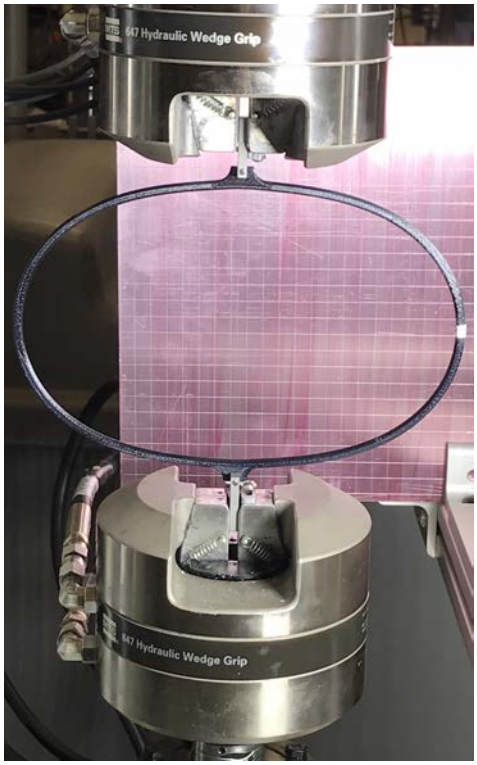

(c) End of test

Figure 82. The deformed state of a ring through at different stages of the compression loading for a 0° ring.

Loading Rate Study.

A series of tests were conducted to investigate the effects of loading rate on a specimen's response. A 0° ring was tested, with the same loading condition, at three different loading rates: 1.27, 2.54, and 12.7 $\frac{mm}{min}$. The responses are compared against one another in Figure 83.

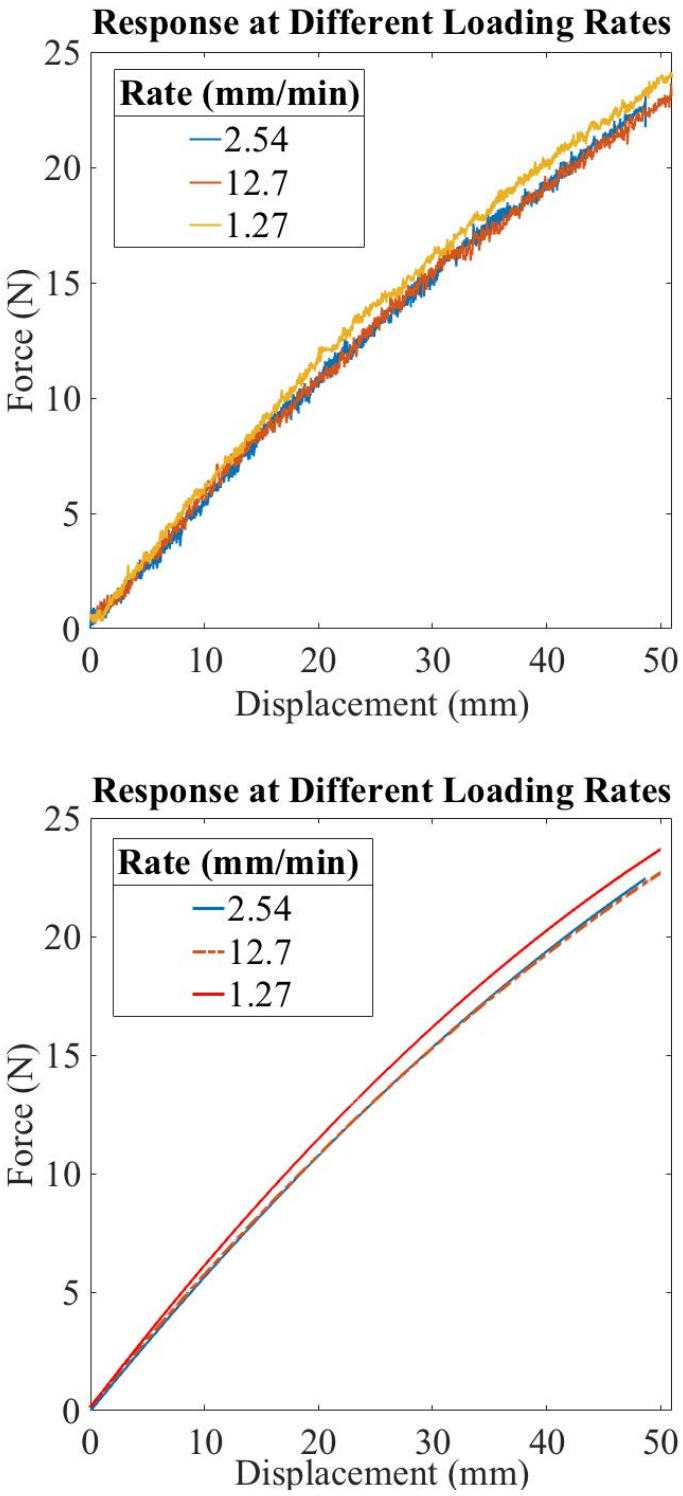

Figure 83. Results from three different loading rates for the 0° ring–raw data (top) and curve fitted data (bottom).

It is evident that the loading rate affected the response from the rings. The

difference in response between the 1.27 and 12.7 $\frac{mm}{min}$ rates is appreciable. The aim of the analysis was to test the rings in a quasi-static environment–slow enough so that inertial effects can be neglected. The results from the different loading rates suggest that inertial effects are significant at a loading rate of 12.7 $\frac{mm}{min}$. This rate imposes dynamic effects on the ring, which was not the intent of the analysis. The FEA was setup to be static so that the results could be directly compared to the experimental results. In order to avoid dynamic effects, all of the compression tests were run with a conservative prescribed loading rate of 1.27 $\frac{mm}{min}$.

Fracture.

On two instances, the 90° ring fractured before reaching the prescribed displacement. The rings fractured at the same region and in the same manner. The location of the fracture was at the right side of the ring and is shown in Figure 84. From inspection of the magnified region, it is concluded the ring split apart at the seam between two print layers.

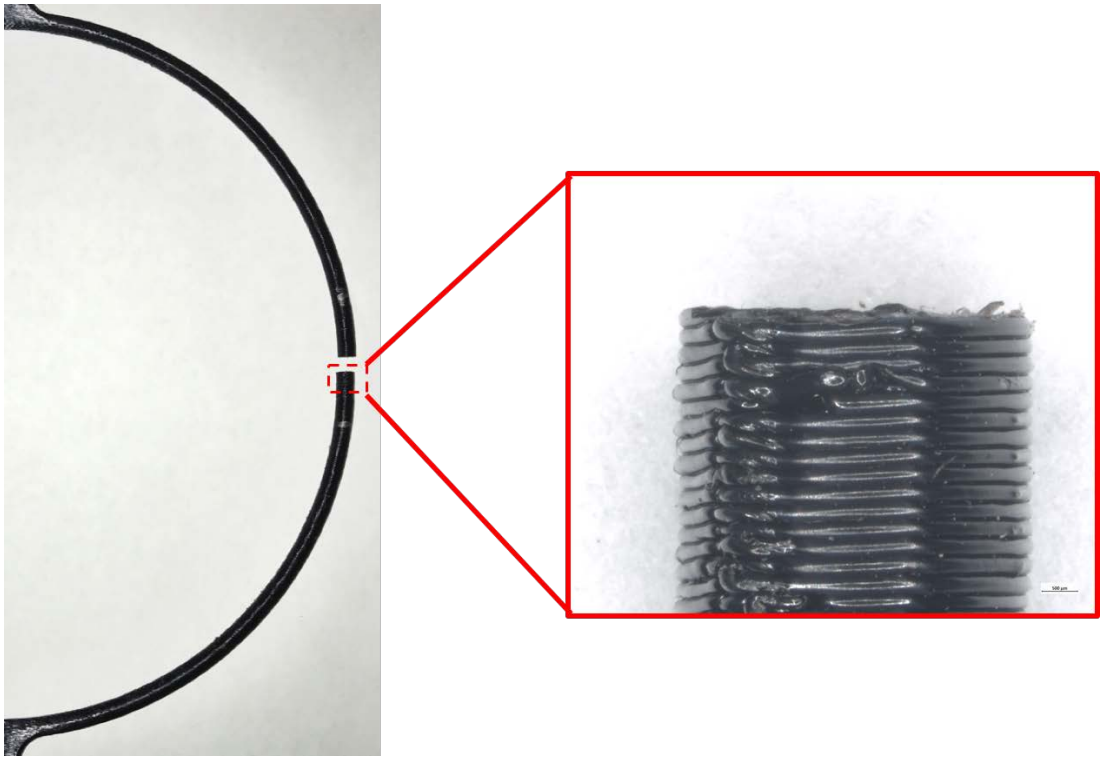

Figure 84. The location of fracture for the failed 90° ring with a magnified side view of the bottom fracture surface.

The fitted curves of the data for each fracture case are presented in Figure 85. The rings fractured at similar conditions. The first ring failed at a displacement of 43.6 mm; the second ring failed at a displacement of 50 mm.

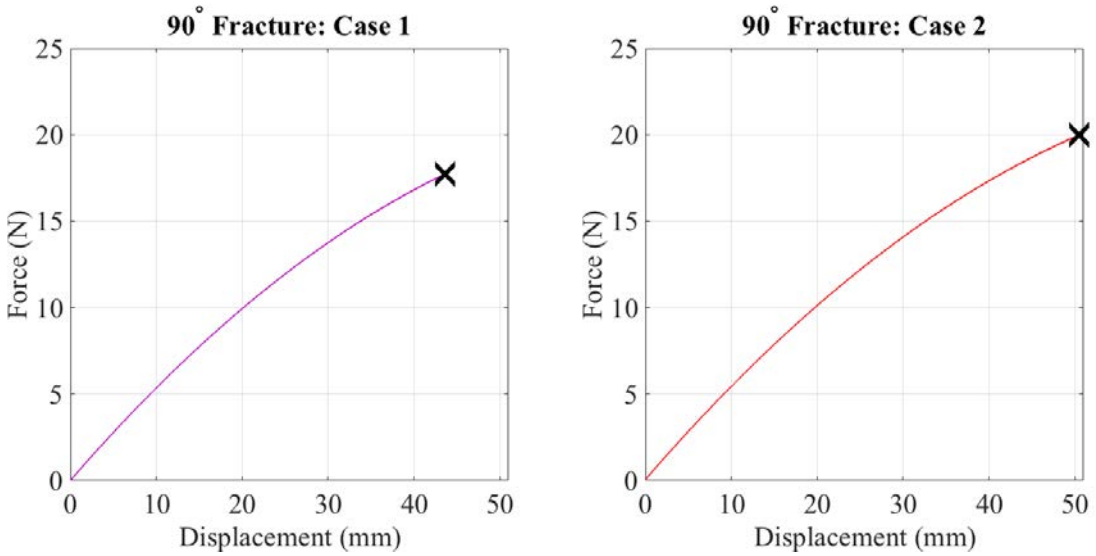

Figure 85. Location of fracture for two different samples of the 90° ring.

The print orientation appears to be the driving factor behind the failure. The other rings did not fracture under the same loading conditions, hence the failure is not indicative of the material's inability to withstand the loading. The sides of the ring endure significant deformation throughout the duration of the test. A side-by-side comparison of the beginning and end state of the ring is presented in Figure 86. The white rectangle on the ring highlights the general vicinity in which the 90° samples fractured. This deformation creates large stresses at these regions in which the layers of the 90° print become extremely susceptible to splitting apart. This phenomenon is what occurred in the two failure cases for the 90° samples.

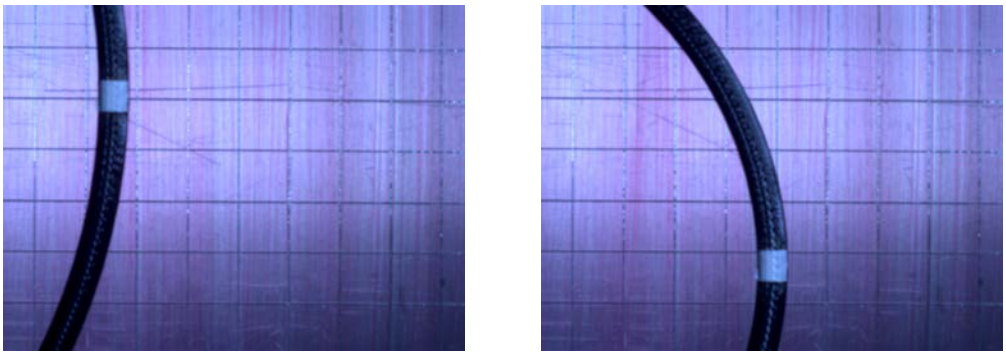

Figure 86. The progression of deformation for the side of a ring during testing with the beginning state (left) and end state (right).

4.3 Material Property Verification

The rings exhibit nonlinear behavior in their response for both the experimental and analytical results. However, there is a region of linear behavior present in the response before it becomes nonlinear. This region generally lies within the δ range of 0 - 25.4 mm. It is in this region in which K was measured. It was measured by fitting a line in the linear region of the response for each ring type. The slope (m) of this line is the value of K. The m was found for each sample of each orientation from the experimental data. An average of the value was used to define K_{exp} for each type. Figure 87 illustrates the line-fitting process for the linear region of a response.

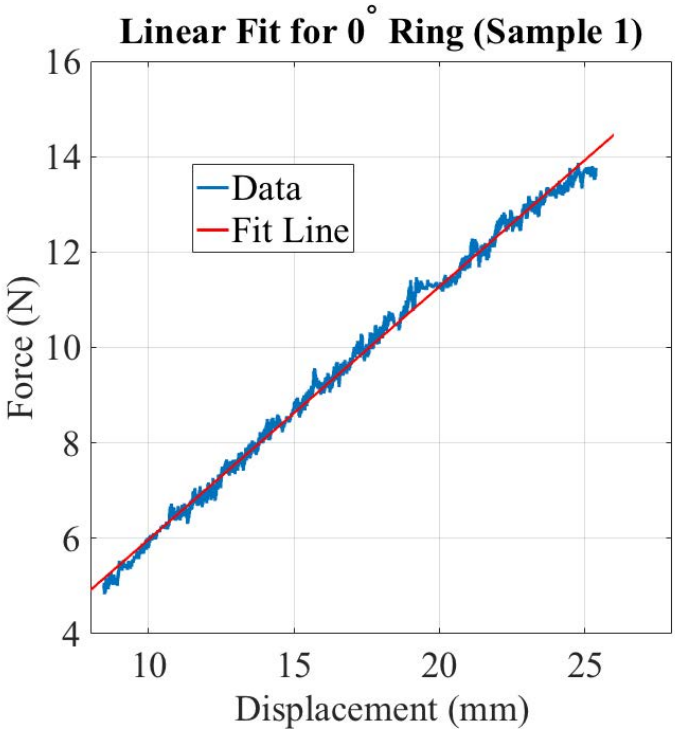

Figure 87. Fitting a line on the linear portion of the first 0° sample.

The values for K_{exp} were found for each orientation from the experimental data. Next, the same linear fit process was applied to the results generated from Abaqus. The process for the FEA analysis began with assigning the model a discretionary value of E and tracking the linear portion of it's response in the same manner as the

experimental data. The slope of the linear portion of the FEA output was found as shown in Figure 88. The resulting K_{FE} that was determined was compared to the K_{exp}. If the values were not equal then the process was repeated by adjusting E and assigning the new value to the model. This iterative process was followed, for each ring orientation, until an exact match was found between K_{exp} and K_{FE}. Once the values matched, the assigned E was taken as the value for the respective ring type. This iterative process is depicted in the schematic of Figure 89. The results that were found for each ring orientation using this method are laid out in Table 2.

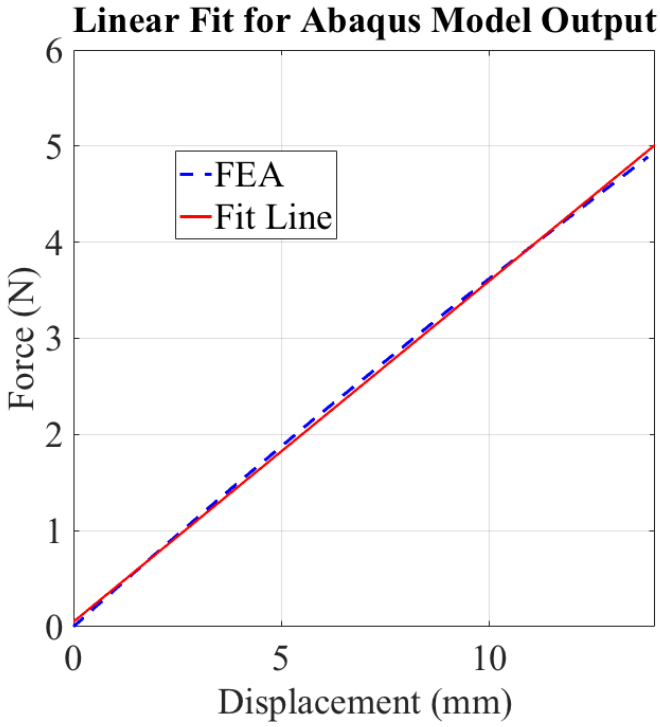

Figure 88. Demonstration of fitting a line on the linear portion of a result from Abaqus first.

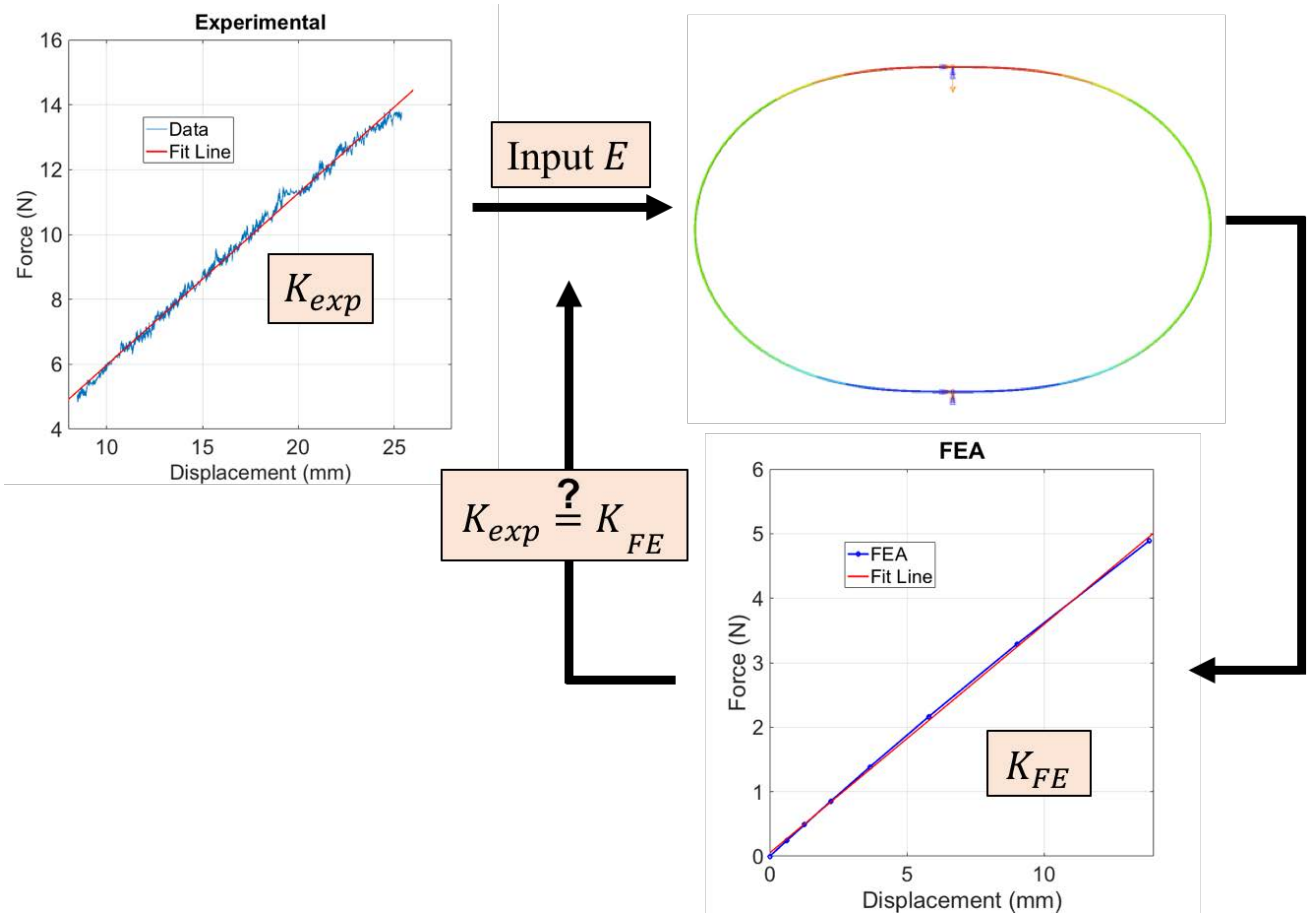

Figure 89. Schematic of the iterative method used to find the E value for each ring.

Material Properties		
Orientation	Stiffness K (N/mm)	Modulus E (GPa)
0°	0.522	2.55
45°	0.482	2.35
90°	0.456	2.22

Table 2. The K and E values found from the iterative matching method between the experimental and FEA results.

Moduli Comparison.

The iterative method was used to find a value for E for each ring orientation. The manufacturer provided a table of values for three different moduli for the material: tensile, compressive, and flexural. The values for these moduli are provided in Table 3 for the XZ and ZX build orientations. XZ is the 0° build orientation. ZX is the 90° build orientation.

ULTEM 9085 Published Moduli (GPa)			
Orientation	Compressive	Tensile	Flexural
0°(XZ)	7.01	2.15	2.30
90°(ZX)	1.73	2.27	2.05

Table 3. The moduli values from the manufacturer's table for ULTEM 9085 [29].

The value for E, found from the iterative method, was compared with the values provided by the manufacturer. The manufacturer's E values were input into the FEA model. Figure 90 shows the response for all the values for the 0° model. The "FEA Fit" is the E that was found to fit the experimental data. It does not align well with the manufacturer's compressive E. It is closer in response to the flexural E and tensile E.

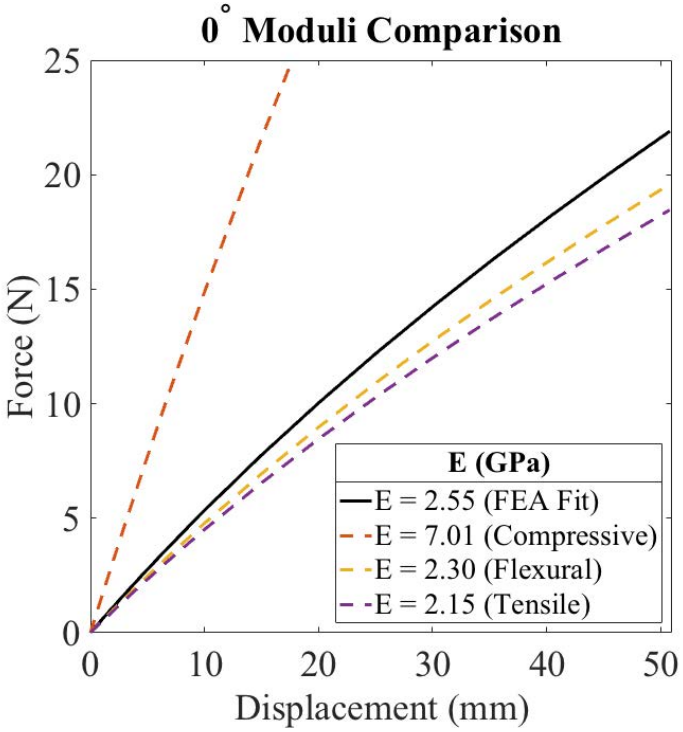

Figure 90. Comparison of the E values that were published by the manufacturer and the E that was found to match the experimental data for the 0° model.

The same comparison was made for the 90° model. The results are given in Figure 91. Similar to the 0° case, it is noticeable that the 'FEA Fit' does not align with the compressive E. It is more aligned with the flexural E and tensile E.

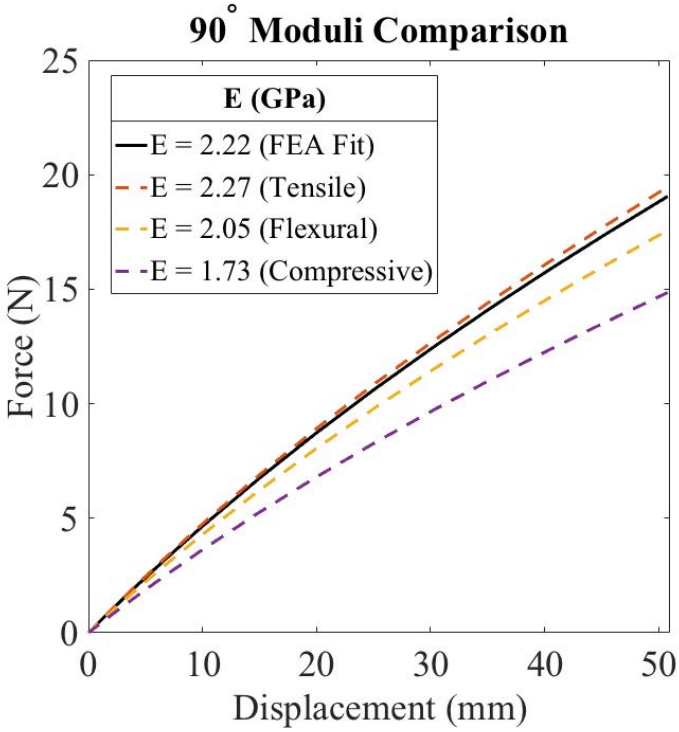

Figure 91. Comparison of the E's that were published by the manufacturer and the E that was found to match the experimental data for the 90° model.

The difference in response across the values of E suggest that E is influenced by the shape of the part. The ring's unique shape, mainly it's curvature, inhibits the part from experiencing pure axial tension or compression. There is significant bending in the model as it endured the compressive loading, which indicates the flexural E value is more relevant to the ring.

The material properties provided by the manufactuer were the results from tensile, compressive, and flexural tests on parts with no curvature [36]. The tensile properties were a result of uniaxial tension on a dogbone specimen [36]. The compressive properties were a result of uniaxial compression on a rectangular prism [36]. The flexural properties were from three-point bending tests on a rectangular specimen [36]. The shape of these samples are not similar to the shape of ring. Therefore, it is concluded that the value for E is influenced by the shape of the part under consideration. The rings for this research exhibited E values similar to the published flexural and tensile

values.

4.4 FEA

The different E values that were found using the iterative method were inserted back into the Abaqus models. An analysis was carried out for each respective ring orientation to examine and compare the FEA to the experimental results. Both ring models, basic and tabbed, were used for the comparison to identify which model better represents the 3D printed ring. The results for the basic ring model are presented first. The results for the tabbed ring model are presented afterward.

Basic Ring Model.

The result for the 0° basic ring model, at a 50.8 mm displacement, is shown in Figure 92. The results for the 45° and 90° models are presented in Figures 93 and 94. Additional plots of the stress distribution and displacement increments for the various models are located in Appendix B.

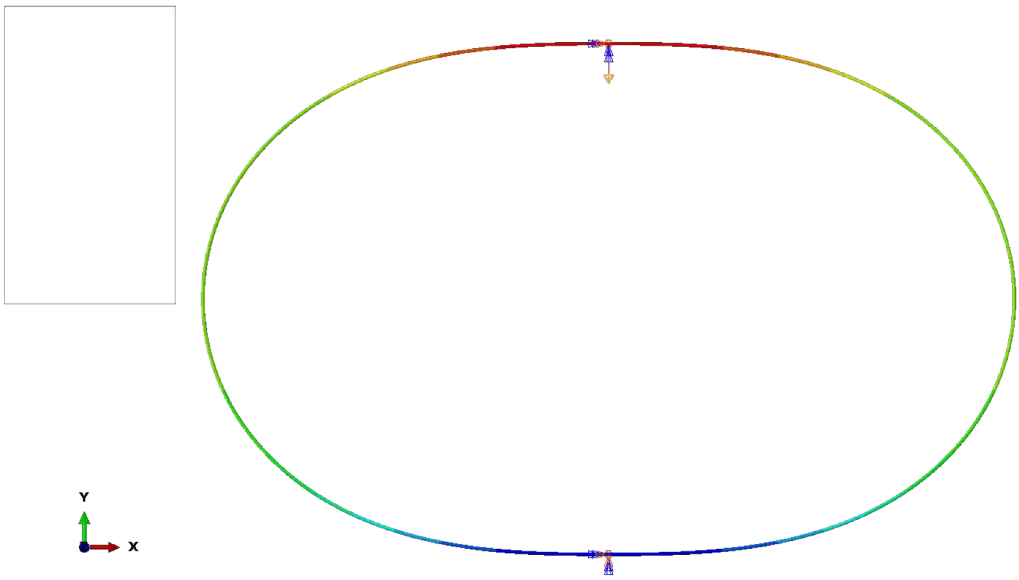

Figure 92. The 0° basic ring model displaced at 50.8 mm.

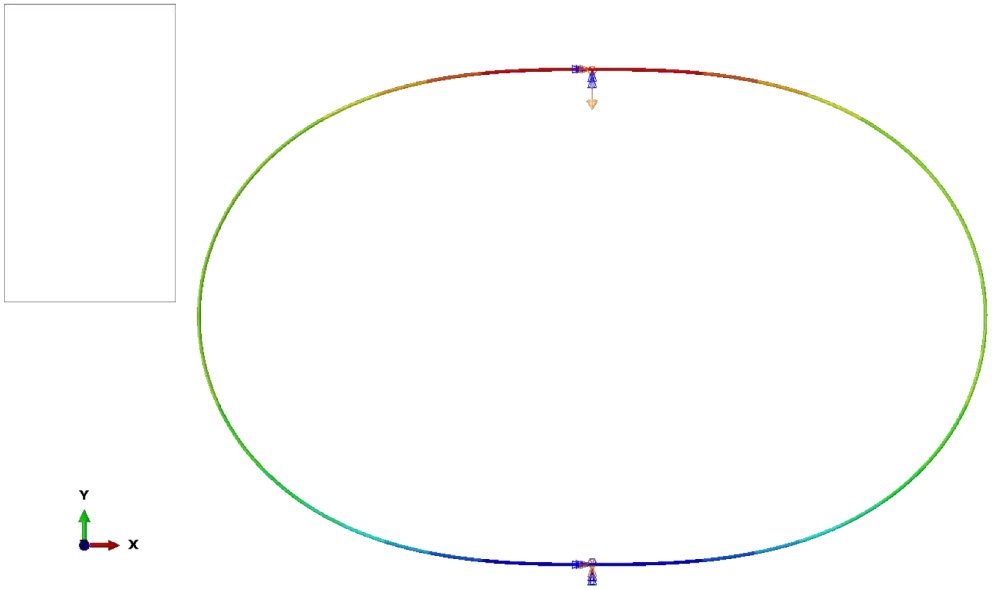

Figure 93. The 45° basic ring model displaced at 50.8 mm**.**

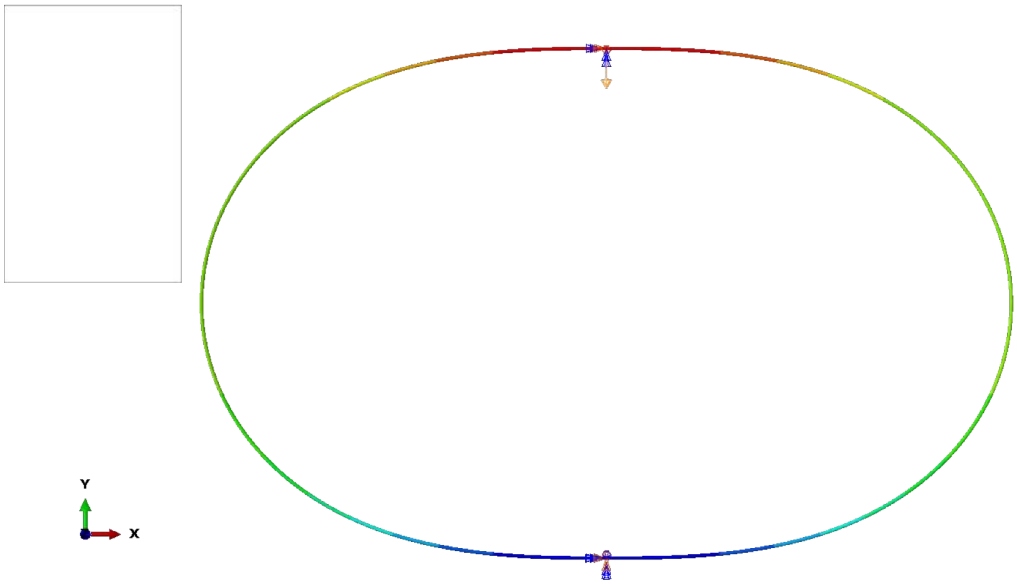

Figure 94. The 90° basic ring model displaced at 50.8 mm**.**

A comparison of the actual ring with the FEA basic ring model–before any displacement was imposed–is provided in Figure 95. A comparison of the deformed ring, at the full 50.8 mm displacement, between the experiment and FEA model result is shown in Figure 96. It is observed that the rings take on the same general deformed

shape. An exact method of comparison would require the use of an accurate measuring technique such as digital image correlation. For this analysis, the similarity in overall shape provides a coarse verification that the FEA model is representative of the real, physical model.

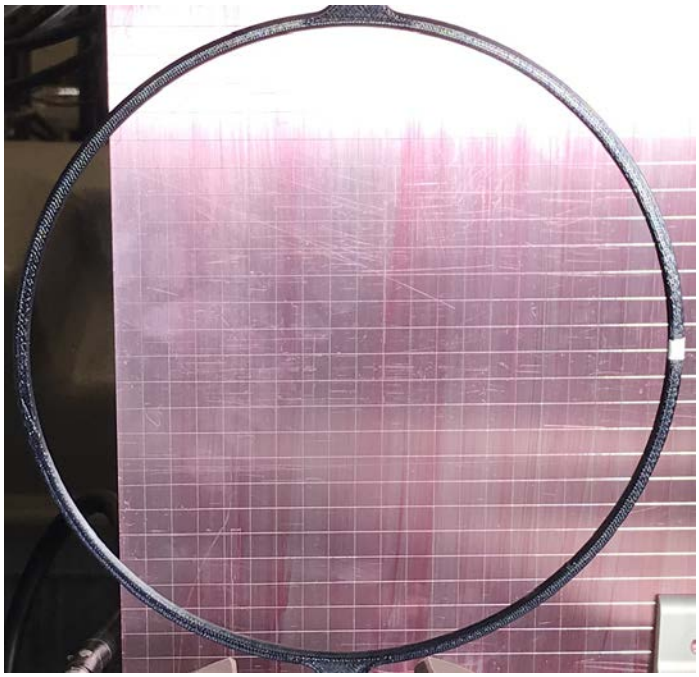

(a) Undeformed ring in experiment

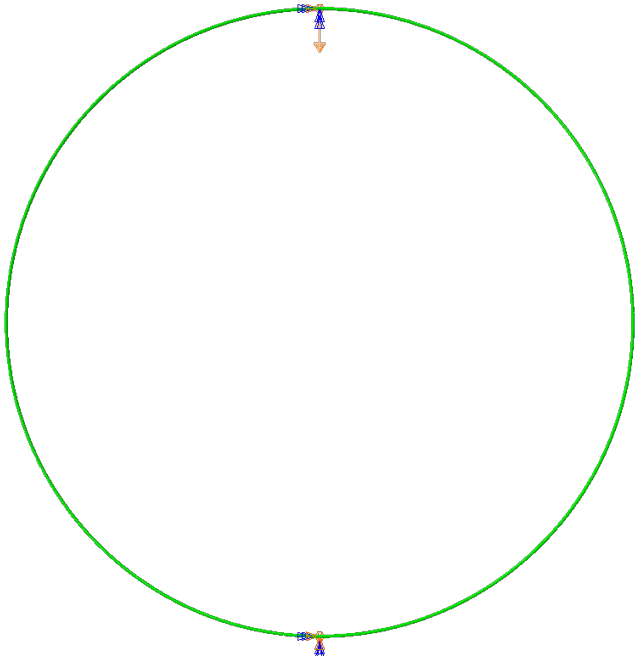

(b) Undeformed basic ring model in FEA

Figure 95. The undeformed state of a ring, in which no displacement was imposed, from the experiment (top) and from FEA (bottom).

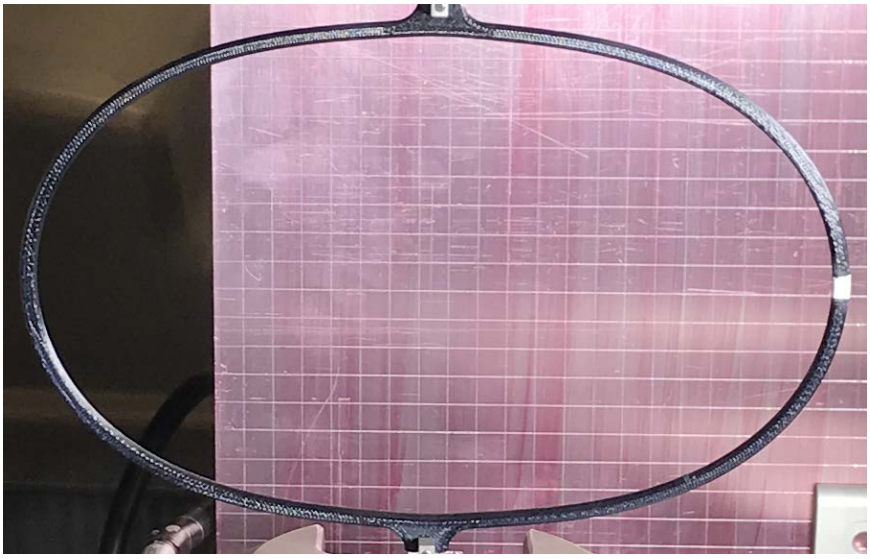

(a) Deformed ring in experiment

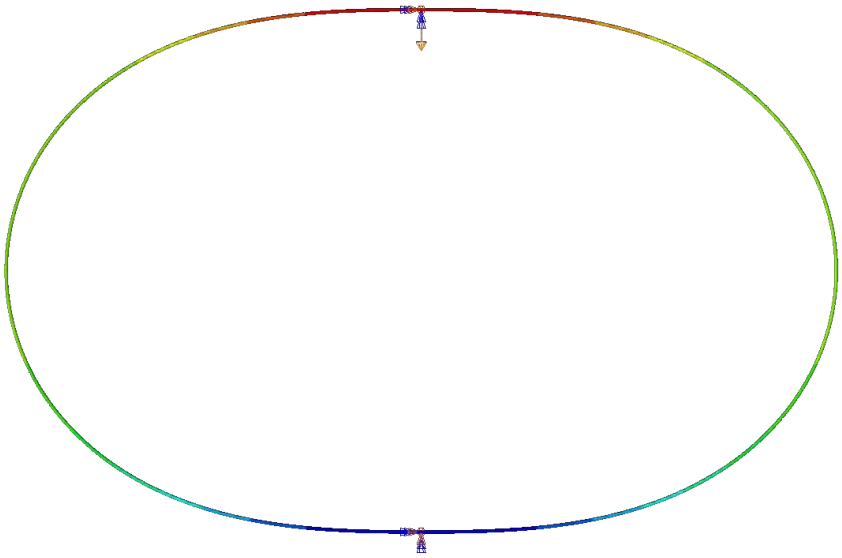

(b) Deformed ring in FEA

Figure 96. The deformed state of a ring from the experiment (top) and from FEA (bottom).

The FEA results for the basic ring model were compared to the experimental results from the Landmark to investigate the model's accuracy. The comparison for the 0°-orientation is shown in Figure 97.

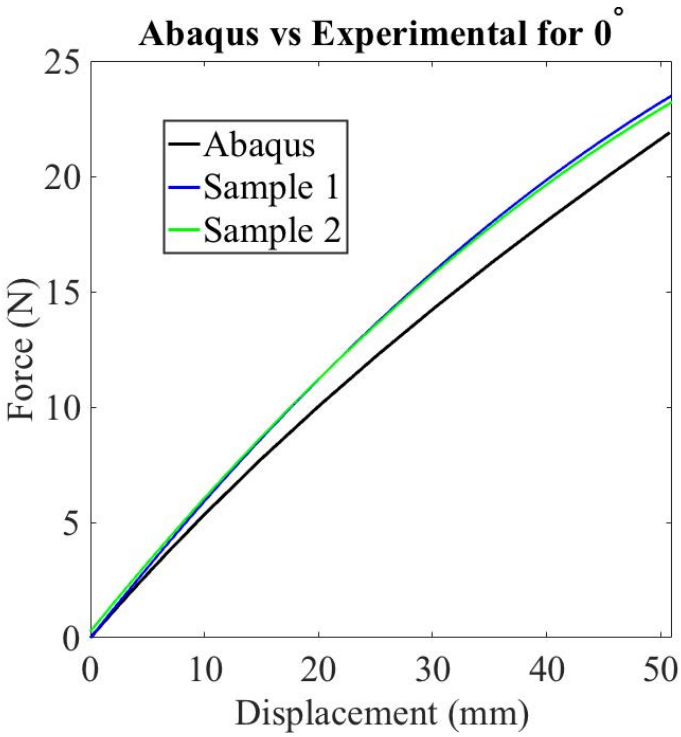

Figure 97. The comparison of results for the FEA 0° basic ring model and experimental results.

A comparative analysis for the other two orientations are given in Figure 98 and Figure 99.

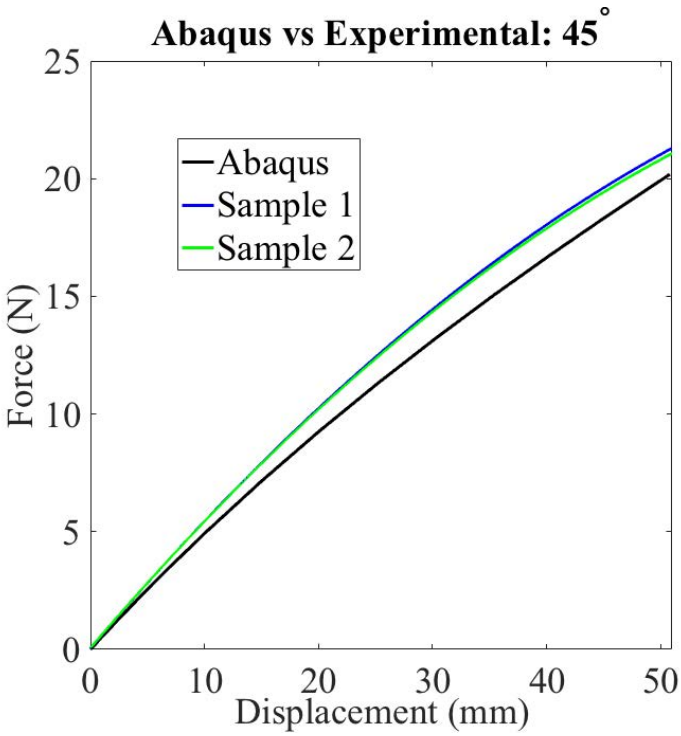

Figure 98. The comparison of results for the FEA 45° basic ring model and experimental results.

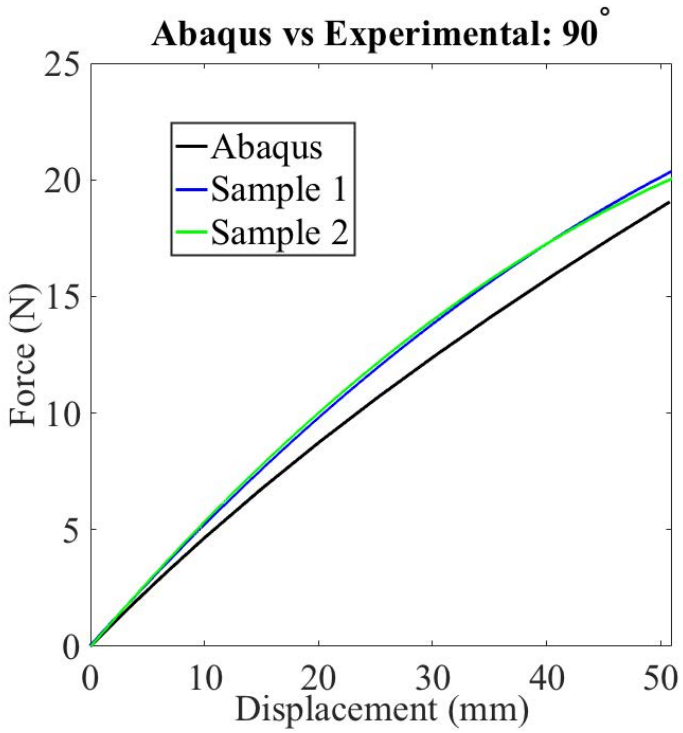

Figure 99. The comparison of results for the FEA 90° basic ring model and experimental results.

It is evident that the results from Abaqus follow the approximate trend as the experimental results. However, the Abaqus output is noticeably shifted downward and falls below all of the experimental results. A reason for this shift may be attributed to the lack of extra material at the top and bottom of the FEA model. The actual ring that was tested in the MTS had built-in tabs at the top and bottom. The overall height of these tabs was 9.1 mm. The t of the beam was 5.08 mm. Therefore, the regions where the tabs were located had nearly double the t compared to the rest of the part. The tabbed ring model accounts for this increase in t. It's performance is measured in the following section.

Tabbed Ring Model.

As discussed previously, the tabbed ring model accounted for the increased thickness at the top and bottom of the ring. A comparative analysis between the model

and actual ring is provided. First, pictorial results are compared at different stages of displacement. The four increments for comparison are: 0 mm, 25.4 mm, 38.1 mm, and 50.8 mm. Images were taken of the ring at these four increments while it was being compressed within the MTS. The images were edited to remove the background and foreground to highlight the ring's profile. Images were collected from Abaqus at the same increments for the tabbed ring model under the same loading. The results are presented in the following figures.

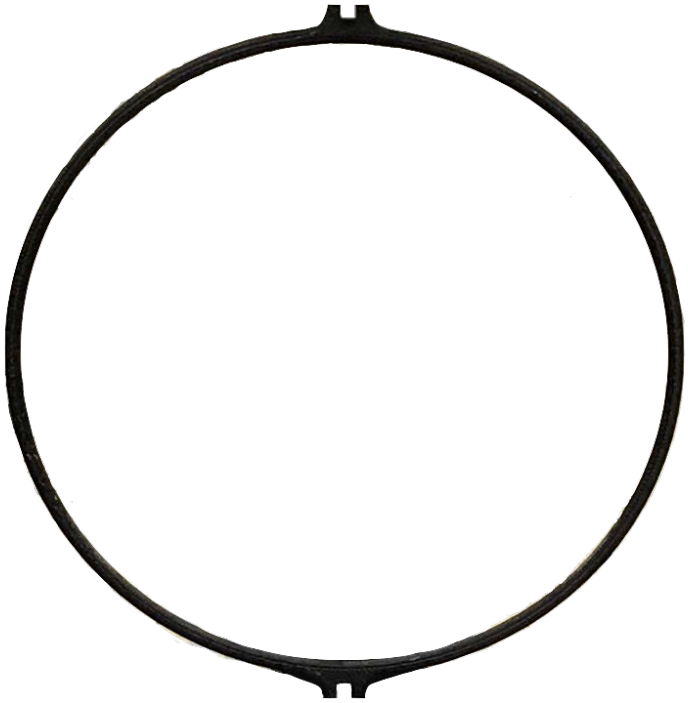

(a) Ring in experiment

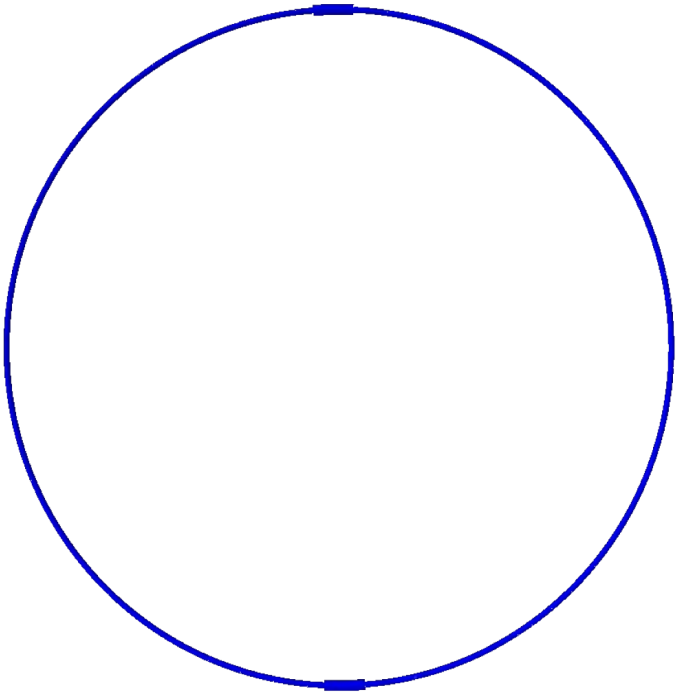

(b) Basic ring model in FEA

Figure 100. The ring from the experiment (top) and from FEA (bottom) at a displacement of 0 mm.

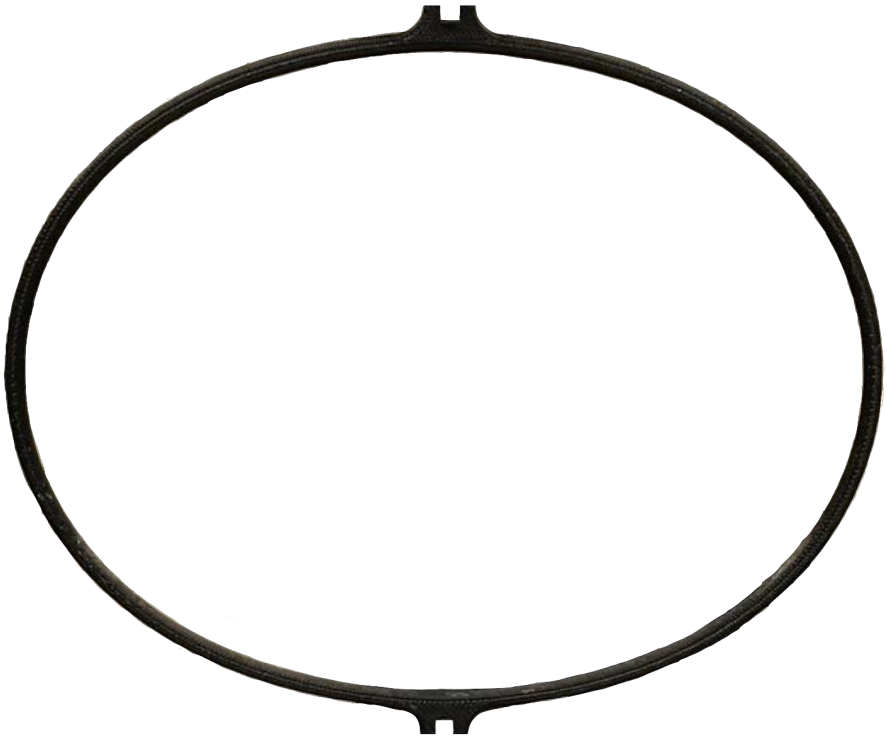

(a) Displaced ring in experiment

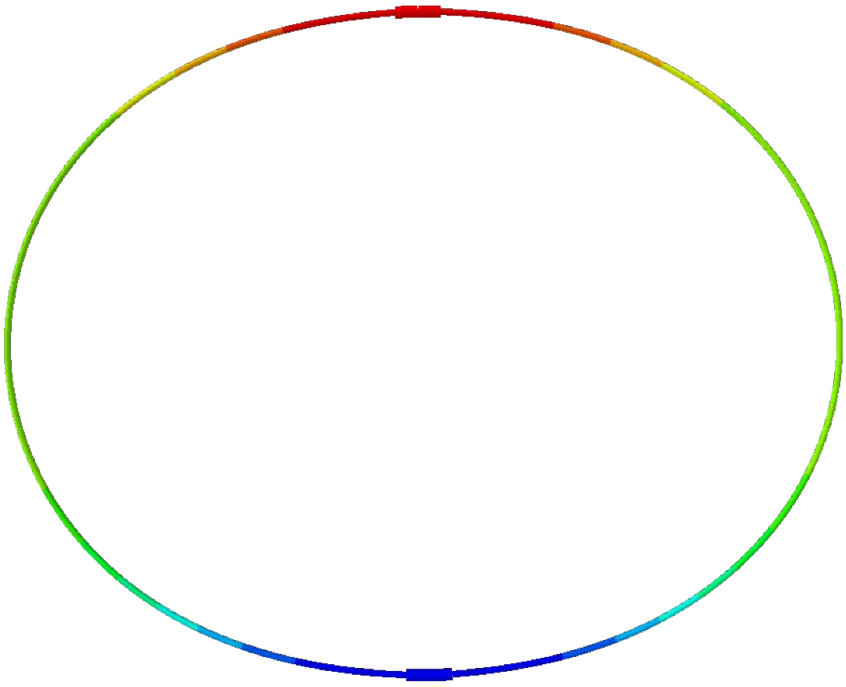

(b) Displaced basic ring model in FEA

Figure 101. The ring from the experiment (top) and from FEA (bottom) at a displacement of 25.4 mm.

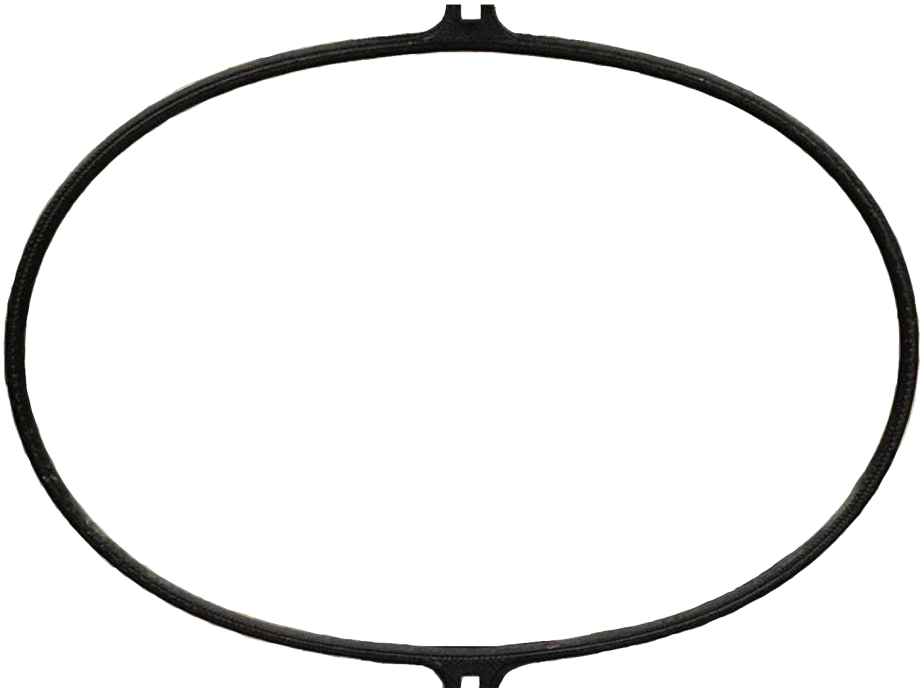

(a) Deformed ring in experiment

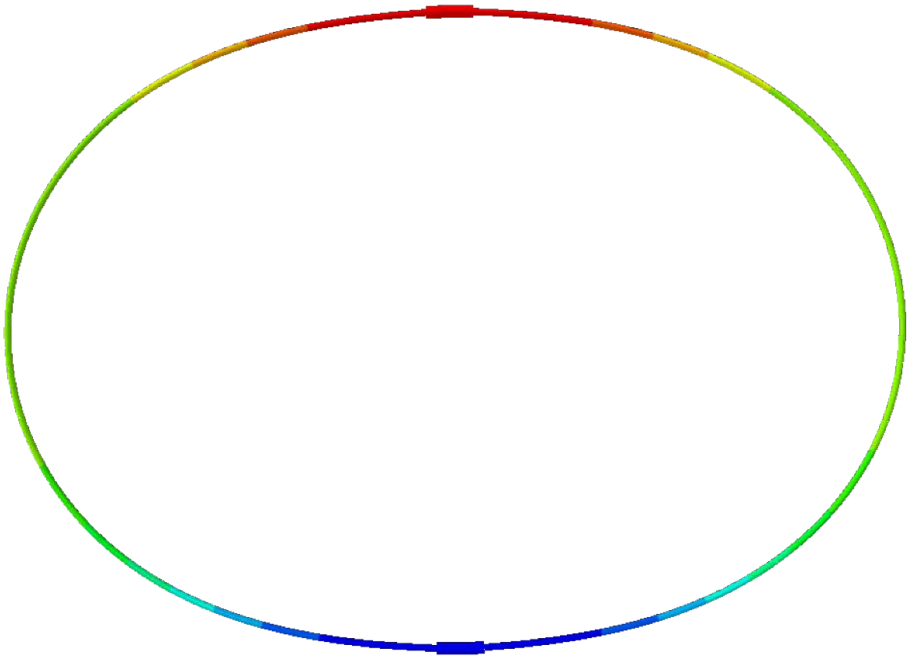

(b) Deformed basic ring model in FEA

Figure 102. The ring from the experiment (top) and from FEA (bottom) at a displacement of 38.1 mm.

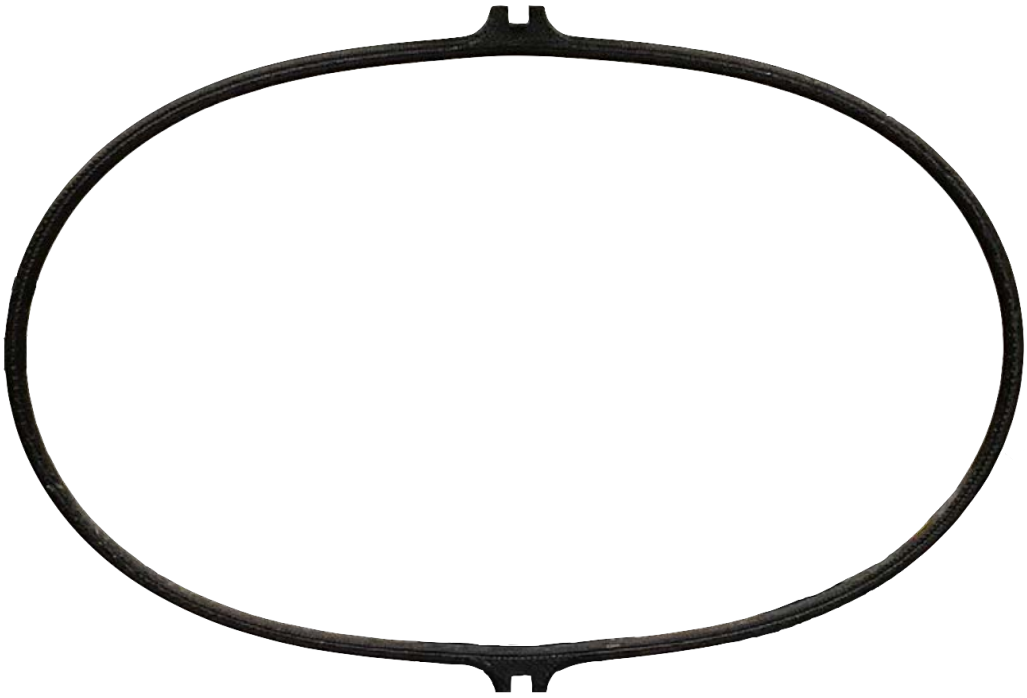

(a) Deformed ring in experiment

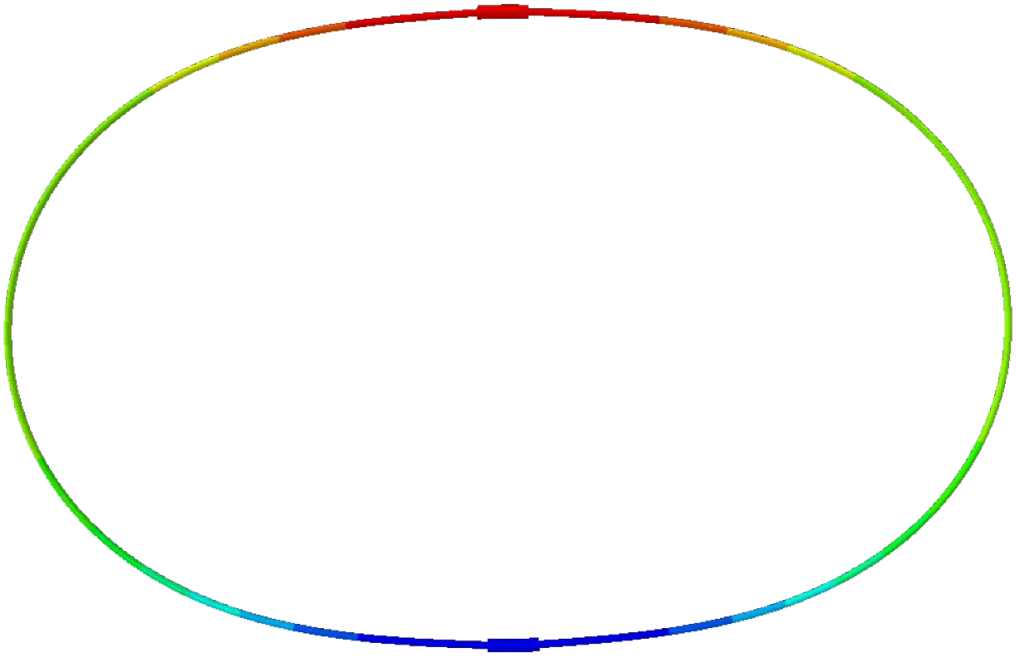

(b) Deformed basic ring model in FEA

Figure 103. The ring from the experiment (top) and from FEA (bottom) at a displacement of 50.8 mm.

The response of the tabbed ring model is measured against the experimental results from the Acumen to gain insight on it's ability to emulate the response. The results from both FEA and the experiments are plotted for each ring orientation. The results for the 0° ring are presented in Figure 104. The results for the 45° ring are presented in Figure 105. The results for the 90° ring are presented in Figure 106.

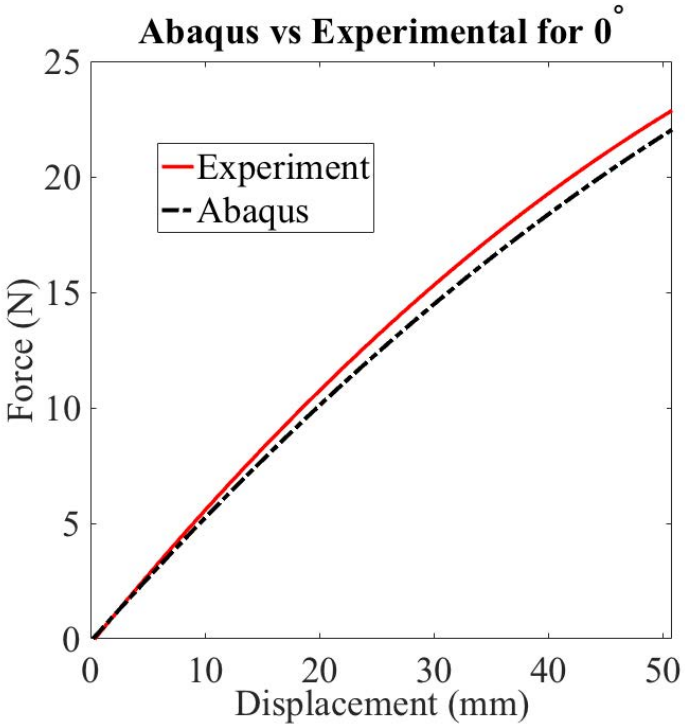

Figure 104. The comparison of results for the 0° tabbed ring model (FEA) and experimental results.

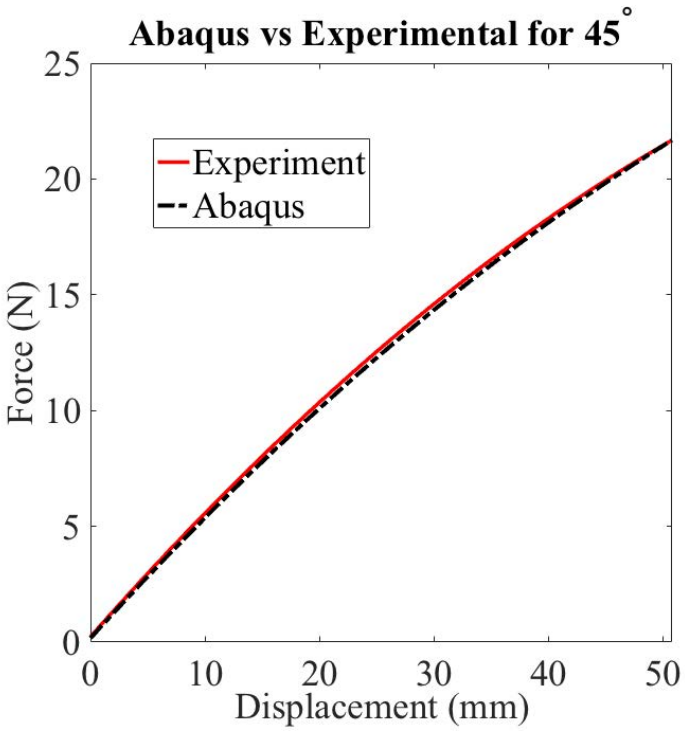

Figure 105. The comparison of results for the 45° tabbed ring model (FEA) and experimental results.

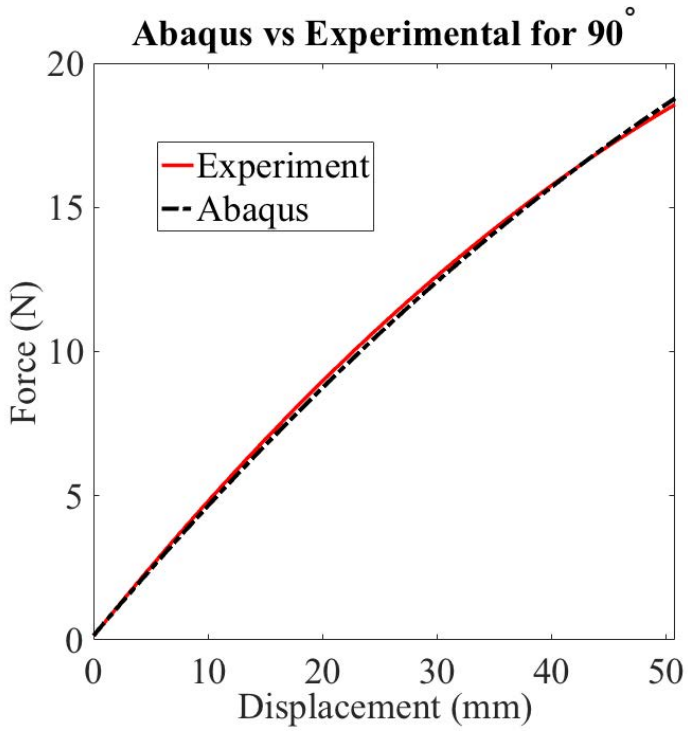

Figure 106. The comparison of results for the 90° tabbed ring model (FEA) and experimental results.

For all three cases, the tabbed ring model's response closely matches the corresponding response from experimentation. The only case that does not entirely align is the 0° model. The 0° model falls short of the experimental result. However, it is offset from the experimental response by a smaller magnitude than the offset in the comparison for the basic ring model. The tabbed ring model and experiment for the 45° and 90° responses align very well. The curves for both cases are nearly identical. Overall, it can be recognized that the tabbed ring model is a more accurate representation of the AM rings for each orientation. The basic ring model provides a reasonable approximation but lacks the fidelity of the tabbed ring model.

4.5 Increased Displacement Study

An additional analysis was conducted, both experimentally and analytically, to analyze the upper limits of a ring. A 168 mm displacement was prescribed to the top vertex of the 0° model. An analysis was performed with the tabbed ring model using this loading condition and the material properties for the 0° ring. The same loading condition was used for a 0° ring in the Acumen. The specifications for both the experiment and FEA remained the same as previous analyses except for the magnitude of displacement. Ultimately, the results for the two methods were compared to one another to gain insight on how the ring responds at an increased displacement.

The Acumen testing machine was by the stroke length of the upper head. Therefore, the ring could not be displaced a full 168 mm if the test began at the same starting position as the 50.8 mm-displacement tests. The cross-head of the MTS was brought down to adjust the initial displacement position so that the full 168 mm range could be achieved. The ring was displaced a total of 98 mm before the experiment was conducted. Figures 107-109 depict the starting position for the 0° ring within the Acumen.

Figure 107. Front view of the 0° ring loaded in the Acumen with a displaced initial position of 98 mm.

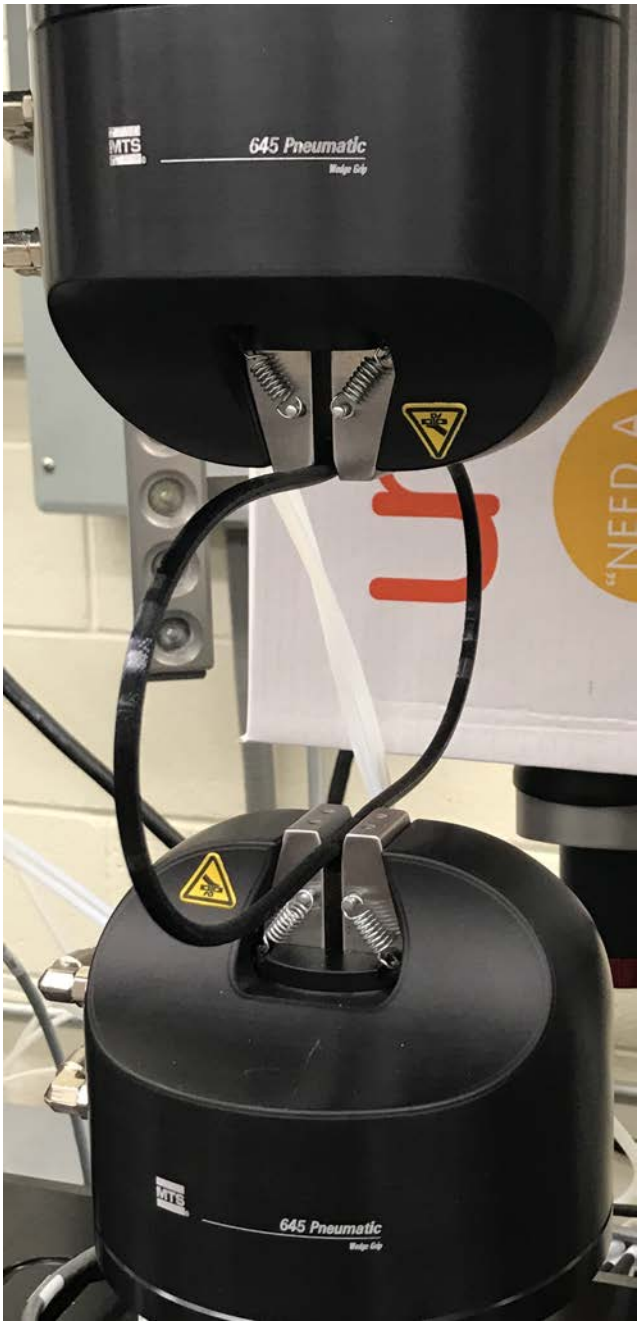

Figure 108. Backside view of the 0° ring loaded in the Acumen with a displaced initial position of 98 mm.

Figure 109. Side view of the 0° ring loaded in the Acumen with a displaced initial position of 98 mm.

A pictorial comparison between the experiment and FEA is provided in the following figures. The comparison points were taken at four different levels of displacement: 123 mm, 136 mm, 148 mm, and 161 mm. The background and foreground were removed from the experimental images to provide a clearer view of the ring's deformed profile. The images were taken at a slight angle to the ring due to the location of the MTS machine's guide posts. Therefore, the images of the experiment at different increments are slightly skewed.

(a) Ring in experiment

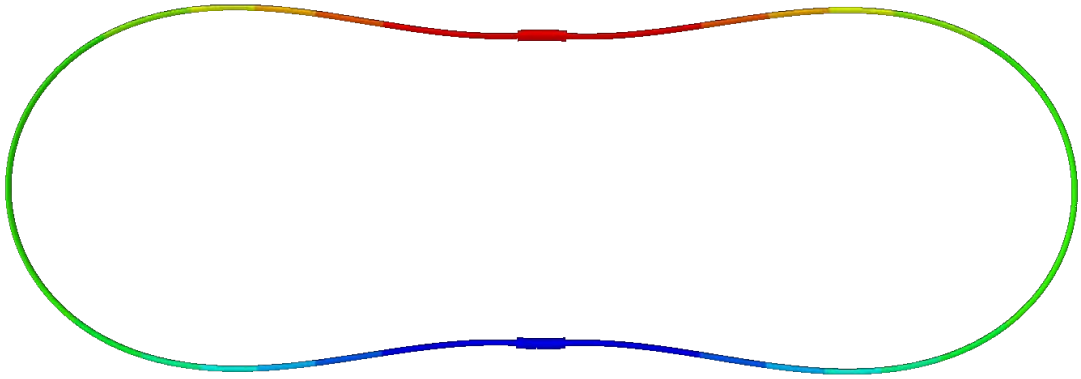

(b) Model in FEA

Figure 110. The ring from the experiment (top) and from FEA (bottom) at a displacement of 123 mm.

(a) Ring in experiment

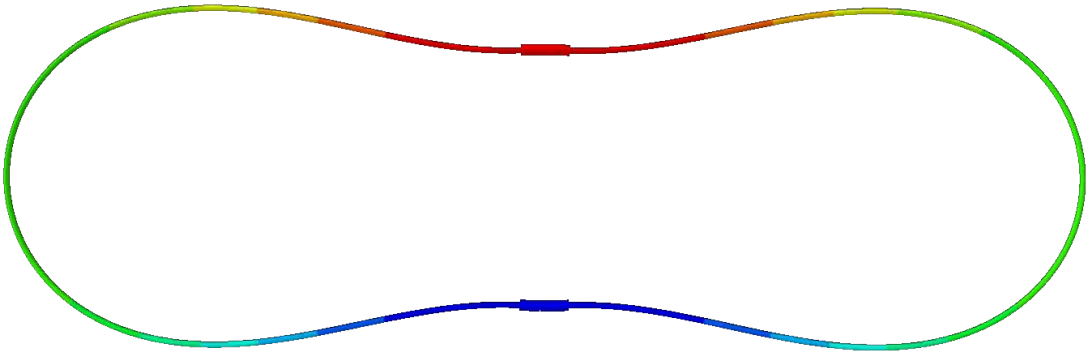

(b) Model in FEA

Figure 111. The ring from the experiment (top) and from FEA (bottom) at a displacement of 136 mm.

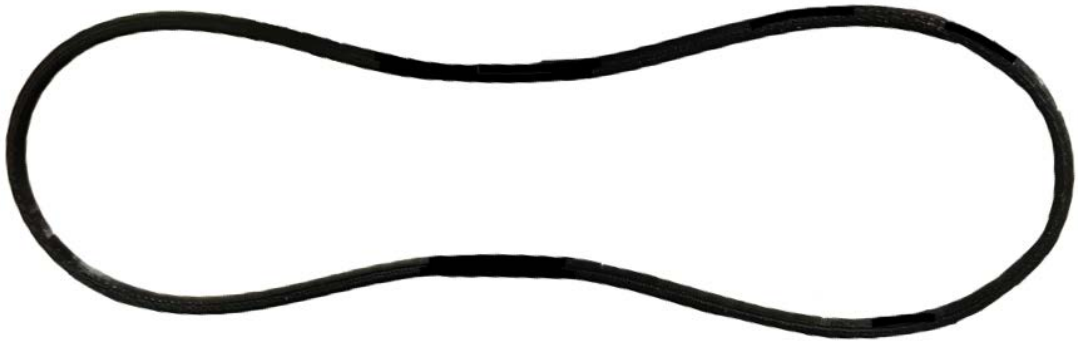

(a) Ring in experiment

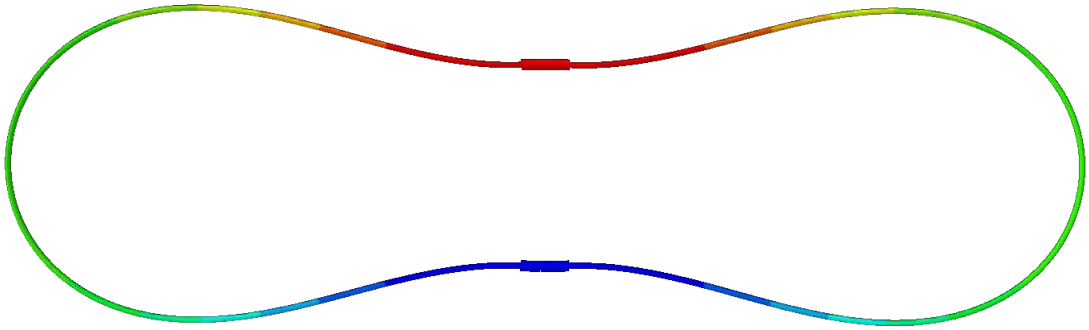

(b) Model in FEA

Figure 112. The ring from the experiment (top) and from FEA (bottom) at a displacement of 148 mm.

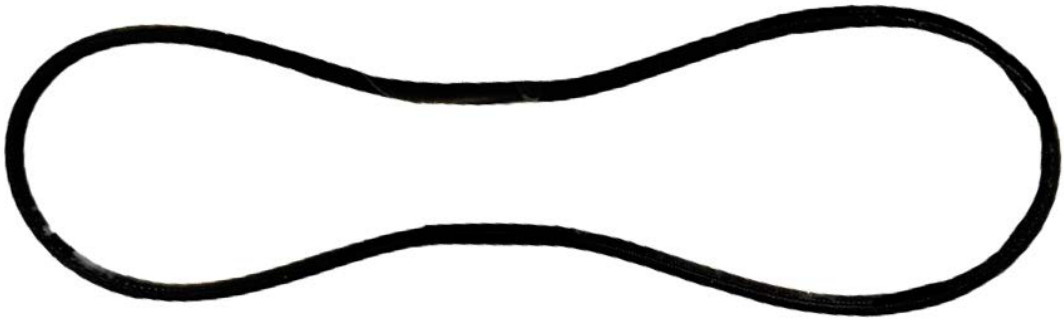

(a) Ring in experiment

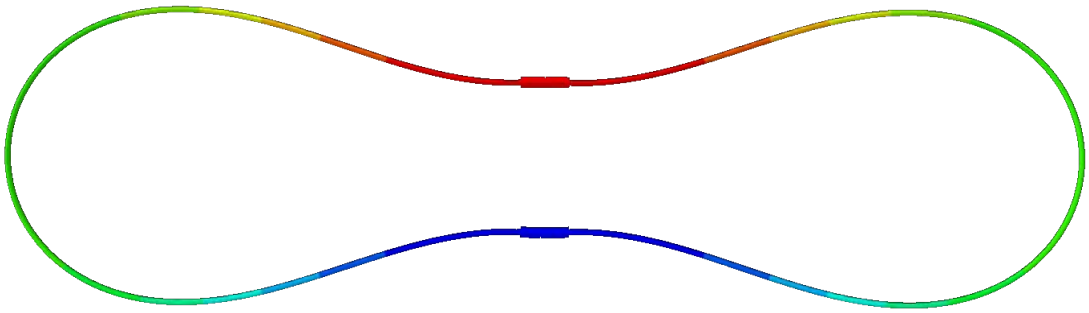

(b) Model in FEA

Figure 113. The ring from the experiment (top) and from FEA (bottom) at a displacement of 161 mm**.**

The plots of the response for this increased displacement are presented in Figures 114 and 115. As previously mentioned, the full response of the ring was not able to be captured experimentally due to the MTS testing machine limitations. Therefore, Figure 114 is the segment of data that was captured for the experiment. There were no limitations for the Abaqus analysis so the response for the entire range of displacement is presented in Figure 115.

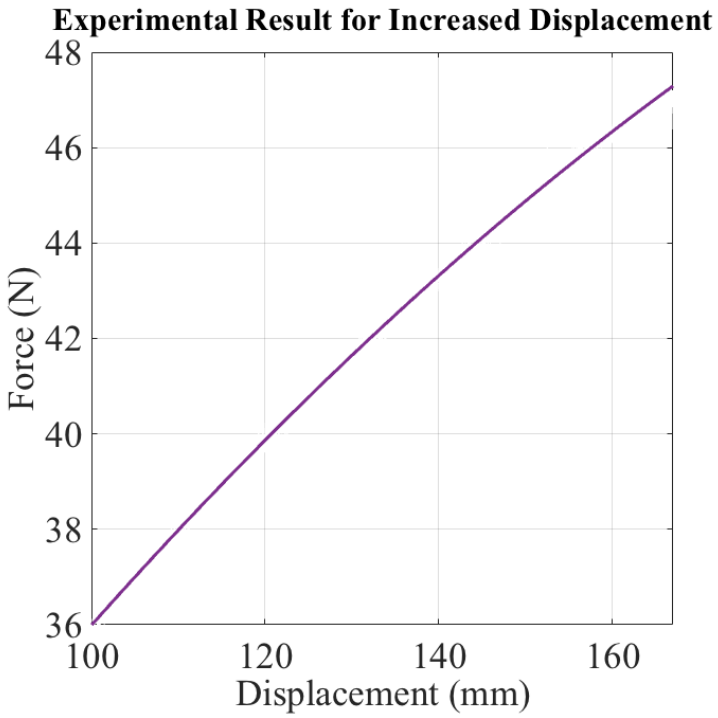

Figure 114. Response of 0° ring loaded from 98 mm to 168 mm in MTS.

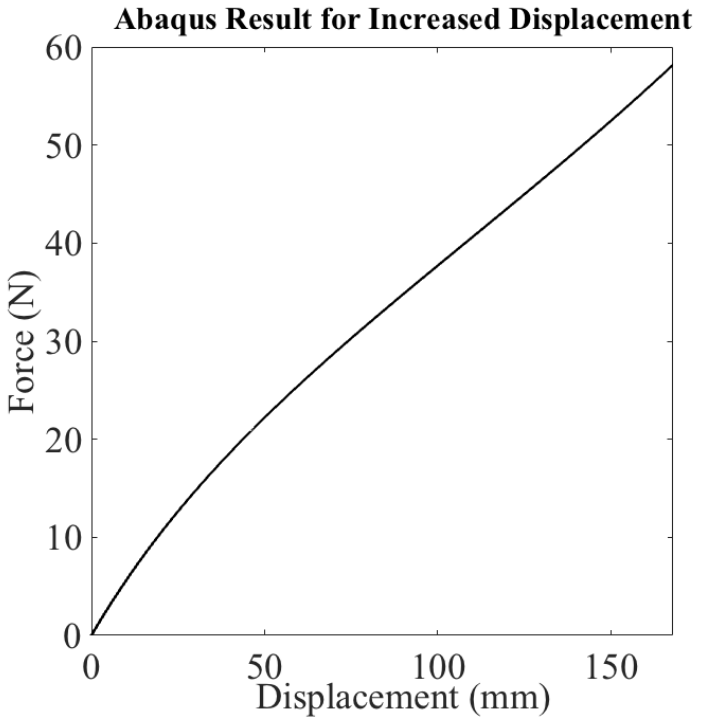

Figure 115. Response of the FEA model of a 0° ring loaded from 0 mm to 168 mm.

In Figure 115, the curve begins to slightly exhibit positive concavity. This suggests that the stiffness of the ring is increasing at this magnitude of displacement. According to Lacarbonara, this stiffening phenomenon may be attributed to "increasing tension-induced geometric stiffness driven by the increase of the curvature" [19]. The figures of the ring's profile at increased displacements reveal a substantial curvature in both sides of the ring. This curvature may be driving a slight increase in stiffness.

4.6 Arch Model

An analysis was conducted for an arch within Abaqus. The arch model represents the upper-half of a 90°-oriented ring that is a member of the celestial icosahedron frame. The specifications for the arch model are outlined in Chapter 3. The analysis was conducted to compare the response of the arch to the response of the 90° ring. The arch is representative of the upper segment of a 90° in the celestial frame because it is fixed at the ends. This is similar to the intersection points that stiffen the ring members within the celestial. The isolated 90° ring represents the worst case scenario because it doesn't have any additional support from the intersection of other ring members. The results for the arch model are presented below.

The displaced model of the arch is presented in Figure 116. The von Mises stress distribution for this displacement is shown in Figure 117. The plot of the response to the displacement condition is shown in Figure 118. The von Mises stress distribution for the 90° tabbed ring model is provided in Figure 119.

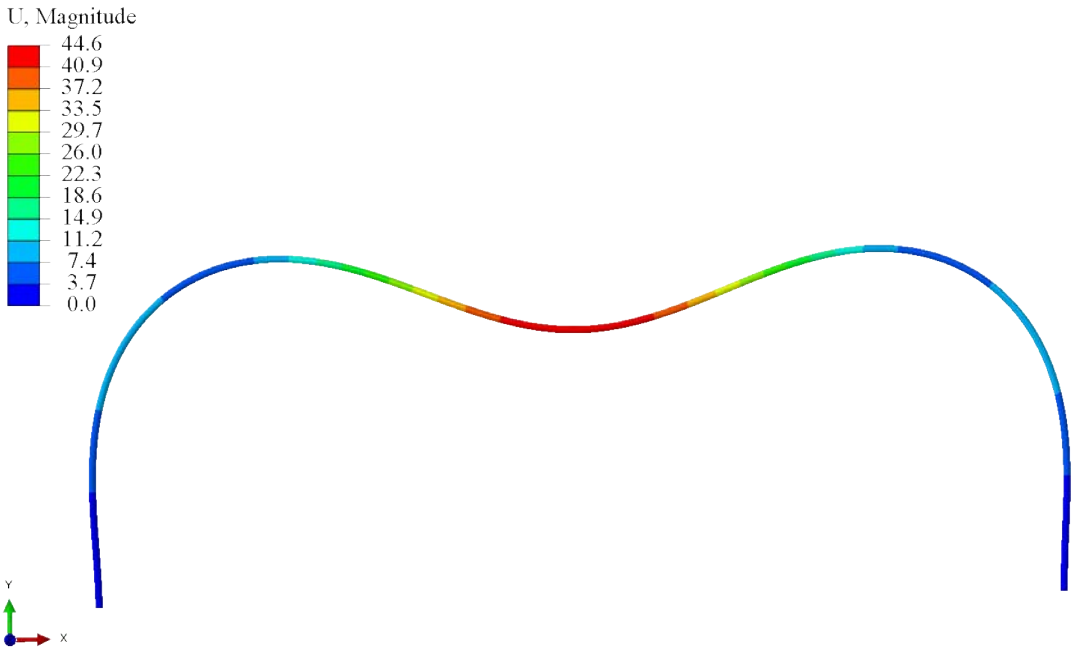

Figure 116. The displaced result of the FEA arch model due to a -50.8 mm displacement of the top vertex.

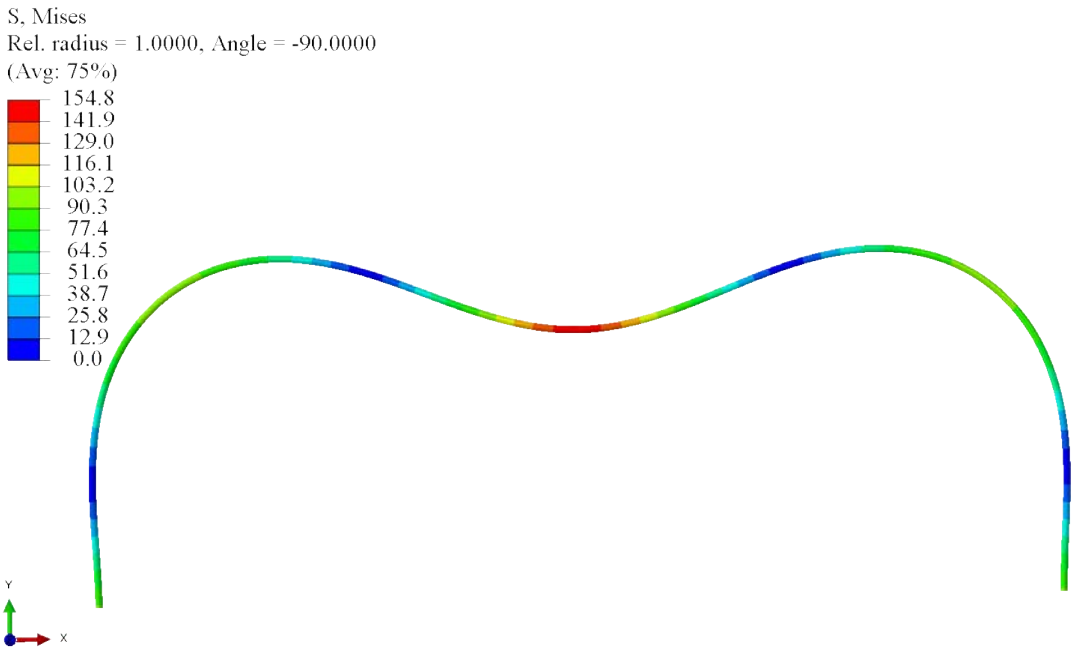

Figure 117. The von Mises stress distribution for the FEA arch model due at a -50.8 mm displacement of the top vertex.

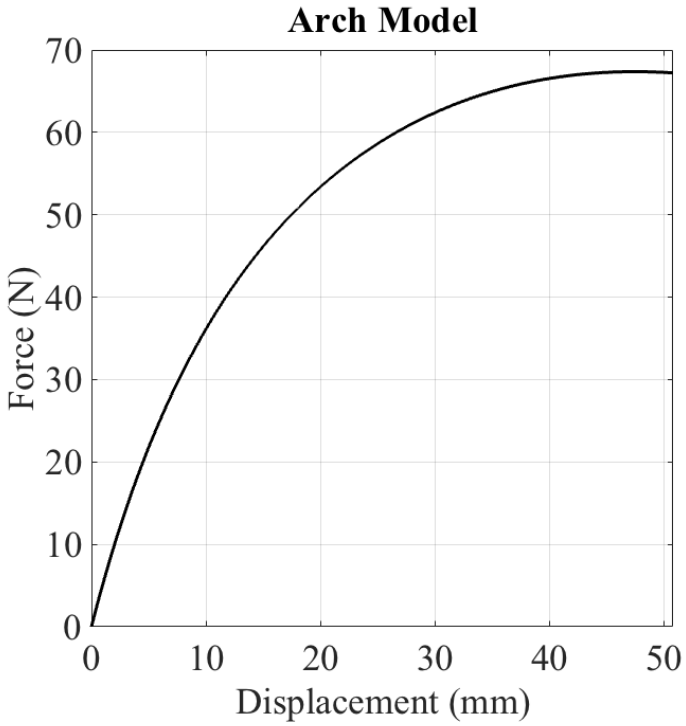

Figure 118. The response of the FEA arch model due to the prescribed loading condition.

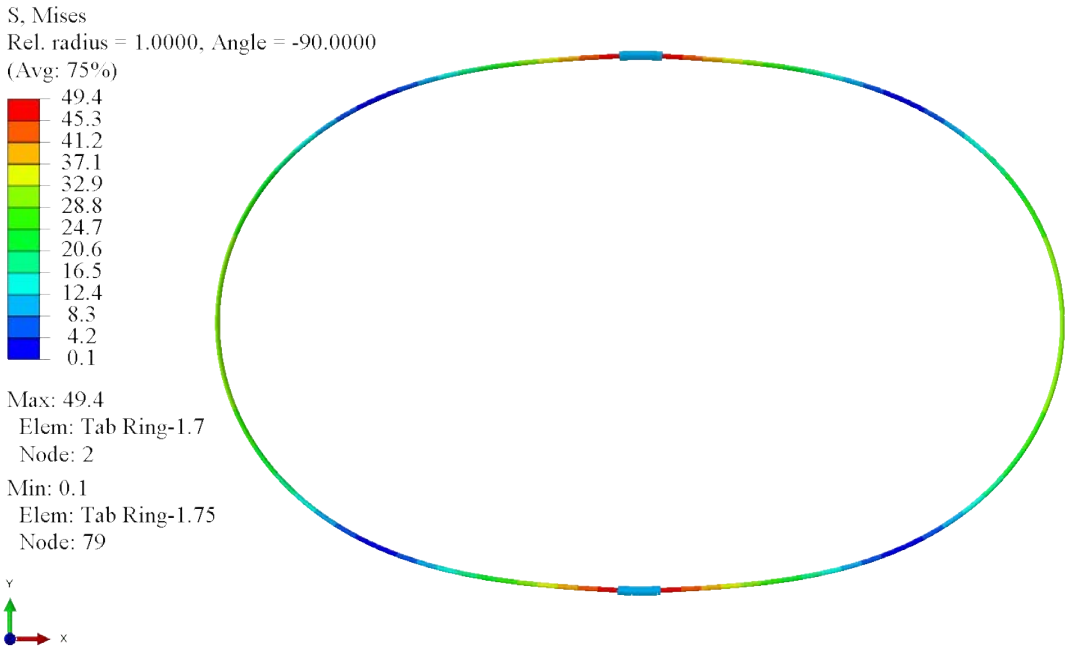

Figure 119. The von Mises stress distribution for the FEA tabbed ring model due to a -50.8 mm displacement of the top vertex.

From the figures, the maximum von Mises stress for the arch was 154.8 MPa. This occurs at the top region of the arch close to where the loading was applied. The maximum von Mises stress for the ring model was 49.4 MPa. This stress value occurs near both the top and bottom vertex of the ring model. The stress present in the arch for the same loading condition is three times the magnitude of the stress value in the ring. The fixed ends of the arch increase the stress throughout the model. The boundary conditions inhibit any movement of the ends of the arch, which in turn increases the stress within the model.

The ultimate tensile strength for the 90° build orientation for ULTEM 9085 is 42 MPa [29]. The ultimate compressive strength for the 90° build orientation is 87 MPa [29]. The flexural strength for the 90° build orientation is 68 MPa [29]. The maximum stresses present within the arch model exceed all three values provided in the manufacturer's sheet. Also, it can be observed in Figure 118 that the curve begins to to flatten significantly. The response transitions from linear to nonlinear before 10 mm of displacement occurs. The stiffness begins to decrease around at a displacement of 5 mm. However, the arch model is an approximate representation of a segment of the celestial icosahedron. The celestial's intersection points would not be fixed like the ends of the arch model. An analysis for the celestial icosahedron frame would be required to determine it's true response.

4.7 Chapter Summary

The results were presented, throughout this chapter, for each facet of the intended research. First, the products of the AM process were furnished. Next, the experimentation for the compression of each ring type were published alongside a discussion of the results. Finally, the FEA results and material property investigation was presented. The final chapter provides a conclusive discourse, with recommendations, for the research presented throughout this thesis.

V. Conclusion & Recommendations

The celestial icosahedron is a unique structure that offers the potential to serve as the frame for a VLTAV. The geometric size of the celestial and it's ring members was under investigation. An ideal, functional size would allow for it to be produced using in-house AM facilities. Also, it would be able to fit within an MTS testing rig. The behavior of the celestial under intense pressure loading was the driver to develop adequate sizing. The in depth analysis of a beam-column subject to sea-level pressure loading enabled for an appropriate beam thickness of $5.08mm$ to be determined. The first major objective of this research was the derivation of the appropriate geometric dimensions. These dimensions are critical for use in future research and analysis for the celestial icosahedron.

Individual rings were manufactured in a manner that was representative of the orientation in which they lie within the celestial: 0°, 45°, and 90°. The rings were loaded in compression experimentally and their response was measured. The response was different for each build type. The data followed the same trend but was different in magnitude. It can be concluded that the response to compression loading is affected by the orientation of the build. The 0° ring was the most stiff and the 90° ring was the least stiff. The 90° fractured on two occasions, thus solidifying the fact that is was the weakest build. It poses the biggest threat to the celestial icosahedron's structural integrity.

An intensive study on the ring's response, namely K and E, was conducted to verify the ring's material properties. FEA was employed in conjunction with experimentation to determine an effective value of E for each build orientation. These values were compared to the E values given by the manufacturer. It turns out that the rings closely compare to the flexural and tensile E values. They are vastly different from the published compressive E. As a result, it is concluded that the material

properties are influenced on the shape of the part that is being considered.

Lastly, a main tenet of this research was to investigate the nonlinear behavior of the rings. The response was nonlinear for each experimental case and this was confirmed by the FEA model. However, the ring's did not exhibit collapse behavior. A larger displacement was imposed on the FEA model to investigate this behavior further. It revealed that the ring model actually became stiffer as it displaced to greater magnitudes. It is presumed that the increase in curvature of the ring at this large displacement influenced the stiffening behavior. A recommendation for future work would be to confirm this finding experimentally.

Appendix A.

The following code produces the differential equations that govern the four different regions of the beam-column subject to an offset triangular load.

```
%% LHS Triangle: 0 < x1 < 0.65L

syms w0 L E I K C1 C2 x1
A = (10/39)*(w0/(E*I*L*K^2)); % A
B = 0; % B
C = ((-221/1200)*((L*w0)/(E*I)) - 6*A)/(K^2); % C
D = 0; % D
u2 = C1*sin(K*x1) + C2*cos(K*x1) + A*(x1^3) + C*x1; % u2 equation

% Boundary Condition: x1 = 0; u2 = 0
% x1 = 0; u2 = subs(u2)
C2 = 0; u2L = subs(u2); % sub in C2 from B.C.
du2L = diff(u2L,x1) % derivative of u2L

% x1 = 0.65*L; u2L = subs(u2L)

%% LHS Triangle: 0.65L < x1 < L

clear;clc
syms w0 L E I K C3 C4 x1 P u2
F = 0.5*0.65*L*w0; % resultant force from triangular loading
Ra = (221/1200)*L*w0; % Rxn at A
M2 = P*u2 + Ra*x1 - F*(x1-0.65*L+(1/3)*0.65*L); % Bending moment

% UC method
A = (169*w0*L)/(1200*E*I*(K^2)); % A constant
```

```
B = (-(169*w0*L^2)/(1200*E*I) - A)/(K^2); % B constant
u2 = C3*sin(K*x1) + C4*cos(K*x1) + A*x1 + B; % u2 equation

% Boundary Condition: x1 = L; u2 = 0
% x1 = L; u2 = subs(u2);
C4 = (1/cos(K*L))*((169*L*w0)/(1200*E*I*K^4) - C3*sin(K*L));
u2R = subs(u2);
du2R = diff(u2R,x1)

% x1 = 0.65*L;

%% LHS Loading - B.C.: x1 = 0.65*L, u2L = u2R

clear;clc
syms w0 L E I K C3 C4 x1 P u2 C1 C2

% B.C.: x1 = 0.65*L, u2L = u2R
eq1 = (C1*sin((13*K*L)/20) - (13*L*((221*L*w0)/(1200*E*I) + ...
    (20*w0)/(13*E*I*K^2*L)))/(20*K^2) + ...
        (169*L^2*w0)/(2400*E*I*K^2)) ...
     - (C3*sin((13*K*L)/20) - ((169*L^2*w0)/(1200*E*I) + ...
     (169*L*w0)/(1200*E*I*K^2))/K^2 - ...
         (cos((13*K*L)/20)*(C3*sin(K*L) ...
     - (169*L*w0)/(1200*E*I*K^4)))/cos(K*L) + ...
         (2197*L^2*w0)/(24000*E*I*K^2));
    % u2L - u2R

% B.C.: x1 = 0.65*L, du2L = du2R
eq2 = (C1*K*cos(K*x1) - ((221*L*w0)/(1200*E*I) + ...
    (20*w0)/(13*E*I*K^2*L))/K^2 ...
    + (10*w0*x1^2)/(13*E*I*K^2*L)) - (C3*K*cos(K*x1) + ...
        (K*sin(K*x1)*(C3*sin(K*L) ...
```

```
54      - (169*L*w0)/(1200*E*I*K^4)))/cos(K*L) + ...
            (169*L*w0)/(1200*E*I*K^2));
55      % du2L - du2R
56
57  x1 = 0.65*L; eq2 = subs(eq2); % substituting x1 = 0.65L
58  eq1 == 0; eq2 == 0; % setting both equations = 0
59
60  % Solving for C1 and C3
61  sol = solve([eq1, eq2], [C1, C3]);
62  C1 = sol.C1; % C1
63  C3 = sol.C3; % C2
64
65  % Solving for C4
66  C4 = (1/cos(K*L))*((169*L*w0)/(1200*E*I*K^4) - C3*sin(K*L));
67
68  % Plugging C1, C3, & C4 back into u2 eqns
69  syms x1
70
71  % displacement from 0 < x1 < 0.65L
72  u2L = C1*sin(K*x1) - (x1*((221*L*w0)/(1200*E*I) + ...
        (20*w0)/(13*E*I*K^2*L)))/K^2 ...
73       + (10*w0*x1^3)/(39*E*I*K^2*L);
74
75  % displacement from 0.65L < x1 < L
76  u2R = C3*sin(K*x1) - ((169*L^2*w0)/(1200*E*I) + ...
        (169*L*w0)/(1200*E*I*K^2))/K^2 ...
77       - (cos(K*x1)*(C3*sin(K*L) - ...
            (169*L*w0)/(1200*E*I*K^4)))/cos(K*L) + ...
78       (169*L*w0*x1)/(1200*E*I*K^2);
79
80  %% RHS Triangle: 0 < x1 < 0.65L
81
```

```
clear;clc;close all

syms L w0 C1 x1 K E I
Q2 = 0.5*0.35*L*w0;
Rb = (Q2*(0.65*L + (1/3)*0.35*L))/L;
Ra = Q2 - Rb;

u2L = C1*sin(K*x1) - ((49*L*w0)/(1200*E*I*K^2))*x1;

%% RHS Triangle: 0.65L < x1 < L

clear;clc
syms L w0 C1 x1 K E I P u2
Lp = x1 - 0.65*L;
y = ((0.35*L - Lp)*w0)/(0.35*L);
F1 = 0.5*(Lp)*(w0 - y);
F2 = Lp*y;
Ra = (49*L*w0)/1200;
M2 = -F1*(2/3)*Lp - F2*(Lp/2) + Ra*x1 + P*u2;
M2 = -M2/(E*I);

% UC
A = -(4000*w0)/(8400*E*I*L*K^2); % A
B = (12000*w0)/(8400*E*I*K^2); % B
C = ((-10873*w0*L)/(8400*E*I) - 6*A)/(K^2); % C
D = ((2873*w0*L^2)/(8400*E*I) - 2*B)/(K^2); % D

% Defining u2R
syms C3 C4
u2R = C3*sin(K*x1) + C4*cos(K*x1) + A*x1^3 + B*x1^2 + C*x1 + D; % u2R

% Apply B.C.: x1 = L, u2 = 0
```

```
% x1 = L;
% u2R = subs(u2R)

C4 = -C3*tan(K*L);
u2R = subs(u2R)

%% RHS Loading - Boundary Condition relating u2's and d(u2)'s

clear;clc
syms C3 C4 L w0 C1 x1 K E I P

% Relating displacements
u2L = C1*sin(K*x1) - ((49*L*w0)/(1200*E*I*K^2))*x1; % u2 for left ...
    side
u2R = C3*sin(K*x1) - ((20*w0)/(7*E*I*K^2) - ...
    (2873*L^2*w0)/(8400*E*I))/K^2 - ...
     C3*tan(K*L)*cos(K*x1) - (x1*((10873*L*w0)/(8400*E*I) - ...
     (20*w0)/(7*E*I*K^2*L)))/K^2 + (10*w0*x1^2)/(7*E*I*K^2) - ...
     (10*w0*x1^3)/(21*E*I*K^2*L); % u2 for right side

eqn1 = (C1*sin(K*x1) - ((49*L*w0)/(1200*E*I*K^2))*x1) - ...
    (C3*sin(K*x1)...
     - ((20*w0)/(7*E*I*K^2) - (2873*L^2*w0)/(8400*E*I))/K^2 - ...
     C3*tan(K*L)*cos(K*x1) - (x1*((10873*L*w0)/(8400*E*I) - ...
     (20*w0)/(7*E*I*K^2*L)))/K^2 + (10*w0*x1^2)/(7*E*I*K^2) - ...
     (10*w0*x1^3)/(21*E*I*K^2*L)); % u2L - u2R

% Relating slopes
du2L = diff(u2L,x1); % derivative of u2L w.r.t. x1
du2R = diff(u2R,x1); % derivative of u2R w.r.t. x1

eqn2 = (du2L) - (du2R); % du2L - du2R
```

```
143
144 x1 = 0.65*L;
145 eqn1 = subs(eqn1); eqn2 = subs(eqn2);
146 eqn1 == 0; % setting eqn1 = 0
147 eqn2 == 0; % setting eqn2 = 0
148
149 % Solving the system of equations for C1, C3, C4
150 sol = solve([eqn1, eqn2], [C1, C3]);
151 C1 = sol.C1; % C1
152 C3 = sol.C3; % C3
153 C4 = -C3*tan(K*L); % C4
154
155 % Plugging constants back into original equations
156 syms x1
157
158 % displacement from 0 < x1 < 0.65L
159 u2L = C1*sin(K*x1) - ((49*L*w0)/(1200*E*I*K^2))*x1; % u2 for left ...
       side
160
161 % displacement from 0.65L < x1 < L
162 u2R = C3*sin(K*x1) - ((20*w0)/(7*E*I*K^2) - ...
       (2873*L^2*w0)/(8400*E*I))/K^2 - ...
163      C3*tan(K*L)*cos(K*x1) - (x1*((10873*L*w0)/(8400*E*I) - ...
164      (20*w0)/(7*E*I*K^2*L)))/K^2 + (10*w0*x1^2)/(7*E*I*K^2) - ...
165      (10*w0*x1^3)/(21*E*I*K^2*L); % u2 for right side
166
167 %% Plugging in values to find the displacements in region I and II
168
169 clear;clc;close all
170
171 syms x1
172 c = 0.00342; % [m] -- 0.135 in
```

```
I = (pi*(c^4))/4;
E = 4.371e9; % [Pa] % elastic modulus
w0 = 4379.27; % [N/m]
L = 0.0777; % [m]
P = 342; % [N]
K = sqrt(P/(E*I));

% Region I (Left side)
u2L = -((10*w0*x1^3)/(39*E*I*K^2*L) - ...
(x1*((221*L*w0)/(1200*E*I) ...
    + (20*w0)/(13*E*I*K^2*L)))/K^2 + ...
    (sin(K*x1)*(24000*w0*cos((13*K*L)/20)*sin(K*L) ...
    - 24000*w0*cos(K*L)*sin((13*K*L)/20) +...
    2197*K*L^2*w0*cos((13*K*L)/20)^2 ...
    + 2197*K*L^2*w0*sin((13*K*L)/20)^2 + ...
    15600*K*L*w0*cos(K*L)*cos((13*K*L)/20) ...
    + 15600*K*L*w0*sin(K*L)*sin((13*K*L)/20) - ...
    2197*K*L^2*w0*cos(K*L)*cos((13*K*L)/20) ...
    - 2197*K*L^2*w0*sin(K*L)*sin((13*K*L)/20)))/...
    (15600*E*I*K^5*L*(cos((13*K*L)/20)^2*sin(K*L) ...
    + sin(K*L)*sin((13*K*L)/20)^2))) ...
    + (-(49*L*w0*x1)/(1200*E*I*K^2) -...
    (sin(K*x1)*(20*w0*sin((13*K*L)/20) ...
    - 20*w0*cos((13*K*L)/20)*tan(K*L) + ...
    7*K*L*w0*cos((13*K*L)/20) + ...
    7*K*L*w0*sin((13*K*L)/20)*tan(K*L)))/...
    (7*E*I*K^5*L*(cos((13*K*L)/20)^2*tan(K*L) ...
    + sin((13*K*L)/20)^2*tan(K*L))));
    % u2L(left loading) + u2L(right loading)

x1 = 0:0.001:0.65*L;
u2L = subs(u2L);
```

```
plot(x1,u2L,'b','LineWidth',4)
ylabel('u_2 [m]','FontSize',16)
xlabel('x_1 [m]','FontSize',16)
title('Displacement for 0 < x_1 < 0.65L','FontSize',16)
y2 = 0*x1;
hold on; plot(x1,y2,'k')
ylim([-3e-3 2e-3])

% Region II (Right side)
syms x1
u2R = -((cos(K*x1)*((169*L*w0)/(1200*E*I*K^4) - ...
(sin(K*L)*(2197*K*L^2*w0*cos((13*K*L)/20)^2 ...
    - 24000*w0*cos(K*L)*sin((13*K*L)/20) + ...
        2197*K*L^2*w0*sin((13*K*L)/20)^2 ...
    + 15600*K*L*w0*cos(K*L)*cos((13*K*L)/20) - ...
    2197*K*L^2*w0*cos(K*L)*cos((13*K*L)/20)))/...
    (15600*E*I*K^5*L*(cos((13*K*L)/20)^2*sin(K*L) ...
    + sin(K*L)*sin((13*K*L)/20)^2))))/cos(K*L) - ...
        ((169*L^2*w0)/(1200*E*I) ...
    + (169*L*w0)/(1200*E*I*K^2))/K^2 + ...
        (169*L*w0*x1)/(1200*E*I*K^2) + ...
    (sin(K*x1)*(2197*K*L^2*w0*cos((13*K*L)/20)^2 - ...
    24000*w0*cos(K*L)*sin((13*K*L)/20) ...
    + 2197*K*L^2*w0*sin((13*K*L)/20)^2 + ...
        15600*K*L*w0*cos(K*L)*cos((13*K*L)/20) - ...
    2197*K*L^2*w0*cos(K*L)*cos((13*K*L)/20)))/...
    (15600*E*I*K^5*L*(cos((13*K*L)/20)^2*sin(K*L) ...
    + sin(K*L)*sin((13*K*L)/20)^2))) ...
    + ((10*w0*x1^2)/(7*E*I*K^2) - (x1*((10873*L*w0)/(8400*E*I)...
    - (20*w0)/(7*E*I*K^2*L)))/K^2 ...
    - ((20*w0)/(7*E*I*K^2) - (2873*L^2*w0)/(8400*E*I))/K^2 -...
    (10*w0*x1^3)/(21*E*I*K^2*L) ...
```

```
    - (w0*sin(K*x1)*(20*sin((13*K*L)/20) + ...
        7*K*L*cos((13*K*L)/20)))/...
    (7*E*I*K^5*L*(cos((13*K*L)/20)^2*tan(K*L) ...
    + sin((13*K*L)/20)^2*tan(K*L))) + (w0*tan(K*L)*cos(K*x1)*...
    (20*sin((13*K*L)/20) + ...
    7*K*L*cos((13*K*L)/20)))/(7*E*I*K^5*L*...
    (cos((13*K*L)/20)^2*tan(K*L)...
    + sin((13*K*L)/20)^2*tan(K*L))));
    % u2R(left loading) + u2R(right loading)

x1 = 0.65*L:0.001:L;
u2R = subs(u2R);
figure
plot(x1,u2R,'r','LineWidth',4)
ylabel('u_2 [m]','FontSize',16)
xlabel('x_1 [m]','FontSize',16)
title('Displacement for 0.65L < x_1 < L','FontSize',16)
y2 = 0*x1;
hold on; plot(x1,y2,'k');ylim([-3e-3 2e-3])
%% Maximum moment

clear;clc;close all

syms x1 E I K L w0

% u2 for left side (Region I)
u2L = ((10*w0*x1^3)/(39*E*I*K^2*L) - (x1*((221*L*w0)/(1200*E*I) ...
    + (20*w0)/(13*E*I*K^2*L)))/K^2 + ...
        (sin(K*x1)*(24000*w0*cos((13*K*L)/20)*sin(K*L) ...
    - 24000*w0*cos(K*L)*sin((13*K*L)/20) + ...
        2197*K*L^2*w0*cos((13*K*L)/20)^2 ...
    + 2197*K*L^2*w0*sin((13*K*L)/20)^2 + ...
```

```
          15600*K*L*w0*cos(K*L)*cos((13*K*L)/20) ...
262     + 15600*K*L*w0*sin(K*L)*sin((13*K*L)/20) -...
263     2197*K*L^2*w0*cos(K*L)*cos((13*K*L)/20) ...
264     - 2197*K*L^2*w0*sin(K*L)*sin((13*K*L)/20)))/...
265     (15600*E*I*K^5*L*(cos((13*K*L)/20)^2*sin(K*L) ...
266     + sin(K*L)*sin((13*K*L)/20)^2))) ...
267     + (-(49*L*w0*x1)/(1200*E*I*K^2) - ...
          (sin(K*x1)*(20*w0*sin((13*K*L)/20) ...
268     - 20*w0*cos((13*K*L)/20)*tan(K*L) + 7*K*L*w0*cos((13*K*L)/20) ...
          + ...
269     7*K*L*w0*sin((13*K*L)/20)*tan(K*L)))/...
270     (7*E*I*K^5*L*(cos((13*K*L)/20)^2*tan(K*L) ...
271     + sin((13*K*L)/20)^2*tan(K*L))));
272
273 du2L = diff(u2L,x1); % du2/dx1 : first derivative w.r.t. x1
274 ddu2L = diff(du2L); % moment equation : second derivative w.r.t. x1
275
276 c = 0.00342; % [m] radius
277 I = (pi*(c^4))/4;
278 E = 2.4e9; % [Pa], elastic modulus
279 w0 = 4379.27; % [N/m]
280 L = 0.0777; % [m]
281 P = 342; % [N]
282 K = sqrt(P/(E*I));
283 x1 = 0:0.001:0.65*L;
284
285 ddu2L = subs(ddu2L); % sub. values into moment equation
286 ddu2L = abs(ddu2L); % absolute values for moments
287 M_max = max(ddu2L); % finding the maximum moment
288 M_max = vpa(M_max,4) % [N-m], value of the largest moment from 0 ...
      < x1 < 0.65L
289
```

```
290 sig = 70e6; % [Pa]
291 c = ((4*M_max)/(pi*sig))^(1/3); % [m], radius of the beam
292 t = 2*c; % [m], thickness of the beam
293 t = t*39.37 % [in], thickness of the beam
294
295 % sigma_YS = 187 MPa; compressive YS from the manufacturer table
296
297 %% Triple derivative of u2L w.r.t. x1
298
299 clear;clc;close all
300
301 syms x1 E I K L w0
302
303 % u2 for left side (Region I)
304 u2L = ((10*w0*x1^3)/(39*E*I*K^2*L) - (x1*((221*L*w0)/(1200*E*I) ...
305     + (20*w0)/(13*E*I*K^2*L)))/K^2 + ...
306     (sin(K*x1)*(24000*w0*cos((13*K*L)/20)*sin(K*L) ...
307     - 24000*w0*cos(K*L)*sin((13*K*L)/20) + ...
            2197*K*L^2*w0*cos((13*K*L)/20)^2 ...
308     + 2197*K*L^2*w0*sin((13*K*L)/20)^2 + ...
            15600*K*L*w0*cos(K*L)*cos((13*K*L)/20) ...
309     + 15600*K*L*w0*sin(K*L)*sin((13*K*L)/20) - ...
            2197*K*L^2*w0*cos(K*L)*cos((13*K*L)/20) ...
310     - 2197*K*L^2*w0*sin(K*L)*sin((13*K*L)/20)))/...
311     (15600*E*I*K^5*L*(cos((13*K*L)/20)^2*sin(K*L) ...
312     + sin(K*L)*sin((13*K*L)/20)^2))) ...
313     + (-(49*L*w0*x1)/(1200*E*I*K^2) - ...
            (sin(K*x1)*(20*w0*sin((13*K*L)/20) ...
314     - 20*w0*cos((13*K*L)/20)*tan(K*L) + 7*K*L*w0*cos((13*K*L)/20) ...
            + ...
315     7*K*L*w0*sin((13*K*L)/20)*tan(K*L)))/...
316     (7*E*I*K^5*L*(cos((13*K*L)/20)^2*tan(K*L) ...
```

```
317      + sin((13*K*L)/20)^2*tan(K*L))));
318
319 du2L = diff(u2L,x1); % du2/dx1 : first derivative w.r.t. x1
320 ddu2L = diff(du2L,x1); % moment equation : second derivative ...
       w.r.t. x1
321 dddu2L = diff(ddu2L,x1); % triple derivative w.r.t. x1
322
323 c = 0.00342; % [m] radius
324 I = (pi*(c^4))/4;
325 E = 2.4e9; % [Pa], elastic modulus
326 w0 = 4379.27; % [N/m]
327 L = 0.0777; % [m]
328 P = 342; % [N]
329 K = sqrt(P/(E*I));
330
331 dddu2L = subs(dddu2L); dddu2L == 0; % setting the triple ...
       derivative to 0
332 solve(dddu2L,x1) % solving for x1 at triple derivative == 0
333 % x1 = 0.03961 m --- matches up w/ the plot. Location of the maximum
334 % bending moment.
335
336 %% Maximum Bending Moment
337
338 clear;clc;close all
339
340 % Occurs at x1 = 0.03961 m as found from above. Inserting ...
       coordinate into
341 % the moment equation(s) found from combining M_L from both beam ...
       analyses.
342 syms x1 E I K L w0
343
344 M_L = ((221/1200)*L*w0*x1 - ((10*w0)/(39*L))*x1^3) + ...
```

```
      (49*L*w0*x1)/(1200);

w0 = 4379.27; % [N/m]
L = 0.0777; % [m]
x1 = 0.03961; % [m], location of max bending moment

M_L = subs(M_L); % [N-m], maximum moment due to bending
M_L = vpa(M_L,4)

%% Solve for c (radius) and thickness (t)

clear; clc

syms M c I s P
sig = (M*c)/I + P/(pi*c^2) == 187e6;
I = (pi*c^4)/4;
M = 2.134; % [N-m]
P = 342; % [N] == 77 [lb_f]
sig = subs(sig);
c = solve(sig,c); % [m], solving for radius

% Thickness
t = 2*c(1); % [m], solving for the thickness
t = t*39.37; % [in], thickness of the beam
t = vpa(t,4) % [in]

fprintf('\nThe thickness for the beam is: %0.3f inches\n\n',t)
```

Appendix B.

The distribution of stress is another salient characteristic that was investigated using Abaqus. The following analyses were conducted in English units (*psi*, *in*, etc.). The following images display the distribution of the von Mises stress distribution for each model due to a 50.8 *mm* displacement:

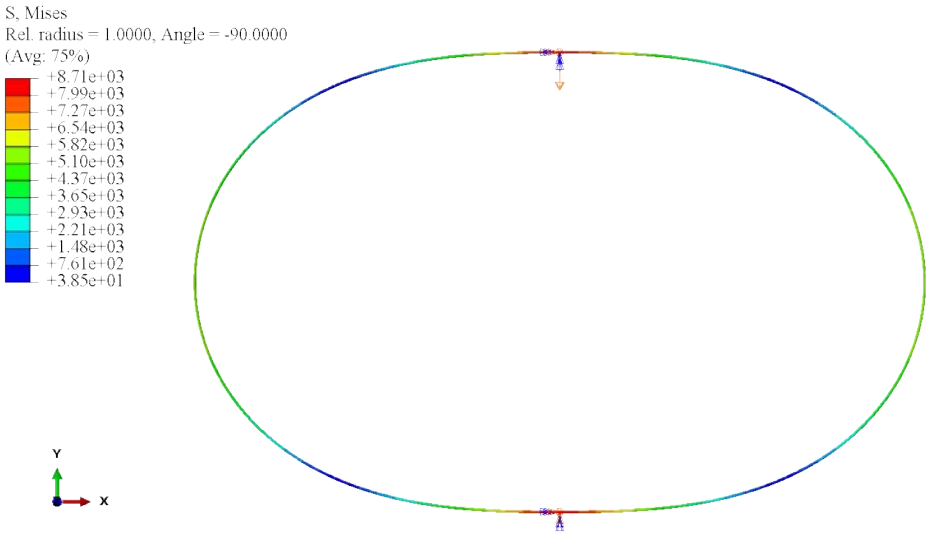

Figure 120. The von Mises for 0° model.

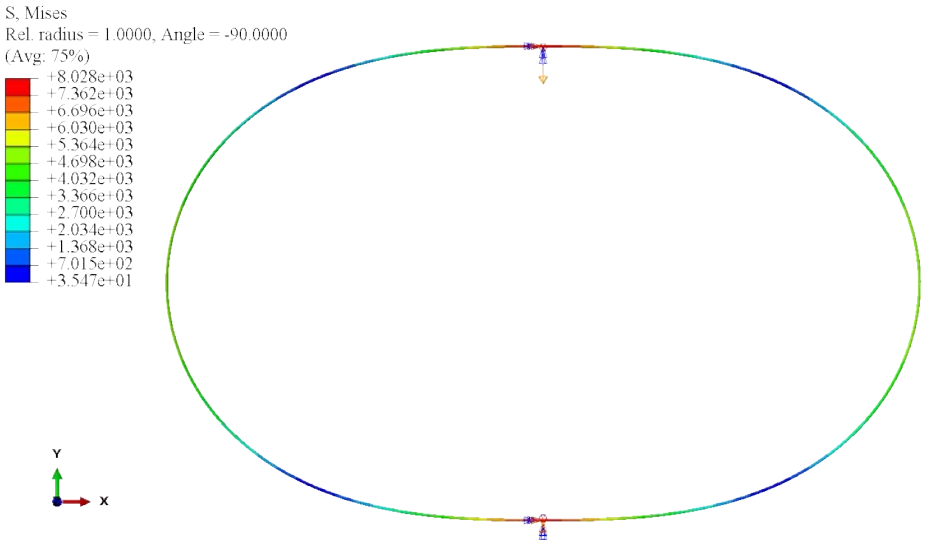

Figure 121. The von Mises for 45° model.

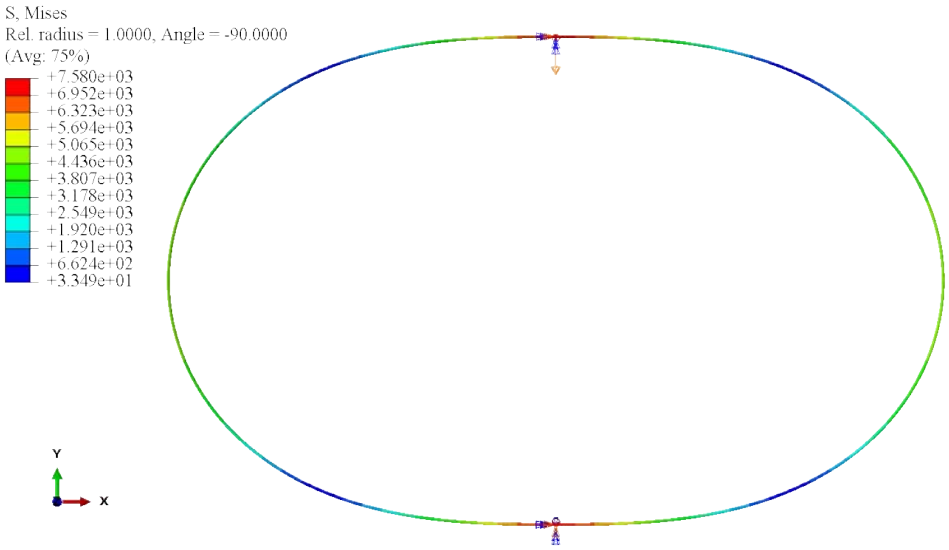

Figure 122. The von Mises for 90° model.

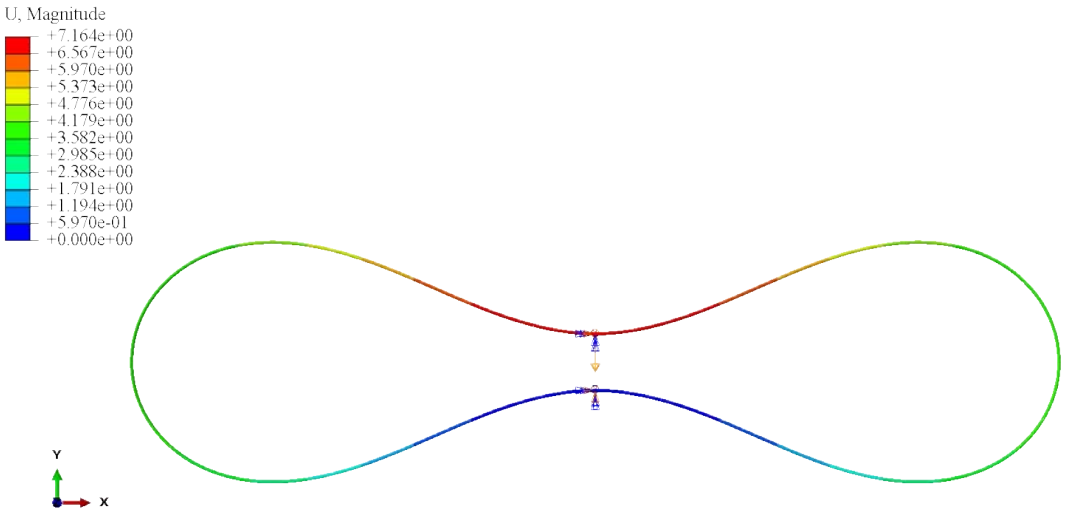

Figure 123. 200 mm displacement loading condition for 0° basic ring model.

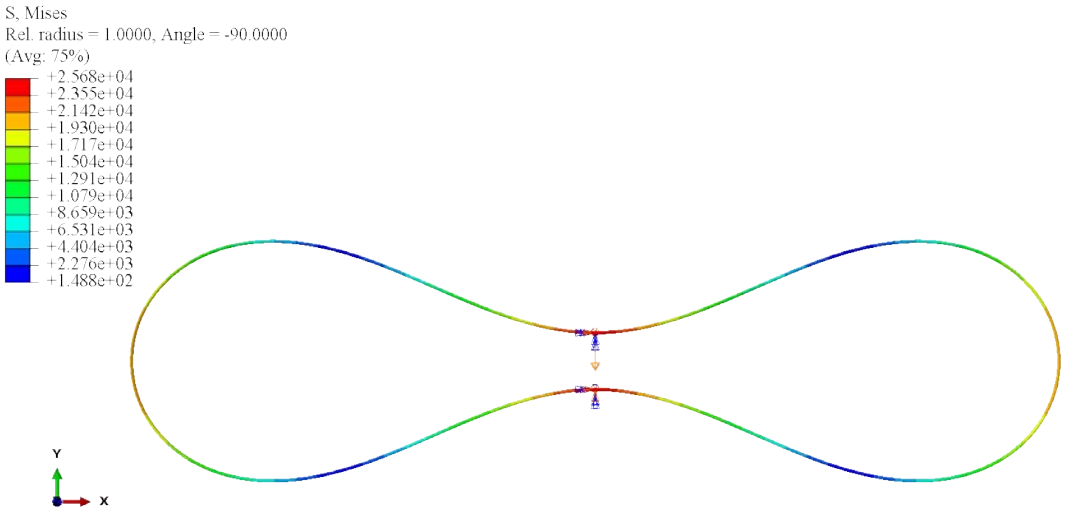

Figure 124. von Mises for 200 mm displacement loading condition for 0° basic ring model.

The following figures present the displacement at different increments for the FEA basic ring model.

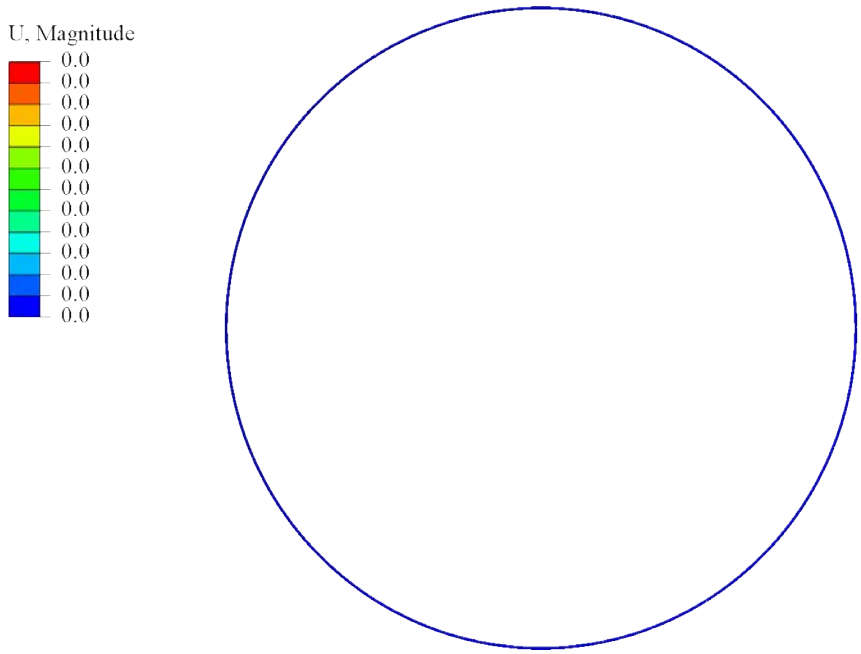

Figure 125. 0 mm displacement for basic ring model with 0° material properties.

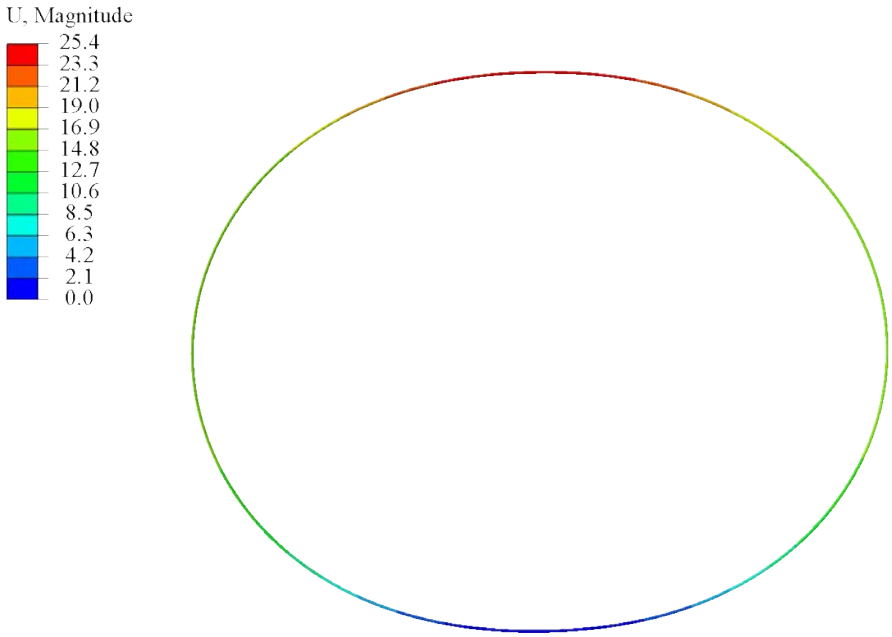

Figure 126. 25.4 mm **displacement for basic ring model with 0° material properties.**

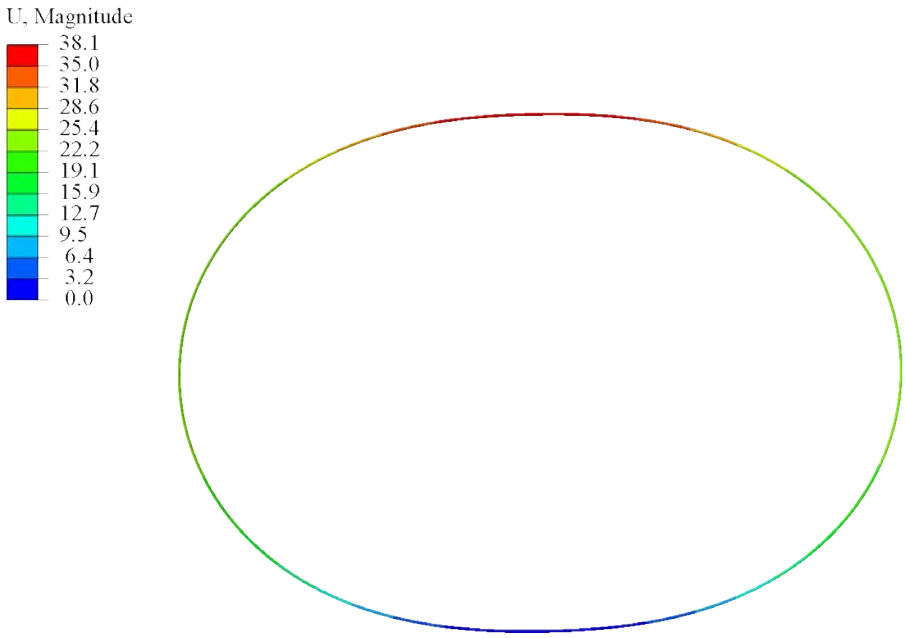

Figure 127. 38.1 mm **displacement for basic ring model with 0° material properties.**

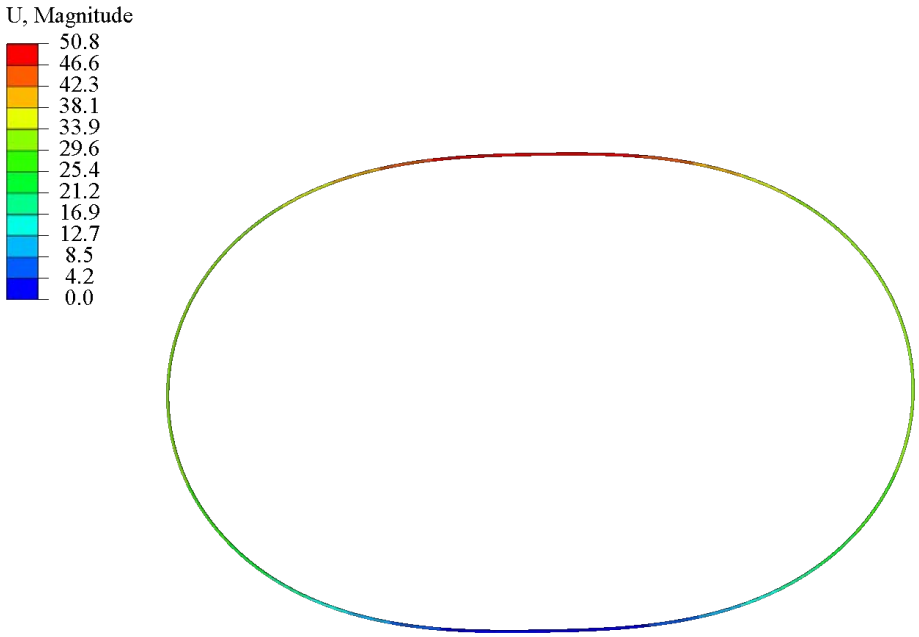

Figure 128. 50.8 mm displacement for basic ring model with 0° material properties.

Bibliography

1. D. Lukco, D.J. Spry, G.C.C. Costa, R.S. Okojie, A. Avishai, L.M. Nakley, P.G. Neudeck, and G.W. Hunter. Chemical Analysis of Materials Exposed to Venus Temperature and Surface Atmosphere. *Earth and Space Science*, 2017.

2. GreekMythology.com. Icarus, 2020. https://www.greekmythology.com/Myths/Mortals/Icarus/icarus.

3. R.J. Shaw. History of flight, 2014. https://www.grc.nasa.gov/www/k-12/UEET/StudentSite/historyofflight.

4. FamousInventors.org. Montgolfier brothers, 2018. https://www.famousinventors.org/montgolfier-brothers.

5. T.D. Crouch. Lighter-than-air, 2013. https://www.centennialofflight.net/essay/Lighter-than-air/LTA-OV.

6. battlefields.org. Civil war ballooning, 2019. https://www.battlefields.org/learn/articles/civil-war-ballooning.

7. The Airship Association. Types of airship, 2019. http://www.airship-association.org/cms/node/28.

8. C. Dusch. Zeppelin (airship), 2019. https://encyclopedia.1914-1918-online.net/pdf/1914-1918-Online-zeppelin-airship-2019-01-25.pdf.

9. Weebau. Francesco lana de terzi, 2012. http://weebau.com/history/lanadeterzi.

10. B.R. Munson, T.H. Okiishi, and D.F. Young. *Fundamentals of Fluid Mechanics*. John Wiley & Sons, Inc., 2006.

11. A.M. Akhmeteli and A.V. Gavrilin. Layered shell vacuum balloons, May12 2005. US Patent Application US11/127,613.

12. T.T. Metlen. Design of a Lighter Than Air Vehicle That Achieves Positive Buoyancy in Air Using a Vacuum. *Theses and Dissertations*, (838), 2012.

13. E.W. Weisstein. Icosahedron, 2001. http://mathworld.wolfram.com/Icosahedron.

14. K.D. Moore. Quasi-Static Nonlinear Analysis of a Celestial Icosahedron Shaped Vacuum Lighter Than Air Vehicle. *Theses and Dissertations*, (1779), 2018.

15. D.P. Graves. Initial Stage of Fluid-Structure Interaction of a Celestial Icosahedron Shaped Vacuum Lighter Than Air Vehicle. *Theses and Dissertations*, (2218), 2019.

16. B.C. Cranston. Conceptual Design, Structural Analysis, and Design Space Exploration of a Vacuum Lighter than Air Vehicle. *Theses and Dissertations*, (424), 2016.

17. B.C. Cranston, M. AlGhofaily, and A.N. Palazotto. Design and structural analysis of unique structures under an internal vacuum. *Aerospace Science and Technology*, 2017.

18. R.D. Cook, D.S. Malkus, M.E. Plesha, and R.J. Witt. *Concepts and Applications of Finite Element Analysis*. John Wiley & Sons, Inc., 2007.

19. W. Lacarbonara. *Nonlinear Structural Mechanics: Theory, Dynamical Phenomena and Modeling*. Springer Science+Business Media, 2013.

20. Dassault Systémes. Abaqus analysis user's guide (6.13), 2013. http://dsk.ippt.pan.pl/docs/abaqus/v6.13/index.

21. A. Khennane. *Introduction to Finite Element Analysis Using MATLAB and Abaqus*. CRC Press, 2013.

22. J.R. Brauer. *What Every Engineer Should Know About Finite Element Analysis*. Marcel-Dekker, 1993.

23. G. Dhondt. Calculix crunchix user's manual, 2014. http://web.mit.edu/calculix-v2.7/CalculiX/ccx-2.7/doc/ccx/node1.

24. A. Harish. Implicit vs explicit finite element method (fem): What is the difference?, 2019. https://www.simscale.com/blog/2019/01/implicit-vs-explicit-fem/.

25. N. Vasios. Nonlinear Analysis of Structures The Arc Length Method: Formulation, Implementation and Applications. *Harvard Universityl*, 2015.

26. T. Heister and L.G. Rebholz. *Scientific Computing For Scientists and Engineers*. De Gruyter, 2015.

27. A.S. Saada. *Elasticity: Theory and Applications*. J. Ross Publishing, 2009.

28. A.N. Palazotto. Mech 600: Elasticity, pt *ii*, 2019.

29. Stratasys. Ultem™ 9085 resin high-performance fdm pei thermoplastic, 2020. https://www.stratasys.com/materials/search/ultem9085.

30. Stratasys. Fortus 380mc and fortus 450mc, 2017. https://www.stratasys.com/3d-printers/fortus-380mc-450mc.

31. A.B. Varotsis. Introduction to fdm 3d printing, 2020. https://www.3dhubs.com/knowledge-base/introduction-fdm-3d-printing.

32. M. AlGhofaily. Finite Element Analysis and Experimentation of an Icosahedron Frame under Compression. *Theses and Dissertations*, (1924), 2015.

33. MTS Systems Corporation. 661.19 force transducer, 1996.

34. ASTM International. Standard Test Method for Compressive Properties of Rigid Plastics. *ASTM Committee D20 on Plastics*, (D695-15), 2015.

35. MathWorks Help Center. Savitzky-golay filtering, 2020. https://www.mathworks.com/help/signal/ref/sgolayfilt.

36. Stratasys. Materials testing procedure, 2019. https://www.stratasys.com/-/media/files/brochures/BR-FDM-MaterialsTestingProcedure-0919a.

REPORT DOCUMENTATION PAGE

Form Approved
OMB No. 0704–0188

1. REPORT DATE *(DD–MM–YYYY)*	2. REPORT TYPE	3. DATES COVERED *(From — To)*
26-03-2020	Master's Thesis	Sep 2018 — Mar 2020

4. TITLE AND SUBTITLE

Analysis of Additively Manufactured Rings Under Compression Loading for Use in a Vacuum Lighter Than Air Vehicle Structure

5a. CONTRACT NUMBER

5b. GRANT NUMBER

5c. PROGRAM ELEMENT NUMBER

6. AUTHOR(S)

Greenoe, Kevin, D, 2d Lt

5d. PROJECT NUMBER

5e. TASK NUMBER

5f. WORK UNIT NUMBER

7. PERFORMING ORGANIZATION NAME(S) AND ADDRESS(ES)

Air Force Institute of Technology
Graduate School of Engineering and Management (AFIT/EN)
2950 Hobson Way
WPAFB OH 45433-7765

8. PERFORMING ORGANIZATION REPORT NUMBER

AFIT-ENY-MS-20-M-264

9. SPONSORING / MONITORING AGENCY NAME(S) AND ADDRESS(ES)

Air Force Office of Scientific Research
875 N. Randolph St
Arlington, VA, 22203-1768
(703) 588-8316
jaimie.tiley@usaf.mil

10. SPONSOR/MONITOR'S ACRONYM(S)

AFOSR

11. SPONSOR/MONITOR'S REPORT NUMBER(S)

12. DISTRIBUTION / AVAILABILITY STATEMENT

Distribution Statement A.
Approved for Public Release; Distribution Unlimited.

13. SUPPLEMENTARY NOTES

14. ABSTRACT

A Vacuum Lighter Than Air Vehicle (VLTAV) utilizes a lightweight structure paired with an internal vacuum to achieve buoyancy; this allows it to float through-out a given atmosphere. The pressure differential between the internal vacuum and external atmosphere places the vehicle under intense loading. A specific structure under investigation is the celestial icosahedron, which features nine intersecting rings that have an outer diameter of 0.2032m and circular cross-sectional thickness of 5.08mm.The celestial's rings are positioned in three different orientations and are analyzed both experimentally and analytically.

15. SUBJECT TERMS

Vacuum Lighter Than Air Vehicle, Additive Manufacturing, Nonlinear Solid Mechanics, Compression Testing

16. SECURITY CLASSIFICATION OF:			17. LIMITATION OF ABSTRACT	18. NUMBER OF PAGES	19a. NAME OF RESPONSIBLE PERSON
a. REPORT	b. ABSTRACT	c. THIS PAGE			Dr. Anthony N. Palazotto, AFIT/ENY
U	U	U	UU	178	19b. TELEPHONE NUMBER *(include area code)* (937) 255-3636x4599 anthony.palazotto@afit.edu